THE UNIVERSITY OF MICHIGAN

COLLEGE OF ENGINEERING
Department of Nuclear Engineering

Technical Report

THE HYDROSTATIC PRESSURE EFFECT ON THE EPR SPECTRA OF Cr^{3+} AND V^{2+} IN SAPPHIRE

Alan F. Clark
Richard H. Sands
Chihiro Kikuchi

ORA Project 06029

under contract with:

U.S. ARMY MATERIEL COMMAND
HARRY DIAMOND LABORATORIES
CONTRACT NO. DA-49-186-AMC-80(x)
WASHINGTON, D.C.

administered through:

OFFICE OF RESEARCH ADMINISTRATION ANN ARBOR

May 1964

This report was also a dissertation submitted by the first author in partial fulfillment of the requirements for the degree of Doctor of Philosophy in The University of Michigan, 1964.

ERRATA

Page

3 line 3: lattice sites, though possibly including the displacements proposed in the literature, and are subject....

4 line 25: spectrum of ruby. (also p. 5, line 1).

11 line 9: coulomb interactions

12 line 10: This type of analysis

18 Figure 1: upper ^4F state is $^4T_1$

28 Figure 3: Exchange coordinates x and y (Not E or H).

29 line 16: in equation 8 (also equation 12 is 12').

45 line 20: three. The use of....

48 line 16: is valid if

54 line 8: to Stevens[57]

59 line 15: three hours at 7×10^6 rads/min.[38]

80 line 18: signal to noise ratio,

85 line 21: misalignment

107 last two equations: .... $k^2 r^2 d(kr)$

109 line 18: the cubic field

116 line 12: are E, C_3, and C_3^2.

124 line 8: where $P_{20} = \frac{1}{2}(3 \cos^2 \theta_i - 1)$.

145 figure: delete (D3)

155 equation F8: $h\nu_{T_1} = E\left[{}^4A_2(F) \rightarrow {}^4T_1(F,P)\right]$ =....

160 last equation: $\frac{1}{3}\left\{\sqrt{2}\ (Y_3^3 .....\right.$

TABLE OF CONTENTS

LIST OF TABLES

LIST OF FIGURES

Figures (cont'd) Page

Abstract

The interaction of the Cr^{3+} and V^{2+} impurity ions with the α-Al_2O_3 crystal lattice was studied by observing the hydrostatic pressure dependence of their electron paramagnetic resonance spectra to 6000 atmospheres.

A two sample comparison method was used in which two identical samples are placed in the X band microwave resonant cavity. One end of the cavity and one sample are subject to hydrostatic pressure. The changes in the spin Hamiltonian parameters are obtained by measuring the difference in the magnetic field required for the same resonant condition in each sample as a function of pressure.

The observed changes were:

Cr^{3+}:

$$\frac{\Delta 2D}{2D} = (1.84 \pm 0.02) \times 10^{-3} / k \text{ atm.}$$

$$\left| \frac{\Delta (g - g_0)_z}{(g - g_0)_z} \right| \leq 2.5 \times 10^{-3} / k \text{ atm.}$$

V^{2+}:

$$\frac{\Delta 2D}{2D} = (1.77 \pm 0.1) \times 10^{-3} / k \text{ atm.}$$

where D is the coefficient of the crystalline field term in the spin Hamiltonian which behaves under rotation like the spherical harmonic Y_{20} and $(g-g_o)_z$ is the difference in the g value parallel to the crystalline axis and the free ion g value.

From this it was concluded that the ions occupy similar lattice sites, though possibly including the displacements proposed in the literature, and are subject to the same compressibility, comparable to that of the bulk compressibility. Comparison with the point charge model led to the conclusion that the point charge model was inadequate to predict the observed pressure changes. A molecular orbital calculation as a function of surrounding ion position and further experiments are suggested.

Chapter I

INTRODUCTION

A. MOTIVATION, OBJECTIVES, AND RESULTS

Interest in solid-state systems has become widespread in recent years, particularly with the use of doped semiconductors as transistors and paramagnetically doped crystals for MASERS and LASERS. Electron paramagnetic resonance (EPR) utilizes a paramagnetic impurity ion in a host lattice as a means of studying both the ion itself and its interaction with the surrounding lattice. The iron group ions are particularly advantageous with their partially filled 3d electron shells and resulting net magnetic moment. Microwaves (ca. 3 cm. wavelength) incident upon the crystal induce magnetic dipole transitions among the magnetic sublevels of the ground state in a strong magnetic field (ca. 3000 gauss). The crystalline field at the impurity ion site due to the surrounding ions or ligands also perturbs the impurity ion states. From the resonance absorption of microwave power for transitions between various energy levels, electronic and nuclear properties of the impurity ion in its host lattice can be deduced. For texts on EPR one may consult Low,[1] Pake,[2] Ingram,[3,4] and Shlichter,[5] as well as the reviews by Bleaney and Stevens,[6] Bowers and Owen,[7] and Jarrett.[8]

The mechanism of the interaction between the crystalline field and the impurity ion needs further study. In order to study the interaction, the usual method is to observe the changes in spectra between similar or isoelectronic ions in the same lattice[9,10,11] or the same ion in a series of lattices with similar symmetry.[12,13] Hydrostatic pressure (ca. 10,000 atmospheres) provides a means of linearly changing the crystalline field at the impurity ion site by compressing the host lattice. Thus it is a powerful means of studying the interaction between the two.

It is the object of this study to determine the hydrostatic pressure dependencies of the EPR spectra of the triply ionized chromium ion (Cr^{3+}) and the doubly ionized vanadium ion (V^{2+}), which are isoelectronic, in the α-Al_2O_3, or sapphire, lattice. The results are interpreted utilizing the crystalline field model in the hope of further understanding the behavior of zero field splitting with a linear lattice change for isoelectronic ions. Additional objectives are to check on the substitutional positions of the impurity ions in the lattice and to determine the usefulness of the crystalline field model. This study is also another step in a thorough examination of the solid state chemistry of vanadium.

It is found that the zero field splitting for both Cr^{3+} and V^{2+} in sapphire varies linearly with pressure to 6000

atmospheres, and the relative change for both ions is nearly the same. From this it is concluded that the ions occupy similar lattice sites and are subject to similar local compressibilities, comparable to that of the bulk compressibility. It is also concluded that the point charge model is inadequate to predict the observed pressure changes, and a molecular orbital calculation and further experiments are suggested.

B. LITERATURE REVIEW

Review of Previous High Pressure Resonance Experiments. An S-state ion, such as Mn^{2+} whose L = 0, should have no low order mechanism to cause zero field fine structure splitting. The observed splittings[14] aroused a great deal of curiosity about the effect of the crystalline field as a perturbation on the energy levels of an impurity ion.[15,16,17] Among the resulting papers, Watanabe suggested that the non-zero contributions due to a crystalline field of cubic symmetry must be from matrix elements containing only even powers of the crystalline field.[18] He also suggested that this could be checked by a hydrostatic pressure experiment on the EPR of such a material.[19] Walsh performed such an experiment and found a quartic dependence on the cubic field for both Mn^{2+} and Fe^{3+} in MgO[20] assuming that local and bulk compressibilities are equal. A paper by Powell, Gabriel,

and Johnston then suggested a mechanism for ground state splitting due to odd powers of the crystalline field.[21] In another hydrostatic pressure EPR experiment, Wait found a square dependence on the cubic crystalline field for Mn^{2+} in calcite and a first power dependence on the axial crystalline field.[22] He also pointed out that according to the theory of Powell et al. Mn^{2+} and Fe^{3+} should not necessarily have the same pressure dependence in MgO,[21] and suggested further experiments on Fe^{3+} in calcite as well as studies in other host lattices. All the calcite samples which could be obtained for study contained too low a concentration of iron to allow a determination of the pressure dependence. Other hydrostatic EPR experiments have been done recently by Rimai, Deutsch, and Silverman[23] on Fe^{3+}, Cr^{3+}, Gd^{3+}, and Eu^{2+} in cubic $SrTiO_3$. They conclude a local compressibility twice that of the bulk compressibility about the impurity sites in $SrTiO_3$. Blum and Benedek[24] have also reported their results for the pressure dependence of the hydrogen atom's hyperfine interactions in the CaF_2 lattice.

Recently several uniaxial pressure experiments have been done on the EPR and nuclear magnetic resonance (NMR) spectra of ruby but are mostly yet unpublished. Viegele and Stettler[25] have studied the effects of uniaxial stress and temperature on the NMR spectra of ruby. Terhune[26]

and Donoho[27] have studied the EPR spectra of ruby under uniaxial stress, and their results are correlated in Chapter V with those obtained in this study. Tucker[28] has performed a spin-phonon interaction experiment on ruby whose results can also be correlated as a uniaxial pressure experiment as will be shown later. A uniaxial pressure experiment on the EPR of Nd^{3+} and U^{3+} in CaF_2 has also been reported by Black and Donoho.[29]

An optical resonance experiment using uniaxial stress on MgO with Cr^{3+} was performed by Schawlow, Piksis, and Sugano[30] to try to understand the charge compensation required when Cr^{3+} substitutes for Mg^{2+}. Sturge[31] followed with a similar experiment with V^{2+} in MgO. These optical studies were used by Walsh in the interpretation of his EPR experiment. Drickamer et al. have also done optical studies using uniaxial pressures up to 150 kbar.[32,33,34] They have found increases in the crystalline field parameter, Dq, which are consistent with the R^{-5} law and similar pressure dependencies for various ions in the same lattice. Also, they indicate small changes in the interelectronic repulsion Racah B parameter.

<u>High Pressure Resonance Experiments on Cr^{3+} and V^{2+} in Sapphire</u>. The pressure experiments which are compared analytically or discussed qualitatively with the present experiment are now briefly summarized. Two EPR experiments

on ruby (Cr^{3+} in sapphire) subject to uniaxial stress have been done but not reported in the literature. Terhune[26] has communicated his results for the change in the zero field splitting, 2D (2D = -.38 cm.$^{-1}$), for stress parallel (//) and perpendicular ($\perp$) to the c axis of the crystal as follows:

$$\left(\frac{\Delta D}{D}\right)_{\parallel} = 5.2 \pm 0.3 \times 10^{-3} / \text{k atm.}$$

$$\left(\frac{\Delta D}{D}\right)_{\perp} = 3.8 \pm 0.3 \times 10^{-3} / \text{k atm.}$$

He did not observe a change in the g value. Donoho[27] has indicated that he also could not observe any changes in the g shift for uniaxial stress and his experimental limit yields

$$\frac{\Delta (g - g_0)_z}{(g - g_0)_z} \leq 2 \times 10^{-3} / \text{k atm.}$$

A third EPR experiment has been reported in progress[35] but the nature of the stress and quantitative results are unavailable.

The optical resonance study of ruby under pressure was done by Stephens and Drickamer.[36] They report a change in the cubic field splitting, Dq (10 Dq = 18,000 cm.$^{-1}$), of

$$\left(\frac{\Delta Dq}{Dq}\right) = 0.6 \times 10^{-3} / \text{k atm.}$$

and a distinct increase in the trigonal splitting parameter, K(K = -350 $cm.^{-1}$), above 60 katm. This change in Dq was shown to be equivalent to 30 katm. to that expected from a simple change in the metal-ligand distance, R, from the compressibility data and the relation

$$10\,Dq = 4\,q\,\langle r^4\rangle / 3\,R^5$$

where q is the ligand charge and $\langle r^4 \rangle$ is the integral of r^4 over the radial 3d wave functions. From the change in Dq they determine a change in the interelectronic repulsion parameter, B(B = 630 $cm.^{-1}$), of

$$\frac{\Delta B}{B} = -0.32 \times 10^{-3} / k\ atm.$$

They also conclude that the decrease in B shows an increase in covalency and the change in K indicates the onset of distortion above 60 katm.

The effect of uniaxial stress on the electric field gradient, q, at the impurity was reported by Viegele and Stettler[25] from an NMR experiment in ruby. They report

$$\left(\frac{\Delta q}{q}\right)_{\parallel} = +3.2 \times 10^{-3} / k\ atm.$$

and

$$\left(\frac{\Delta q}{q}\right)_{\perp} = -2.7 \times 10^{-3} / k\ atm.$$

but their analysis of these values has not been published.

One other experiment which can be correlated with this study as a pressure experiment is the spin-phonon interaction in ruby performed by Tucker.[28] He analyzes the perturbation, $\mathcal{H}'$, with the form

$$\mathcal{H}' = G\, e_{zz}\, S_z^2$$

where G is defined as the magneto-elastic coupling constant and e_{zz} is the strain. He reports values[26] of G^2

$$G_{\parallel}^2 = 2.8 \times 10^{-30} \quad ergs^2$$

$$G_{\perp}^2 = 1.2 \times 10^{-30} \quad ergs^2$$

for longitudinal waves parallel and perpendicular to the c axis.

To the author's knowledge there are no pressure-resonance experiments for V^{2+} in sapphire and no others for ruby.

Studies of Cr^{3+} and V^{2+} in Sapphire. A great deal of work has been published for ruby because of its wide application in recent LASER and MASER technology Summarized below are only those fundamental studies and related works which are used in the analysis of this problem. A summary of the crystal field parameters of the iso-electronic ions is given in Table V.

The EPR spectra of Cr^{3+} and V^{2+} in sapphire are reported by E.O. Schulz-DuBois[37] and Lambe and Kikuchi[38], respectively. More recent evaluations of the spin Hamiltonian parameters are summarized by Laurence and Lambe[39] for an ENDOR (electron nuclear double resonance) experiment to study the quadrupole interactions in sapphire. The electric field gradients determined in their experiment are also used in the discussion in Chapter V.

The optical spectrum of ruby was studied by Sugano and Tanabe[40] and interpreted with qualitative success (except for the zero field splitting) by crystal field theory. More recent discussions of the optical spectrum of ruby and similar structures and ions are by Wood, et al[13] and Weakliem and McClure.[41] From his studies of the optical spectrum McClure[42] has suggested that the chromium ion is not substitutional for an aluminum. The optical spectrum of V^{2+} in sapphire is reported by Sturge[43] along with the collected optical parameters for the other isoelectronic ions, Cr^{3+} and Mn^{4+}.

Molecular orbital theory was used by Lohr and Lipscomb[44] to study theoretically the spectra of Cr^{3+} in various crystals, including sapphire. Using a semiempirical LCAO-MO method they qualitatively predict the observed spectra with some improvement over the crystal field theory in the value of the zero field splitting. Their theory

was used by Royce and Bloembergen[45] to analyze electric field effects on the EPR spectrum of ruby with good success.

The sapphire crystal structure was obtained from Wyckoff[46] and the most recent compilation of elastic constants is by Bernstein.[47] One other reference that should be mentioned is a discussion of the expansion of the impurity ion wave functions upon insertion of the ion into a lattice by Marshall and Stuart,[48] since according to them, this would be expected with lattice compression. They show that the reduction of the spin-orbit coupling parameter, λ , of an ion upon insertion into a lattice is due to radial expansion of the electron wave functions and support their arguments with neutron scattering form factors and super-hyperfine experiments.

Chapter II

THEORY

A. THE HAMILTONIAN, ENERGY LEVELS, AND TRANSITIONS

A phenomemological Hamiltonian called the "spin Hamiltonian"[49,50] is usually used to interpret the experimental results of current research in electron paramagnetic resonance. It arises in the following manner. A "free ion" Hamiltonian is obtained much in the manner of the helium atom[51] by a summation of the electron momenta, the coulomb interactions between the nucleus and individual electrons and the coulomb interations between electrons. This Hamiltonian can be used to obtain the wave functions for the determination of the perturbation caused when this "free ion" is inserted in a crystalline field and an external magnetic field. The crystalline field is produced by the charges or dipoles from the surrounding ligands. The perturbing Hamiltonian -- due to the crystalline field, the external magnetic field, and the remaining intra-ionic interactions -- to which the free ion wave functions are applied becomes with simplification the spin Hamiltonian.

In the free ion case the wave functions are the product or a linear combination of permutations of the product (Slater determinant) of one electron "orbitals." The equations for the one electron orbitals, Hartree or

Hartree-Fock equations respectively, are determined by applying a variational method to the Schroedinger equation of the free ion. A more inclusive approach is to allow some "linear combination of atomic orbitals" (LCAO) with orbitals from a neighboring ligand or excited states of the impurity ion. This allows the wave functions to contain contributions of higher lying states of the ion of the proper symmetry and wave functions from neighboring ligands, as in the "molecular orbital" calculations currently in such wide use.[52,53,44] This type analysis is not used here primarily because the shift in the Hamiltonian parameters is of concern rather than the exact determination. (In fact, the comparison analysis used precludes a prior knowledge of the parameters, and that their previous determination has fit the spin Hamiltonian well.)

An outline of the usual derivation of the spin Hamiltonian is shown below. It is followed by the restriction of the spin Hamiltonian to a $3d^3$ ion in sapphire and the resulting energy levels and transitions are then derived.

The General Hamiltonian. From the general Hamiltonian for a single electron moving in electric and magnetic fields obtained from Dirac's theory, one can generalize further to obtain a Hamiltonian for many electrons in an atom with external perturbations by appropriate summations of interactions with the nucleus and other electrons.[54]

Specification of the external perturbing fields and potentials then allows for the interactions of the atomic system when placed in the crystalline environment and magnetic field. This method does not include effects of the nucleus interacting with the external fields. The interaction of the nuclear electric quadrupole moment with the crystalline electric field and the nuclear magnetic dipole interaction with the external magnetic field must be added as further perturbations. Only the electrons in the unfilled shell, such as the 3d shell for the iron group transition elements, usually are considered. Because in resonance studies only the effects of the crystalline field and the magnetic behavior of the electrons and nuclei are of primary interest, this general Hamiltonian can be further simplified as will be shown.

Following the above discussion one obtains the Hamiltonian shown in equation 1,

$$\mathcal{H} = \mathcal{H}_o + \mathcal{H}_{CF} + \mathcal{H}_{LS} + \mathcal{H}_{SS} + \mathcal{H}_e + \mathcal{H}_N + \mathcal{H}_n + \mathcal{H}_Q \qquad (1)$$

where

$$\mathcal{H}_o = \sum_i \left(\frac{p_i^2}{2m} - \frac{Z e^2}{r_i} \right) + e^2 \sum_{k>i} \frac{1}{r_{ik}}$$

$$\mathcal{H}_{CF} = -eV_{CF} = -e\left(V_{Cubic} + V_{Axial}\right)$$

$$\mathcal{H}_{LS} = 2 Z \beta^2 \sum_i \left(\underline{l}_i \cdot \underline{s}_i \right) r_i^{-3}$$

$$\mathcal{H}_{ss} = 2\beta^2 \sum_{k,i\neq k} \left\{ (\underline{s}_i \cdot \underline{s}_k)\, r_{ik}^{-3} - 3(\underline{s}_i \cdot \underline{r}_{ik})(\underline{s}_k \cdot \underline{r}_{ik})\, r_{ik}^{-5} \right\}$$

$$\mathcal{H}_e = \beta\, \underline{H} \cdot \sum_i (\underline{\ell}_i + 2\underline{s}_i)$$

$$\mathcal{H}_N = 2 g_N \beta_N \beta\, \underline{I} \cdot \sum_i \left\{ \frac{\ell_i(\ell_i+1)}{j_i(j_i+1)\, r_i^3}\, \underline{j}_i + \frac{2\delta(r_i)}{3\, r_i^2}\, \underline{s}_i \right\}$$

$$\mathcal{H}_n = -g_N \beta_N\, \underline{H} \cdot \underline{I}$$

$$\mathcal{H}_Q = \frac{e^2 Q}{2I(2I-1)} \sum_i \left\{ I(I+1)\, r_i^{-3} - 3(\underline{I} \cdot \underline{r}_i)^2\, r_i^{-5} \right\} + \frac{3eQ}{4I(2I-1)} \frac{\partial^2 V_{cF}}{\partial z^2} \left\{ I_z^2 - \frac{I(I+1)}{3} \right\}$$

where V_{cf} is the crystalline field and the rest of the symbols are standard notation. The terms in equation 1 and the order of magnitude of the resulting energy level separations are as follows in order: the well known Hamiltonian of a many particle system with coulomb interactions, 10^5 cm.$^{-1}$; the crystalline field term, widely variable, but in our case of iron group series 10^3 - 10^4 cm.$^{-1}$; spin-orbit interaction 10^2 cm.$^{-1}$; spin-spin interaction, 1 cm.$^{-1}$; the electron Zeeman interaction with external magnetic field, 1 cm.$^{-1}$; the interaction of the nuclear magnetic moment and the magnetic field produced by the electrons, 10^{-2} cm.$^{-1}$; nuclear Zeeman interaction with the

external magnetic field, 10^{-3} cm.$^{-1}$; and the nuclear electric quadrupole interaction with the electrons and the crystalline field, 10^{-4} cm.$^{-1}$, in which axial symmetry has been assumed.

The Wave Functions. For most transition metal ions the first term, $\mathcal{H}_0$, in the total Hamiltonian is used to obtain wave functions to use in determining the perturbation due to the remaining terms. The last term in $\mathcal{H}_0$, the inter-electron coulomb repulsion, prevents exact solutions for the radial part of the wave functions, which are left as empirically determined parameters. Certain combinations of these radial integrals resulting from a spherical harmonically expanded interelectron potential are the empirical Racah A, B, and C parameters[55] which are used experimentally later on. (See Appendix F.)

The angular part of the wave functions is soluble and group theory provides a powerful means of simplifying the problem of the impurity ion in the crystal before solving by eliminating the need to consider many combinations of wave functions. This arises because the total Hamiltonian must be invariant under the coordinate transformations which preserve symmetry since a physically observable quantity must not depend upon the choice of coordinates. For a free ion any inversion or infinitesimal rotation or combination preserves the symmetry, but in a crystal it

is only that group of symmetry operations that preserve crystal symmetry about the impurity ion. Thus simplification arises if one uses those combinations of wave functions which transform among themselves according to the irreducible representations of the symmetry group of the impurity ion site. Other representations are just combinations of the irreducible representations. The transformation properties of these irreducible representations are represented by a matrix for each of the symmetry operations. Since only the trace, or character, is used in applications, these properties are given in a character table. (For example, see Heine.[56])

These group theory arguments can still be used when considering only part of the total Hamiltonian because an energy perturbation is also a physically observable quantity. In these cases the product of representations in the matrix element evaluation of $\mathcal{H}_{pert.}$ ($\mathcal{H}_{pert.}$ also transforms as one of the irreducible representations) must contain the identity representation or the energy perturbation would not be invariant under a symmetry preserving transformation of coordinates and the matrix element would have to be zero. Examples will be shown as they arise and the character tables of the cubic O_h group and the trigonal C_3 group are shown in Appendix F along with the O_h irreducible representation product table.

If a simple ionic model of the lattice is assumed, the wave functions, Ψ , are made up of products of one electron impurity ion orbitals, ϕ_i . If the covalent nature of the lattice is to be accounted for, the orbital of an unpaired electron must contain some of the ligand orbital, ϕ_l , or

$$\phi = \alpha \phi_i + \beta \phi_l \qquad (2)$$

where $\alpha^2+\beta^2 \cong 1$ if the overlap is small. Thus β^2 , or the amount of mixing of the ligand orbital, is a measure of covalency.

The Cubic Field. It is generally useful to decompose V_{cf} into a higher symmetry V_1 and a lower symmetry V_2 and determine the energy levels of $\mathcal{H}_o - eV_1$ with the free ion wave functions and then apply V_2 plus the rest of the terms in equation 1 as a perturbation on these levels. As will be seen later, sapphire is primarily cubic with some axial distortion so V_1 and V_2 become V_{cub} and V_{ax}, respectively. The result of the first part of this procedure for a $3d^3$ ion such as Cr^{3+} and V^{2+} is shown as a function of cubic crystalline field strength, Dq, in Figure 1.[13] The free ion energy levels are indicated at Dq = 0. [The notation of the levels corresponds to the transformation properties of the wave functions (i.e. the irreducible representation of the cubic group

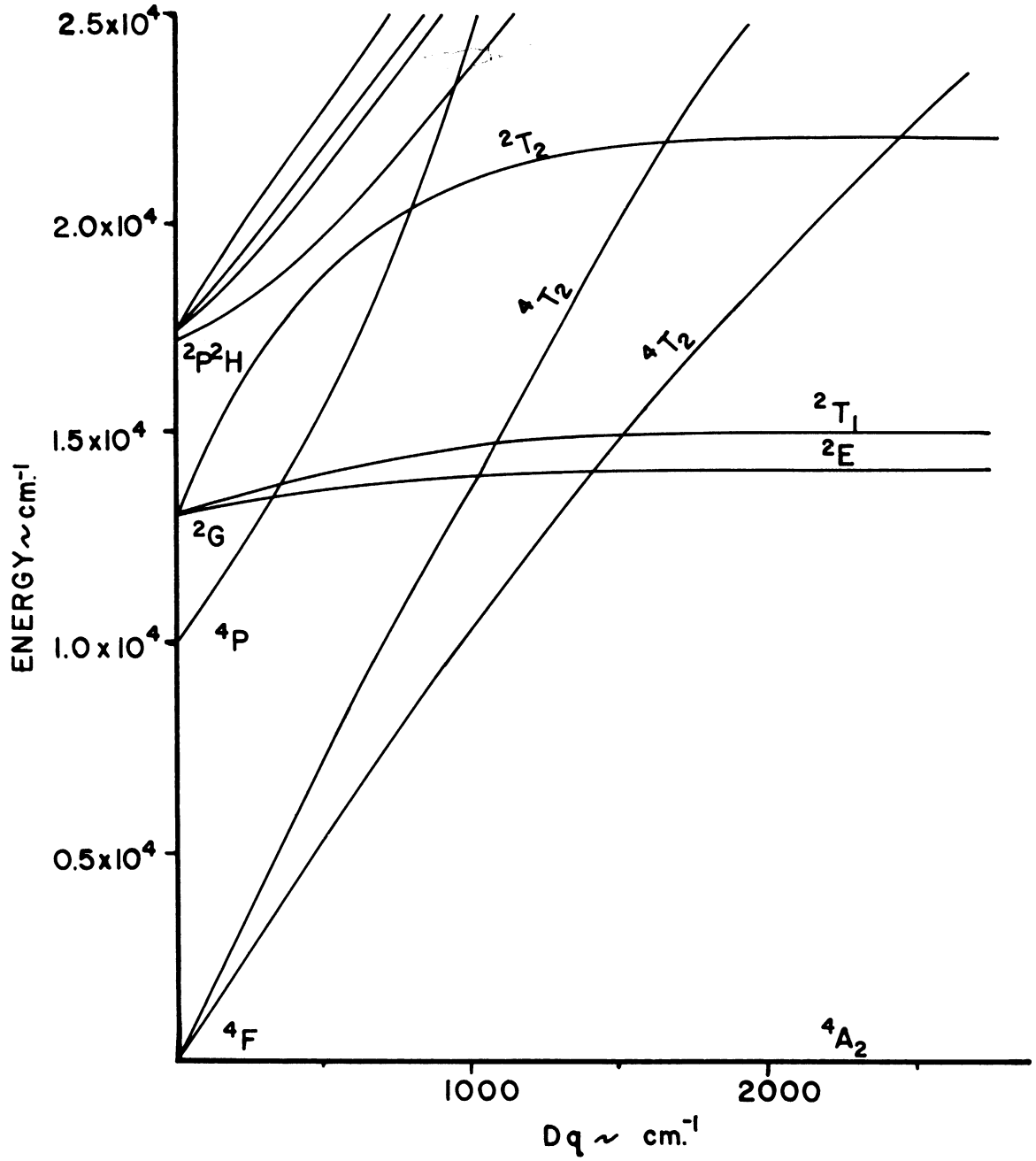

Figure 1. Energy levels of a $3d^3$-^{4}F-state ion versus cubic crystalline field.

to which the wave functions belong) which result in that energy level when applied to the Hamiltonian $\mathcal{H}_o - eV_1$. The superscript is the spin multiplicity, 2 S + 1.] The value of Dq for ruby, for example, is 1,800 cm.$^{-1}$ and the resulting energy levels are shown in Figure 2, where the usual optical transitions are indicated. As will be shown later, the additional noncubic or axial crystalline field and spin orbit coupling will cause further small splitting. In the $^4A_2$ ground state this becomes the "zero field splitting" of about 0.38 cm^{-1}, and for the ^2E level a splitting of about 29 cm.$^{-1}$ results in the well known R_1 and R_2 red lines of ruby. The result is similar for the V^{2+} ion.

The Spin Hamiltonian. It remains now to apply the perturbations of V_{ax} and remaining terms of equation 1, $\mathcal{H}_{LS}$ and on , to the wave functions of the $^4A_2$ ground state. Since there is only one combination of wave functions which transforms like the A_2 irreducible representation, this state is effectively an orbital singlet and thus it has an orbital expectation value of zero. Also, since $\mathcal{H}_{LS}$ is a smaller perturbation than the inter-electron repulsion term of $\mathcal{H}_o$ an LS type coupling scheme is applicable and M_l and M_s are good quantum numbers. Assuming constant total $\underline{L} = \sum_i \underline{l}_i$ and $\underline{S} = \sum_i \underline{s}_i$, Stevens[57] has shown that the position coordinates can be replaced by the components of $\underline{L}$ and the individual electron spin variables by the components

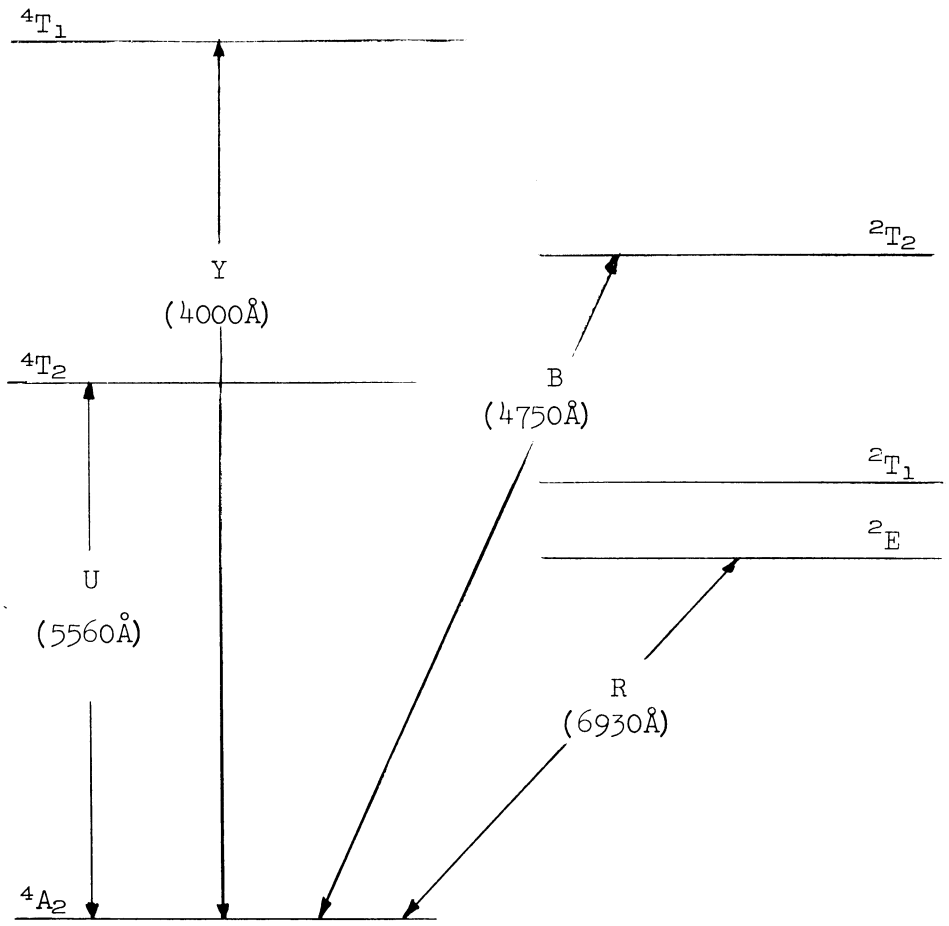

Figure 2. Energy levels of ruby with cubic field.

of S. With the further assumption that the next higher cubic field level to the $^4A_2$ ground state is far away (optical transitions as compared to microwave), the change in energy of the ground state can be calculated to second order using only the orbital part of the wave function.

Thus we have the eigenvalue problem

$$\mathcal{H}\,\Psi_{q,m_s,m_I} = E_{q,m_s,m_I}\,\Psi_{q,m_s,m_I} \qquad (3)$$

where Ψ are those combinations of the free ion wave functions, Φ, which transform as the irreducible representations of the cubic point group, where

$$\Phi_{q,m_s,m_I} = R_n(r)\,Y_{L\,m_l}\,\chi_{S\,m_s}\,\Lambda_{I\,m_I}$$

and q stands for the quantum numbers n, L, S, I, and m_l, and R(r) is the radial dependence and Y, χ, and Λ are the eigenfunctions of the angular momentum operators L, S, and I, respectively. With

$$\mathcal{H} = \mathcal{H}_o - e\,V_{CUB} + \mathcal{H}_{PERT} \qquad (4)$$

one obtains

$$E_{q\,m_s m_I} = E_q + \langle q\,m_s\,m_I|\mathcal{H}_{PERT}|q\,m_s\,m_I\rangle + \sum_{q'm_s'm_I' \neq q\,m_s m_I} \frac{\langle q\,m_s\,m_I|\mathcal{H}_{PERT}|q'm_s'm_I'\rangle\langle q'm_s'\,m_I'|\mathcal{H}_{PERT}|q\,m_s\,m_I\rangle}{E_q - E_{q'}} \qquad (5)$$

where E_q are the eigenvalues of $\mathcal{H}_o - e V_{cub}$. Since only the small changes in the ground state due to the crystalline and magnetic fields are of interest, E_q can be dropped. The calculation performed to second order over the orbital part of the wave function for the orbital singlet ground state yields

$$\langle m_s m_I | \mathcal{H}_{SPIN} | m_s' m_I' \rangle = \langle 0\, m_s m_I | \mathcal{H}_{PERT} | 0\, m_s' m_I' \rangle + \sum_{q'' m_s'' m_I'' \neq q m_s m_I} \frac{\langle 0 m_s m_I | \mathcal{H}_{PERT} | q'' m_s'' m_I'' \rangle \langle q'' m_s'' m_I'' | \mathcal{H}_{PERT} | 0 m_s m_I \rangle}{E_q - E_{q''}} \quad (6)$$

This eliminates the orbital operator and leaves only spin operators in the "spin Hamiltonian" as follows.

Considering the last six terms in equation 1 as the perturbation one obtains

$$\mathcal{H}_{PERT} = \lambda \underline{L} \cdot \underline{S} + \beta \underline{H} \cdot (\underline{L} + 2\underline{S}) + A \underline{I} \cdot \underline{S} - g_N \beta_N \underline{H} \cdot \underline{I} + Q' \left[I_z^2 - \tfrac{1}{3} I(I+1) \right] \quad (7)$$

where spin-spin interactions among the electrons and the electronic interaction with the nuclear quadrupole moment have been neglected. (For a more general discussion see Bleaney and Stevens.[6]) Since V_{ax} will be shown to be of the form $\left[L_z^2 - \tfrac{1}{3} L(L+1) \right]$ its matrix element with the

orbital singlet ground state, $^4A_2$ is zero. Also, since V_{ax} transforms as the irreducible representation E of the cubic group and the products $T_1 \times E \times A_2$ and $T_2 \times E \times A_2$ do not contain the identity representation (see Appendix F), the axial field does not connect the excited orbital states $^4T_2$ and $^4T_1$ in the second order perturbation which follows. Therefore it is dropped from the spin Hamiltonian but must be applied to the higher orbital states before the second order perturbation calculation.

Since the expectation value of L_z for the orbital singlet ground state is zero the first order part of the spin Hamiltonian from equations 6 and 7 is

$$\left(\mathcal{H}_{SPIN}\right)_{1st} = 2\beta \underline{H}\cdot\underline{S} + A\,\underline{I}\cdot\underline{S} - g_N\beta_N \underline{H}\cdot\underline{I} + Q'\left[I_z^2 - \tfrac{1}{3}I(I+1)\right]$$

The second order contributions from $\mathcal{H}_{PERT}$ will arise through $\underline{L}$ and will contain terms quadratic in the components of $\underline{H}$ and $\underline{S}$ or

$$\left(\mathcal{H}_{SPIN}\right)_{2nd} = \lambda^2 d_{ij} S_i S_j + \lambda\beta f_{ij} H_i S_j + \beta^2 \Lambda_{ij} H_i H_j$$

where the d_{ij}, f_{ij}, and Λ_{ij} are matrices made up of the orbital matrix elements connecting the i and j components with the excited states. (For example, the calculation of the d_{ij} is outlined in Chapter II - E and performed in Appendix G.) The last term, quadratic in H, represents a constant energy and can be dropped.

Combining the first and second order contributions in a tensor notation in which $\underline{\underline{D}} = \lambda^2 d_{ij}$ and $\underline{\underline{g}} = 2\delta_{ij} + \lambda f_{ij}$ yields

$$\mathcal{H}_{SPIN} = \beta \underline{H} \cdot \underline{\underline{g}} \cdot \underline{S} + \underline{S} \cdot \underline{\underline{D}} \cdot \underline{S} + \underline{I} \cdot \underline{\underline{A}} \cdot \underline{S} + \underline{I} \cdot \underline{\underline{Q}} \cdot \underline{I} - \beta_N \underline{H} \cdot \underline{\underline{g}}_N \cdot \underline{I} \qquad (8)$$

The g's, D, A, and Q are tensors whose principal axes are assumed to coincide. This spin Hamiltonian when diagonalized will yield all the energies arising from the various perturbations and therefore show all the resonance properties of the system. The first, or Zeeman, term in equation 7 contains the gyromagnetic ratio or spectroscopic splitting factor, g, which will differ from the free electron value of 2.0023 due to admixing of higher orbital states. Anisotropy of g may arise through the mixing of the spin-orbit and crystalline field interactions. The second, or fine structure, term is a measure of the further splitting, D, of the ground state from asymmetric or non-cubic contributions of the crystalline field. This also arises through spin orbit coupling as detailed in Chapter II-E, and is called the "zero field splitting." The third, or hyperfine, term gives a measure, A, of the interaction of the nuclear magnetic moment with the magnetic field of the electrons. The nuclear electric quadrupole and magnetic dipole interactions with the crystalline and magnetic fields, respectively, are expressed by Q and g_n in the last two terms.

The Spin Hamiltonian for a $3d^3$ Ion in Sapphire. The spin Hamiltonian must have the same symmetry as that of the crystalline field, in this case axial symmetry. It will be seen later that the crystalline field can be expanded in the spherical harmonics, Y_{lm}, with many restrictions on the number of terms. The expansion of the axial field about a $3d^3$ ion with S = 3/2 yields only the one spherical harmonic, Y_{20}, so the spin Hamiltonian spin operators that obey axial symmetry must also transform under rotation like Y_{20}. Racah noted[58] that the vector operator T^1_m, which has the same transformation properties as Y_{1m}, obeys the recursion relation

$$T^l_{m-1} = [l(l+1) - m(m-1)]^{-1/2} [S_-, T^l_m]$$

with the angular momentum operator S. From this one can obtain linear combinations of the spin operators which have the same transformation properties as the spherical harmonics, assuring the same symmetry for the spin Hamiltonian as the crystalline field. Examples of such linear combinations, S_{lm}, are

$$S_{20} = S_z^2 - \tfrac{1}{3} S(S+1)$$

and

$$S_{40} = -\frac{1}{180}\left[35S_z^4 - 30S(S+1)S_z^2 + 25S_z^2 - 6S(S+1) + 3S^2(S+1)^2\right]$$

Thus equation 7 with the crystalline field axis as the z axis becomes

$$\mathcal{H}_{SPIN(AX)} = \beta\left[g_z H_z S_z + \tfrac{1}{2} g_\perp (H_+ S_- + H_- S_+)\right] + D\left[S_z^2 - \tfrac{1}{3}S(S+1)\right]$$
$$+ A I_z S_z + \tfrac{1}{2} B(I_+ S_- + I_- S_+) + Q'\left[I_z^2 - \tfrac{1}{3}I(I+1)\right]$$
$$- \beta_N\left[g_{Nz} H_z I_z + \tfrac{1}{2} g_{N\perp}(H_+ I_- + H_- I_+)\right] \qquad (9)$$

or

$$\mathcal{H}_{SPIN(AX)} = \beta\left[g_z H_z S_z + g_\perp (H_x S_x + H_y S_y)\right] + D\left[S_z^2 - \tfrac{1}{3}S(S+1)\right]$$
$$+ A I_z S_z + B(I_x S_x + I_y S_y) + Q'\left[I_z^2 - \tfrac{1}{3}I(I+1)\right]$$
$$- \beta_N\left[g_{Nz} H_z I_z + g_{N\perp}(H_x I_x + H_y I_y)\right] \qquad (10)$$

where g_z equals the g_{zz} component of the g tensor and $g_\perp = g_{xx} = g_{yy}$.

The Energy Levels for a $3d^3$ Ion in Sapphire. It remains only to apply this spin Hamiltonian to the eigenvalue problem

$$\mathcal{H}_{SPIN}\ \Psi_{m_s m_I} = E_{m_s m_I}\ \Psi_{m_s m_I} \qquad (11)$$

where $\Psi_{m_s m_I}$ now only need contain χ_{m_S} and Λ_{m_I} This yields the eigenvalues to second order in the hyperfine interaction with the magnetic field parallel to the crystalline field axis of

$$E_{M,m} = g_z \beta H M + D\left[M^2 - \tfrac{1}{3}S(S+1)\right] + AMm - g_N \beta_N H m$$
$$+ Q'\left[m^2 - \tfrac{1}{3}I(I+1)\right] + \tfrac{1}{4}B^2 \frac{[S(S+1) - M(M+1)][I(I+1) - m(m-1)]}{-g_z\beta H - D(2M+1) + A(M-m+1)} \qquad (12)$$
$$+ \tfrac{1}{4}B^2 \frac{[S(S+1) - M(M-1)][I(I+1) - m(m+1)]}{g_z\beta H + D(2M-1) + A(m-M+1)}$$

where m_S and m_I have been replaced by M and m, respectively, to conform to standard notation.

The gross structure of these energy levels for S = 3/2 and different M with the magnetic field parallel to the crystalline axis are shown in Figure 3. These are plotted with the coordinates

$$x = \frac{G}{D'} = \frac{g_z \beta H}{-D}$$

and

$$Y_M = \frac{E_M}{D'} = \frac{E_M}{-D}$$

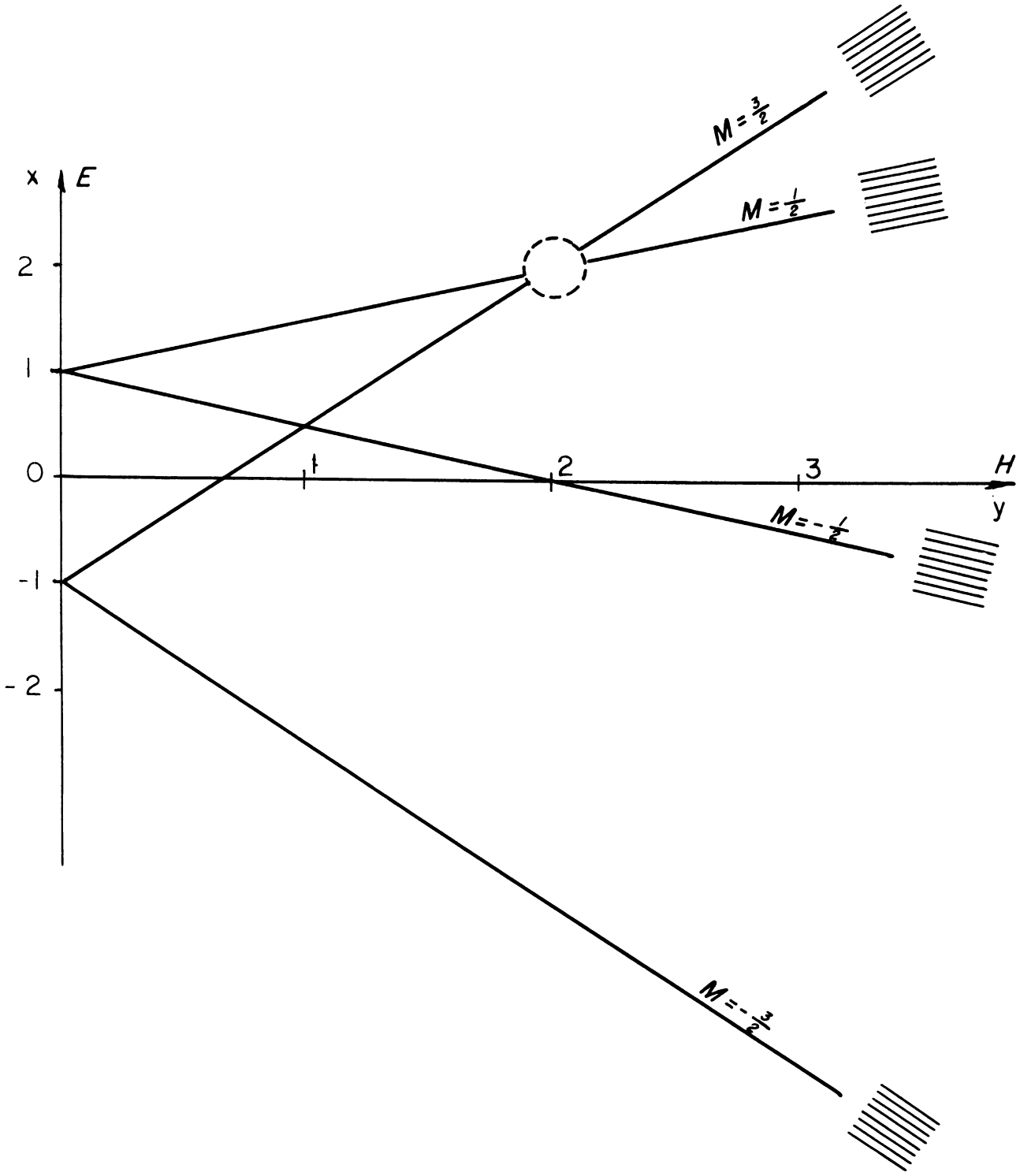

Figure 3. Energy levels of ruby ground state versus applied magnetic field.

This is done so that the plot is the same for Cr^{3+} and V^{2+} which both have S = 3/2 but have different D values. In addition, vanadium has an I = 7/2 and one isotope of chromium has an I = 3/2 which will split these levels further into 2 I+1 levels as shown in the inserts in Figure 3.

EPR Transitions for a $3d^3$ Ion in Sapphire. To induce transitions among these magnetic sub-levels with different M, a time dependent $H'(t)$ must be added to the steady field, H. Physically, this can be thought of as adding perpendicular to the steady field, H, an oscillating magnetic field vector, $H'(t)$, whose frequency is equal to the Larmor precessional frequency of the spin angular momentum. The transition probability is then proportional to the square of the matrix elements of the first and last operators in equation 7, with $H'(t)$ substituted for H. These levels of different M are connected only by the S_+ and S_- operators ($S_\pm = S_x \pm iS_y$) if the hyperfine splitting is small and the field is parallel to the crystal axis. Their matrix elements are

$$< M | S_\pm | M \mp 1 > = \left[S(S+1) - M(M \mp 1)\right]^{1/2} \quad (12)$$

Thus, the selection rule for EPR is $\Delta M = \pm 1 (\Delta m = 0)$. With this selection rule the resonance condition for the frequency of $H'(t)$, which now must be perpendicular to H, becomes

in our case

$$h\nu = E(M+1,m) - E(M,m) = g_z \beta H + D(2M+1) + A m$$

$$+\frac{1}{4} B^2 \left[I(I+1) - m(m-1)\right] \left\{ \frac{S(S+1) - (M^2+3M+2)}{-g_z \beta H - D(2M+3) + A(M-m+2)} \right. \quad (14)$$

$$\left. - \frac{S(S+1) - (M^2+M)}{-g_z \beta H + D(2M-1) + A(m-M+1)} \right\} + \frac{1}{4} B^2 \left[I(I+1) - m(m+1)\right]$$

$$\left\{ \frac{S(S+1) - (M^2+M)}{g_z \beta H + D(2M+1) + A(m-M)} - \frac{S(S+1) - (M^2-M)}{g_z \beta H + D(2M-1) + A(m-M+1)} \right\} .$$

This is the equation used to analyze the results of this study. (It should be noted that usually D and A are much smaller than $g_z \beta H$ and the second order terms can be further simplified. For Cr^{3+} and V^{2+} in sapphire D is of the same order of magnitude as $g_z \beta H$ and this is not the case.) At X band microwave frequencies (9-10 Gc/sec) and with $D \sim \nu$, it can be seen from Figure 3 that three fine structure transitions will occur at $\sim$ 100 gauss, $\sim$ 3500 gauss, and $\sim$ 7000 gauss.

For ruby a check was also performed with the magnetic field not parallel to the crystalline symmetry axis. The dominant isotope of chromium in ruby has I = 0, so the spin Hamiltonian of equation 10 simplifies to

$$\mathcal{H}_{SPIN} = \beta \left[g_z H_z S_z + g_\perp (H_x S_x + H_y S_y) \right] + D \left[S_z^2 - \tfrac{1}{3} S(S+1) \right] . \quad (15)$$

Going to the case where the field is no longer parallel to the quantization axis, one can either transform the spin Hamiltonian to a coordinate system whose axis is parallel to the applied field and use combinations of the original eigenfunctions, or perform a perturbation calculation which yields second order terms in $\sin^2\theta \frac{D^2}{g_z \beta H}$ where θ is the angle between the field and the crystal axis. For ruby $D > g_z \beta H$ and the latter doesn't converge. The former yields the following spin Hamiltonian[37]

$$\begin{aligned}\mathcal{H} = &\left(g_z \cos^2\theta + g_\perp \sin^2\theta\right) \beta H S_z \\ &+ D\left(\cos^2\theta - \tfrac{1}{2}\sin^2\theta\right)\left[S_z^2 - \tfrac{1}{3}S(S+1)\right] \\ &+ D\tfrac{1}{2}\cos\theta\sin\theta\left[e^{-i\varphi}\left(S_z S_+ + S_+ S_z\right) + e^{i\varphi}\left(S_z S_- + S_- S_z\right)\right] \\ &+ D\tfrac{1}{4}\sin^2\theta\left(e^{-2i\varphi}S_+^2 + e^{2i\varphi}S_-^2\right)\end{aligned} \quad (16)$$

The energy levels, eigenfunctions, and transitions are calculated by Schulz-DuBois[37] and the X band transitions as a function of magnetic field and the angle, θ, are shown in Figure 4. The transitions marked forbidden are forbidden only at zero degrees.

The off axis check was done primarily at the angle $\theta = 54.74^\circ$ where $\cos^2\theta = 1/3$ and the second term in equation 16 is zero and the coefficients of the last two are equal. This angle was used because the transition energies are relatively simplified to[37]

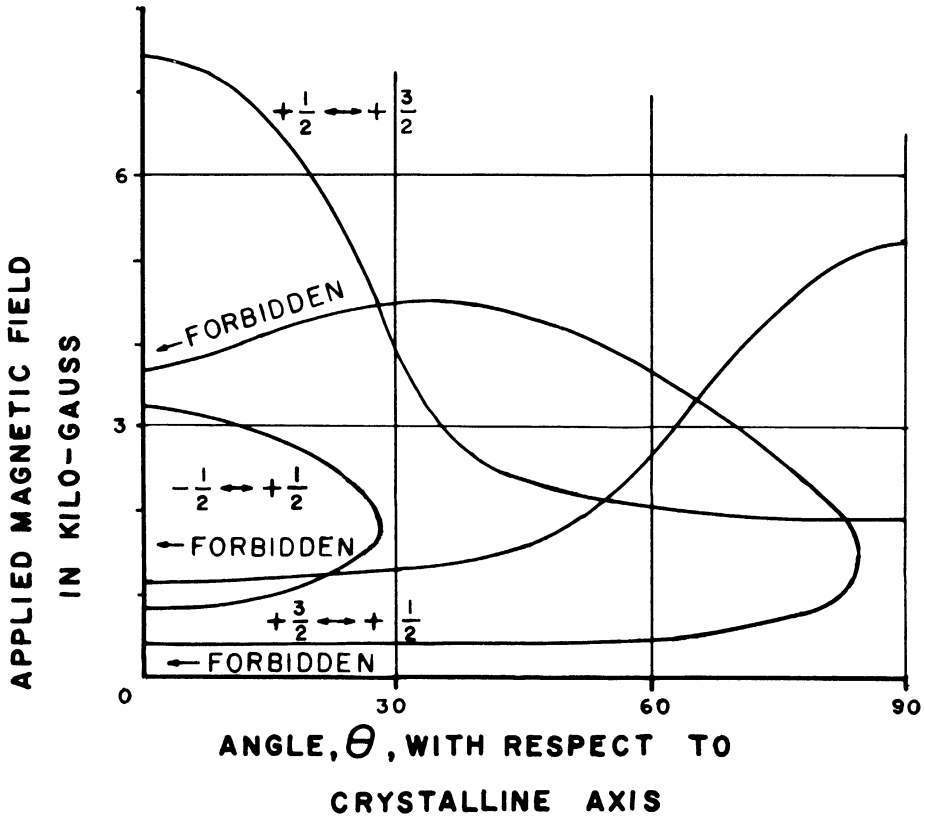

Figure 4. EPR resonances in ruby for x band as a function of applied magnetic field and the field's angle to the crystalline axis.

$$Y_{3/2} - Y_{1/2} = Y_{-1/2} - Y_{-3/2} = \left[1 + \frac{5x^2}{4} + (3x^2 + x^4)^{1/2}\right]^{1/2} - \left[1 + \frac{5x^2}{4} - (3x^2 + x^4)^{1/2}\right]^{1/2} \quad (17)$$

and

$$Y_{1/2} - Y_{-1/2} = 2\left[1 + \frac{5x^2}{4} - (3x^2 + x^4)^{1/2}\right]^{1/2} \quad (18)$$

where

$$Y_M = \frac{E_M}{-D} \; ; \; x = \frac{g_z \beta H}{-D} \; ; \text{ and } g^2 = g_z^2 \cos^2\theta + g_\perp^2 \sin^2\theta .$$

(NOTE: In equation 18, x is double valued.)

To understand the source of symmetry about the ion the sapphire crystal structure is next discussed.

B. SAPPHIRE CRYSTAL STRUCTURE

Sapphire is the commercial name for synthetic corundum which is chemically pure aluminum oxide in the alpha phase, or just $\alpha - Al_2O_3$. The gem sapphire is naturally occurring corundum with various coloring impurities to give it gem value, such as cobalt which gives the blue sapphire, vanadium the green, and chromium the red sapphire or ruby.

The crystal structure[46] can be generated by placing Al_2O_3 molecules at the corners of a cube and stretching the cube along one of the body diagonals. Another Al_2O_3 molecule which is rotated 180° about the molecular axis with respect to the others is inserted in the center of the distorted cube. Without distortion each aluminum ion would thus be at the center of six oxygens in octahedral coordination as shown in Figure 5. This results in the cubic crystalline field. The distortion along the body diagonal yields the axial or trigonal crystalline field from the inequivalent sets of three adjacent oxygens as shown in Figure 6. Three of the oxygens lie in a plane 1.37Å away from the aluminum site. The aluminum-oxygen (Al-O) distance is 1.98 Å and makes an angle of 46° 27' with the crystalline c axis. The other three oxygens are in a plane 0.80 Å away and the Al-O distance is 1.84 Å and makes an angle of 64° 10' with the c axis. In addition, the two sets of oxygens are not rotated exactly 180° with respect to each other. A projection of one set on the plane of the adjacent set (Figure 7) shows an additional rotation of 4° 22'.

The crystal belongs to the $\bar{3}$ m (or D_{3d}^6 - Shoenflies) space group and the aluminum occupies a site which has the symmetry of the 3 (or C_3) point group. The four degree offset is often neglected for which the symmetry becomes 3 m (or C_{3V}).

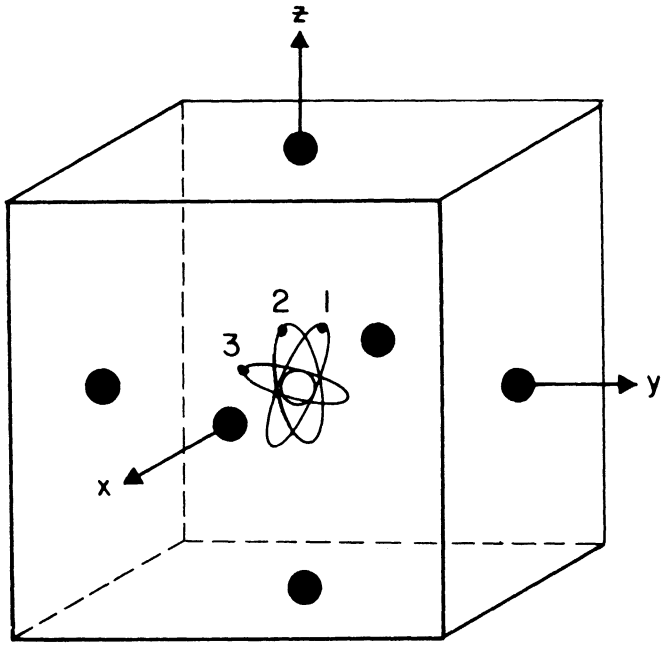

Figure 5. Octahedral coordination in ruby.

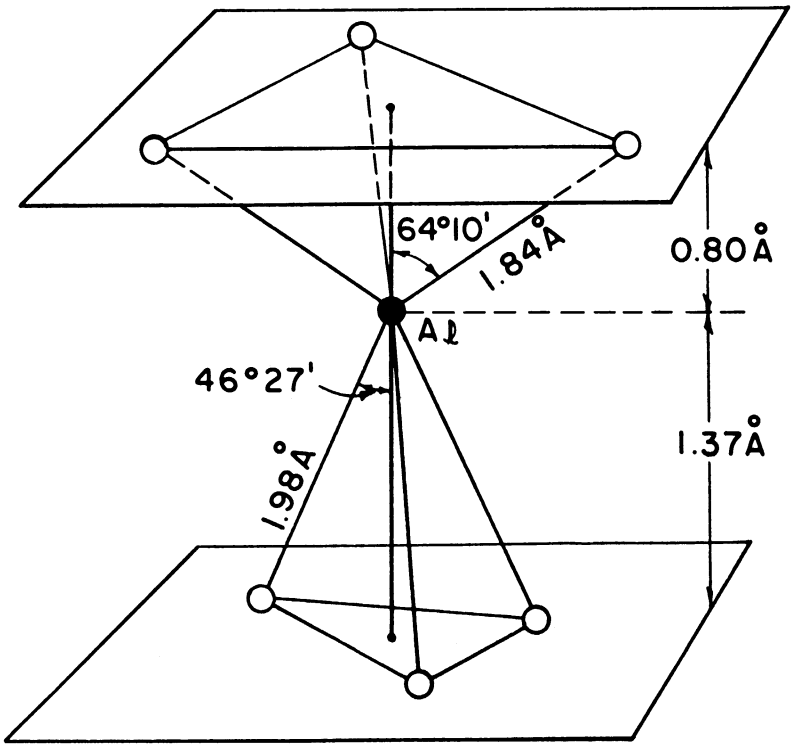

Figure 6. Crystal coordination for aluminum site in sapphire.

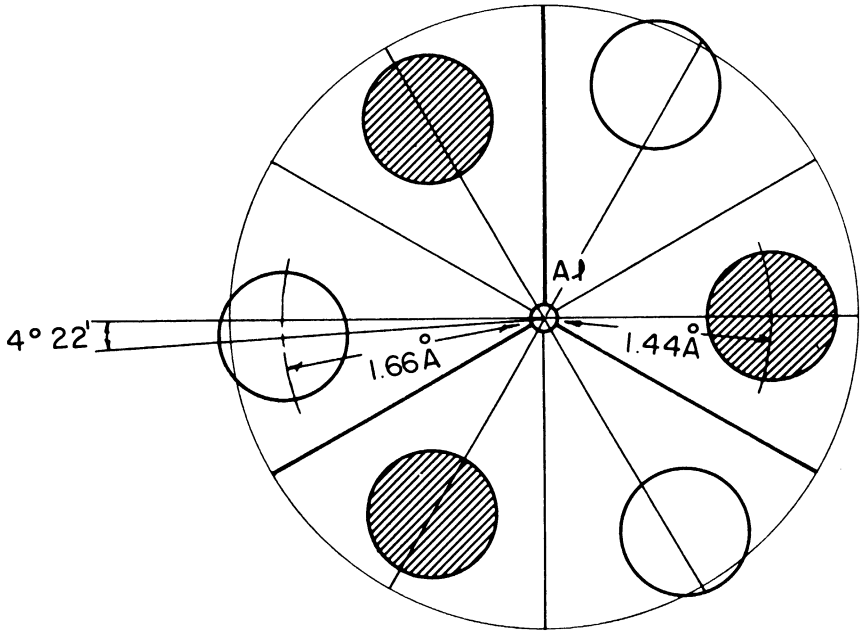

Figure 7. Projection of oxygens in Al_2O_3 onto a plane perpendicular to the trigonal axis.

In the crystalline field calculation the next-nearest-neighbor aluminum ions are accounted for. A list of the 14 next-nearest-neighbors, their distances from the substitutional site, and approximate angles (cosines are exact) with the crystalline c axis are shown in Table I. The oxygens are also included for completeness.

TABLE I

Location of the neighbor and next-nearest-neighbor ions with respect to a substitutional impurity in α-Al_2O_3.[59]

Site	# of ions	Distance Å	cos	approx.
Impurity	1	0.0	-------	----
O1	3	1.84937	0.43575	64°
O2	3	1.98828	-0.68899	133°
Al 1	1	2.73273	-1.00000	180°
Al 2	3	2.80912	-0.20072-	101°
Al 3	3	3.18581	0.50374	60°
Al 4	3	3.50390	0.61893	52°
Al 5	3	3.50390	-0.61893	128°
Al 6	1	4.67959	1.00000	0°

It should be noted for later reference that if one moves along the c axis of the crystal, one adjacent octahedral site will contain an aluminum but the other is empty.

It is the change of position of the surrounding ions with pressure that causes t he crystalline field to change. The displacement of the ions with hydrostatic pressure can be obtained from the following discussion of the elastic constants.

C. THE ELASTIC CONSTANTS FOR SAPPHIRE

For any elastic deformation there is a linear relation between the stresses applied and the resulting strains. These relations are derived in Appendix C and put into the notation for which the values are usually reported in the literature. In the usual matrix notation this relation is expressed

$$p_i = \sum_{j=1}^{6} c_{ij} u_j \tag{19}$$

where the c_{ij} are the elastic "stiffness" coefficients, p_i are the stresses, and u_j the resulting strains. Similarly,

$$u_i = \sum_{j=1}^{6} s_{ij} p_j \tag{20}$$

where the s_{ij} are the elastic "compliance" coefficients. The stresses, p_i, are related to the components of the stress tensor σ_{ij} as follows:

$$\begin{aligned} p_1 &= \sigma_{xx} & p_4 &= \sigma_{yz} = \sigma_{zy} \\ p_2 &= \sigma_{yy} & p_5 &= \sigma_{xz} = \sigma_{zx} \\ p_3 &= \sigma_{zz} & p_6 &= \sigma_{xy} = \sigma_{yx} \end{aligned} \tag{21}$$

The strains, u_i, are related to the components of the strain tensor ϵ_{ij} as follows

$$\begin{aligned} u_1 &= \epsilon_{xx} & u_4 &= \epsilon_{yz} + \epsilon_{zy} \\ u_2 &= \epsilon_{yy} & u_5 &= \epsilon_{xz} + \epsilon_{zx} \\ u_3 &= \epsilon_{zz} & u_6 &= \epsilon_{xy} + \epsilon_{yx} \end{aligned} \tag{22}$$

A component, σ_{ij} , of the stress tensor can be thought of as the tensile force per unit surface area in the i^{th} direction applied to a surface whose normal is in the j^{th} direction. Similarly, a component, ϵ_{ij} , of the strain tensor can be thought of as the elongation per unit length in the i^{th} direction for j = i and the change in the angle between the i^{th} and j^{th} axes for $i \neq j$.

It is shown in Appendix C that the symmetric matrices s_{ij} and c_{ij} generally have 21 independent components and that the crystal symmetry restricts this number further. The most general compliance tensor for the sapphire lattice which has $\bar{3}$ m symmetry has the six independent components shown:

$$\begin{pmatrix} u_1 \\ u_2 \\ u_3 \\ u_4 \\ u_5 \\ u_6 \end{pmatrix} = \begin{pmatrix} S_{11} & S_{12} & S_{13} & S_{14} & 0 & 0 \\ & S_{11} & S_{13} & -S_{14} & 0 & 0 \\ & & S_{33} & 0 & 0 & 0 \\ & & & S_{44} & 0 & 0 \\ & SYM. & & & S_{44} & 2S_{14} \\ & & & & & 2(S_{11}-S_{12}) \end{pmatrix} \begin{pmatrix} P_1 \\ P_2 \\ P_3 \\ P_4 \\ P_5 \\ P_6 \end{pmatrix} \qquad (23)$$

In the case of hydrostatic pressure

$$P_1 = P_2 = P_3 = -P \qquad (24)$$

and

$$P_4 = P_5 = P_6 = 0$$

The compressional analysis done later utilizes the x and z displacements, Δx and Δz, of ions neighboring the impurity

ion. These are then related to the elastic compliance constants by the following:

$$u_1 = \epsilon_{xx} = \frac{\Delta x}{x} = -\left(S_{11} + S_{12} + S_{13}\right) p$$
$$u_3 = \epsilon_{zz} = \frac{\Delta z}{z} = -\left(2 S_{13} + S_{33}\right) p \quad . \tag{25}$$

For uniaxial compression

$$p_1 = -p \; ; \quad p_2 = p_3 = p_4 = p_5 = p_6 = 0 \quad . \tag{26}$$

The displacements are then calculated with the elastic compliance constants:

$$u_1 = -S_{11} p$$
$$u_3 = -S_{13} p \tag{27}$$

Then for both cases the x and z displacements are simply u_1 x and u_3z.

The most recent compilation of elastic constants for sapphire is that of Bernstein[47] who quotes the values

$$\begin{aligned} C_{11} &= 4.92 \times 10^{12} \text{ DYNE/CM.}^2 \\ C_{33} &= 4.92 \quad " \quad " \\ C_{44} &= 1.47 \quad " \quad " \\ C_{12} &= 1.68 \quad " \quad " \\ C_{13} &= 1.16 \quad " \quad " \\ C_{14} &= -0.234 \quad " \quad " \end{aligned} \tag{28}$$

Since the compliance constants are used to determine strain, the reciprocal matrix of these c_{ij} values must be obtained. For a crystal of $\bar{3}$ m symmetry the inversion is simplified to[60]

$$\begin{aligned} S_{11} + S_{12} &= C_{33} / C \\ S_{11} - S_{12} &= C_{44} / C' \\ S_{13} &= - C_{13} / C \\ S_{14} &= - C_{14} / C' \\ S_{33} &= (C_{11} + C_{12}) / C \\ S_{44} &= (C_{11} - C_{12}) / C' \end{aligned} \tag{29}$$

where

$$C = C_{33} (C_{11} + C_{12}) - 2 C_{13}^2$$

$$C' = C_{44} (C_{11} - C_{12}) - 2 C_{14}^2 .$$

This yields the following values

$$\begin{aligned} S_{11} &= 0.241 \times 10^{-12} \text{ (DYNE/CM.}^2\text{)}^{-1} \\ S_{33} &= 0.222 \quad " \quad " \\ S_{44} &= 0.697 \quad " \quad " \\ S_{12} &= -0.0755 \quad " \quad " \\ S_{13} &= -0.0390 \quad " \quad " \\ S_{14} &= -0.0503 \quad " \quad " \end{aligned} \tag{30}$$

These are the compliance constants used in the analysis of this experiment and are summarized with the stiffness constants in Table II.

TABLE II

The Elastic Stiffness Constants, c_{ij}, and Compliance Constants, s_{ij}, for Sapphire at Room Temperature. (c_{ij} from B.T. Bernstein, J. Appl. Phys. 34, 169 (1963); s_{ij} by inversion.)

c_{11} = 4.92 x 10^{12} dyne/cm^2		s_{11} = 0.241 x 10^{-12} cm^2/dyne	
c_{33} = 4.92	"	s_{33} = 0.222	"
c_{44} = 1.47	"	s_{44} = 0.697	"
c_{12} = 1.68	"	s_{12} = -0.0755	"
c_{13} = 1.16	"	s_{13} = -0.0390	"
c_{14} = -0.234	"	s_{14} = -0.0503	

Since these constants are for the bulk crystal and the local compression about the impurity site is of concern, the bulk compressibility must be related to the "local compressibility" about the impurity ion. The usual assumption is that they are equal.[20,22] This implies that the neighboring ions will compress about the impurity ion as if they were all imbedded in a medium with the bulk elastic properties of sapphire. There will be "local relaxation" if the compliance constants of this hypothetical medium are larger than for sapphire and "local tension" if they are smaller, i.e., local relaxation implies that the neighboring ions displace more than expected for a given stress.

Local relaxation could be expected if the atomic forces between the impurity ion and the ligands were less than for an original lattice ion. For example, this would be the case on a purely ionic b asis for a substitutional atom with a lower valence state. Since covalency effectively reduces ionic charge, it would be expected to lead to local relaxation also, but to what extent the covalent bonding strengthens the interatomic force to compensate for this is unknown. An estimate of the combined effects can be obtained from bulk compressibilities. Kittel[61] has shown that the bulk compressibility is generally inversely proportional to the interatomic force. In general, highly covalent structures such as diamond ($\beta = \frac{10^6}{V^0}\frac{\Delta V}{\Delta P}\,\text{ATM.}^{-1} = 0.16$) silicon (0.32), SnO_2 (0.49), and germanium (1.42) have lower bulk compressibilities than highly ionic structures such as AgBr (2.74), NaCl (4.18), KCL (5.65), and RbBr (7.97). This implies that a higher degree of covalency for the impurity ion than the normal lattice ion could lead to local tension. Local tension would also result if polarization effects are significant since added distortion is necessary with compression.

Now it is necessary to determine the crystalline field at the impurity ion site and predict the changes due t o the above displacements. This is done in the next two sections.

D. THE CRYSTALLINE FIELD MODEL

The crystal field model will be used in which the crystalline field is determined by a calculation of the potential at the impurity ion site when approximating the surrounding ions as appropriate point charges at the ionic lattice sites. In view of the criticism of the crystal field model[62] and the failure of the simple theory to satisfactorily predict the zero-field splitting of the $^4A_2$ ground term of the Cr^{3+} ion in ruby,[40] the use of this model must be justified. First, a more recent expansion of the crystal field analysis to include distortion of the wave functions by the trigonal field through configuration mixing and the covalent π bonds has shown good agreement.[63] Also, the crystal field calculations to fit optical spectra show reasonable agreement when some displacement of the impurity ion is assumed.[42] This assumption is supported by ENDOR (Electron Nuclear DOuble Resonance) experiments.[39] Thus a model that can reasonably predict the splitting should be able to predict changes much more accurately. Finally, the point charge model has worked before for trigonal calcite.[22] With these justifications the crystal field model is used with the idea that the results will give some indication of its validity.

If it is assumed that the impurity ion is surrounded by point charges and that the impurity ion charge does

not overlap those of the surrounding ligands, then Laplace's equation holds

$$\nabla^2 V = 0 \tag{31}$$

and the crystalline field potential due to the point charges can be expanded about the impurity ion site. In this region Laplace's equation has general solutions of the form

$$V(\underline{r}) = \sum_{l,m} a_{lm} r^l Y_{lm}(\theta, \phi) \tag{32}$$

where r, θ, and ϕ are the spherical coordinates of $\underline{r}$ centered at the impurity site. Equating this to the potential

$$V(\underline{r}) = \frac{1}{4\pi\epsilon} \sum_i \frac{q_i}{|\underline{r} - \underline{r}_i|} \tag{33}$$

at the position $\underline{r}$, due to the sum of the charges q_i at the surrounding ion sites $\underline{r}_i$ at the coordinates (r_i, θ_i, ϕ_i), results in the coefficients

$$a_{lm} = \frac{1}{\epsilon(2l+1)} \sum_i \frac{q_i}{r_i^{l+1}} Y_{lm}^*(\theta_i, \phi_i) \quad . \tag{34}$$

(The details of this and the following analysis are carried out in Appendix A.) The C_3 symmetry of the crystal lattice restricts the m values to integral multiples of three and l values to even integers. The use of 3d wave functions for which $l = 2$ cuts the series at $l = 4$ and

allows only even values of ℓ. The a_{oo} term is just a constant and since Cr^{3+} and V^{2+} both have S = 3/2, only the term in a_{20} remains. This coefficient becomes, where the spherical harmonic is put in terms of Legendre polynomials,

$$a_{20} = \epsilon \frac{1}{\sqrt{20\pi}} \sum_i q_i P_{20}(\cos\theta_i) r_i^{-3} \tag{35}$$

In the next section D is shown to be proportional to a_{20} and the change in a_{20} with lattice compression is also derived. Calculations of a_{20} are included in Appendix A and a summary of the results in Table III are also in the next section.

E. COMPRESSIONAL MODEL AND PREDICTED BEHAVIOR

In order to evaluate the results of this experiment with respect to the crystalline field model, some model of change of the crystal lattice with hydrostatic compression must be assumed. This, then, must be related to the changes in the crystalline field spin Hamiltonian parameters.

Assumptions. The following assumptions are made and discussed in turn:

1. The local compressibility is the same as the lattice compressibility.

This implies that the surrounding ions will compress about the impurity ion site in the manner as if they were imbedded in a material with the same elastic constants as bulk sapphire. Local relaxation, or greater compressibility, about the impurity ion site was deduced in several other materials. There has been some evidence of local relaxation in MgO[34] and $SrTiO_3$[23], but Drickamer[36] has shown that none exists for Cr^{3+} or V^{3+} in sapphire. This is probably due to its stiffness.

2. The impurity ions are substitutional.

This assumption is under serious question both from optical studies[42] and ENDOR results.[39] It is also suspected that the vanadium and the chromium do not occupy the same site. It is one of the objectives of this study to check on this assumption.

3. The changes in the spin Hamiltonian parameters are due primarily to changes in the intensity of the electrostatic crystalline field.

The spin Hamiltonian parameters could also be affected by changes in covalency (or the degree to which ligand orbitals must be used in determining wave functions) and changes in the distribution of the 3d wave functions as shown later in this section. A direct measure of both of these parameters is the Racah B parameter.[55,64] It is shown in Appendix F that both an increase in the degree of

covalency and an expansion of the radial distribution of the wave functions, which would be expected with increasing pressure, will tend to decrease B. Drickamer's optical experiment[36] shows that the change in the Racah B parameter is very small in our pressure ranges. The decrease in B observed in ruby is 0.03% as compared to observed shifts in the crystalline field parameter of about 0.2%. Therefore this assumption seems reasonable.

4. The point charge model can be used to describe the changes in the electrostatic field.

For a crystalline field which is cubic and in which the compression has the effect of simply shrinking the distance to the surrounding ions, this assumption is exact. For this reason the point charge model was used in the work by Walsh[20] and Wait.[22] Even for a distributed ligand charge this assumption is valid of the compression is "conformal" or angle preserving and the charge distribution lies outside the ion. This is shown in Appendix A. One of the reasons for choosing such a model for ruby, which has trigonal symmetry and nonconformal compression, is that it was used with success for trigonal symmetry before,[22] even though the calcite compression was also far from conformal. Also, the agreement that Drickamer[36] obtains with a simple point charge analysis supports this assumption. However, one of the motivations in choosing the sapphire structure was to check this agreement and that for calcite.

Change in the Coefficient a_{20}. The method used will be to determine the rate of change of a_{20} with change in the position of a surrounding ion and simply multiply by the change in position per unit pressure as predicted by the elastic constants and the first assumption.

As is easily seen from Figure 6, by taking the z axis as the axis of trigonal symmetry, the contributions to the crystalline field on the axis from each of the three oxygens in a plane are equal and any dependence on ϕ can be neglected. It is easiest now to consider only one of the oxygens, namely the one lying on the positive axis. The effect of this ion will then be one third of the effect of all three for any symmetry preserving motion of the one. Thus, if one were considering only the effect of the oxygens, the sum in equation 35 would be over the two values i;

i	r_i	θ_i
1	1.84 Å	64° 10′
2	1.98 Å	46° 27′

(36)

where r_i and θ_i are obtained from Table I and then

$$a_{20} = 3 Q q_{oxy.} \sum_{i=1}^{2} \frac{P_{20}(\cos \theta_i)}{r_i^3} \qquad (37)$$

where Q is just a combination of constants, and $q_{oxy.}$ is the charge on an oxygen ion. A similar condensation can be performed for the fourteen nearest neighbor aluminums when the sites listed in Table I contain more than one ion.

To get the change in a_{20} with pressure it is easier to transform to a rectangular coordinate system with the same z axis but with the x axis through an oxygen site. Then we can determine a change in a_{20} as

$$\frac{\Delta a_{20}}{a_{20}} = \frac{1}{a_{20}} \sum_i \left\{ \frac{\partial a_{20}}{\partial x} \Delta x_i + \frac{\partial a_{20}}{\partial z} \Delta z_i \right\} . \quad (38)$$

The Δx_i and Δz_i are obtained from the elastic constants (See Section C) and are respectively $u_1 x_i$ and $u_3 z_i$. In this coordinate system there is no need to consider Δy_i since y_i for the ion is zero. Thus the compression is symmetry conserving, allowing the condensation above.

The rate of change of a_{20} with position can be obtained from equation 35. For $x_k = x,z$ one obtains

$$\frac{\partial a_{20}}{\partial x_k} = Q \sum_i q_i \left[\frac{-3}{r_i^4} \frac{\partial r_i}{\partial x_k} P_{20}(\cos\theta_i) + \frac{1}{r_i^3} \frac{\partial P_{20}(\cos\theta_i)}{\partial x_k} \right] . \quad (39)$$

Since $r_i = (x_i^2 + y_i^2 + z_i^2)^{\frac{1}{2}}$ the following relations hold:

$$\frac{\partial r_i}{\partial x} = \frac{\partial r_i}{\partial x_i} = \frac{x_i}{r_i} = \sin\theta_i$$

$$\frac{\partial r_i}{\partial z} = \frac{\partial r_i}{\partial z_i} = \frac{z_i}{r_i} = \cos\theta_i .$$

One now obtains by substitution into equation 38

$$\frac{\Delta a_{20}}{a_{20}} = \frac{Q}{a_{20}} \sum_i q_i \left[u_1 x_i \left(\frac{-3}{r_i^4} \sin\theta_i P_{20} + \frac{1}{r_i^3} \frac{\partial P_{20}}{\partial x} \right) + u_3 z_i \left(\frac{-3}{r_i^4} \cos\theta_i P_{20} + \frac{1}{r_i^3} \frac{\partial P_{20}}{\partial z} \right) \right] \quad (40)$$

where

$$\frac{\partial P_{20}}{\partial x_k} = \frac{\partial \frac{1}{2}(3\cos^2\theta_i - 1)}{\partial x_k} = 3\cos\theta_i \frac{\partial \cos\theta_i}{\partial x_k}$$

and

$$\frac{\partial \cos\theta_i}{\partial x} = \frac{\partial}{\partial x_i}\left(\frac{z_i}{r_i}\right) = \frac{-\sin\theta_i \cos\theta_i}{r_i}$$

$$\frac{\partial \cos\theta_i}{\partial z} = \frac{\partial}{\partial z_i}\left(\frac{z_i}{r_i}\right) = \frac{\sin^2\theta_i}{r_i} \quad .$$

The substitution of the structure constants for the six oxygens and fourteen nearest neighbor aluminums from Table I and the elastic constants from Table II is shown in Appendix B. Since there was suspicion that the impurity ion was not substitutional but displaced along the trigonal z axis by about 0.1 Å toward the empty octahedral site (i.e. toward the top of Figure 6), these calculations were performed at various positions in this direction. One calculation was done in the opposite direction as a check. A summary of the values obtained are shown in Table III. The contribution of the fourteen nearest neighbor aluminums is relatively small and is therefore sometimes neglected. It is interesting to note that this contribution becomes negligible at a position 0.15 Å towards the empty octahedral site. If one plots the relative positions of the surrounding ions from Table I as shown in Figure 8, it can be seen that this is about where the aluminum contribution is symmetric.

TABLE III

Summary of the Theoretical Calculations of the Change with Pressure in the Crystalline Field Parameter as a Function of Displacement Along the Trigonal Axis in Al_2O_3. (a_{20} is in units of Q x 10^{-2} $Å^{-3}$ where $Q = 1/e\sqrt{20\pi}$ and $\Delta a_{20}/a_{20}$ is in units of 10^{-3}/katm. Positive displacement is towards the empty octahedral site.)

PARAMETER	CALCULATION INCLUDES	DISPLACEMENT −0.1 Å	SUBST.	+0.1 Å	+0.12 Å	+0.15 Å
a_{20}	6 Ox.	0.796	4.33	10.25	10.80	12.55
	6 Ox. + 14 Al.	—	6.68	11.55	—	13.37
$\left(\frac{\Delta a_{20}}{a_{20}}\right)_{\text{HYDROSTATIC}}$	6 Ox.	2.56	0.740	0.522	0.501	0.478
	6 Ox. + 14 Al.	—	0.643	0.508	—	0.478
$\left(\frac{\Delta a_{20}}{a_{20}}\right)_{\text{UNIAXIAL}}$	6 Ox.	32.9	5.39	1.96	1.67	1.30
	6 Ox. + 14 Al.	—	3.86	1.76	—	1.29

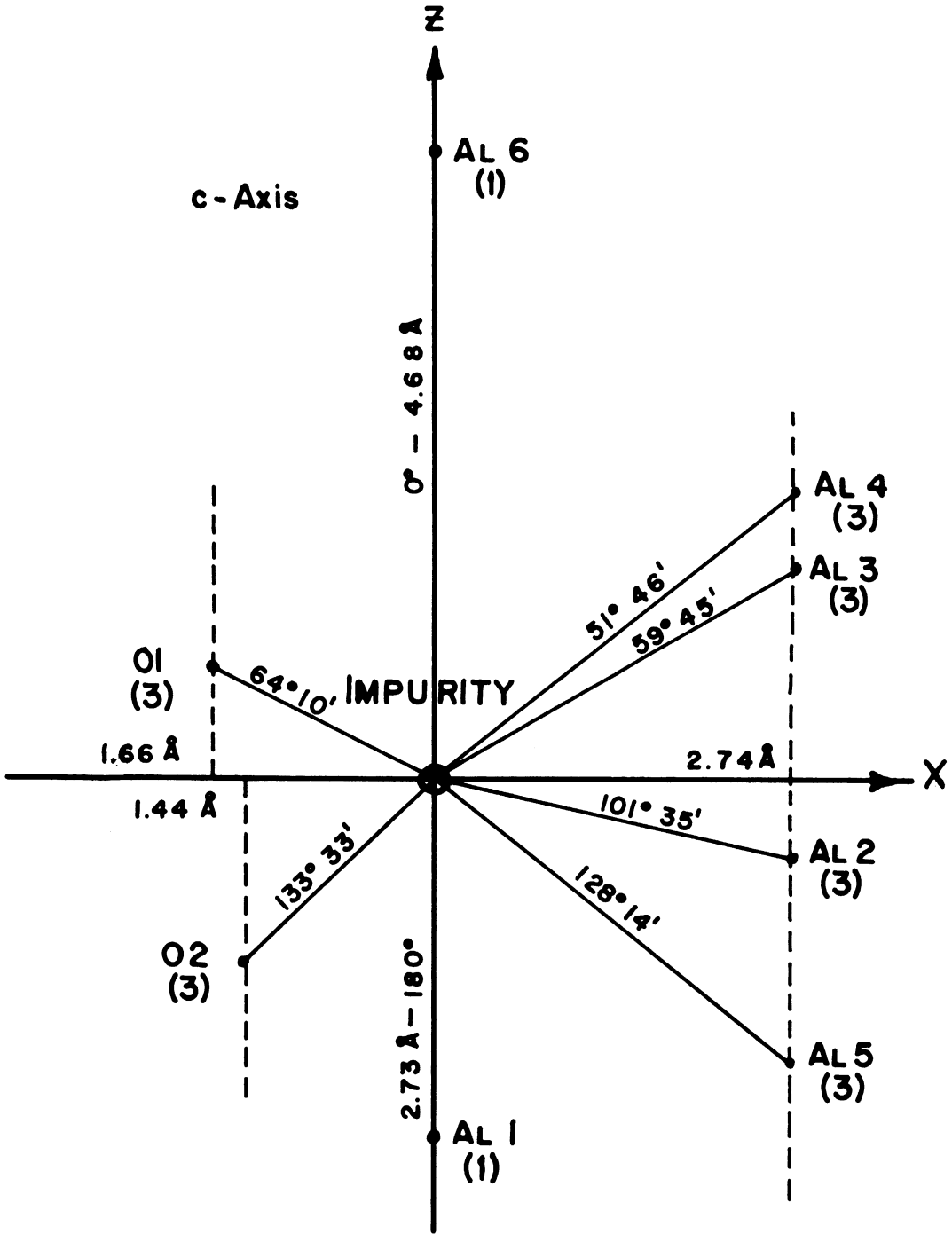

Figure 8. Relative positions of the nearest and next-nearest-neighbor ions in sapphire.

Predicted Behavior. Before predicting the pressure dependence of the zero field splitting due to changes in the crystalline field, the dependence of the splitting on the crystalline field must be determined. With the restriction to only the a_{20} term, equation 30 becomes

$$V_{AX} = a_{20} r^2 Y_{20} = a_{20} \left(3z^2 - r^2 \right) \quad . \qquad (41)$$

Substitution of orbital angular momentum operators according to Stevens[46] yields

$$V_{AX} = \frac{2}{105} a_{20} \langle r^2 \rangle \left[3 L_z^2 - L(L+1) \right] \equiv 2\delta \left[L_z^2 - \tfrac{1}{3} L(L+1) \right] \qquad (42)$$

where δ is the axial field splitting and the integral is already performed on r^2. As shown in Appendix G, V_{ax} splits the excited states $^4T_2$ and $^4T_1$ but not the $^4A_2$ ground state. The matrix elements are evaluated in Appendix G and result in the splittings of 15 δ (or 3/2 K) shown in Figure 9. Since there is no splitting of the ground state due only to the axial field, the observed splitting arises through second order spin-orbit coupling to the higher states.

Evaluation of the matrix elements of the second order perturbation λ L·S, as the third term in equation 5, to the axial split excited states in Figure 9 becomes

$$\Delta E = -\sum_{n=1}^{4} \frac{\lambda^2 \langle 0 | L \cdot S | n \rangle \langle n | L \cdot S | 0 \rangle}{E_n - E_0} \qquad (43)$$

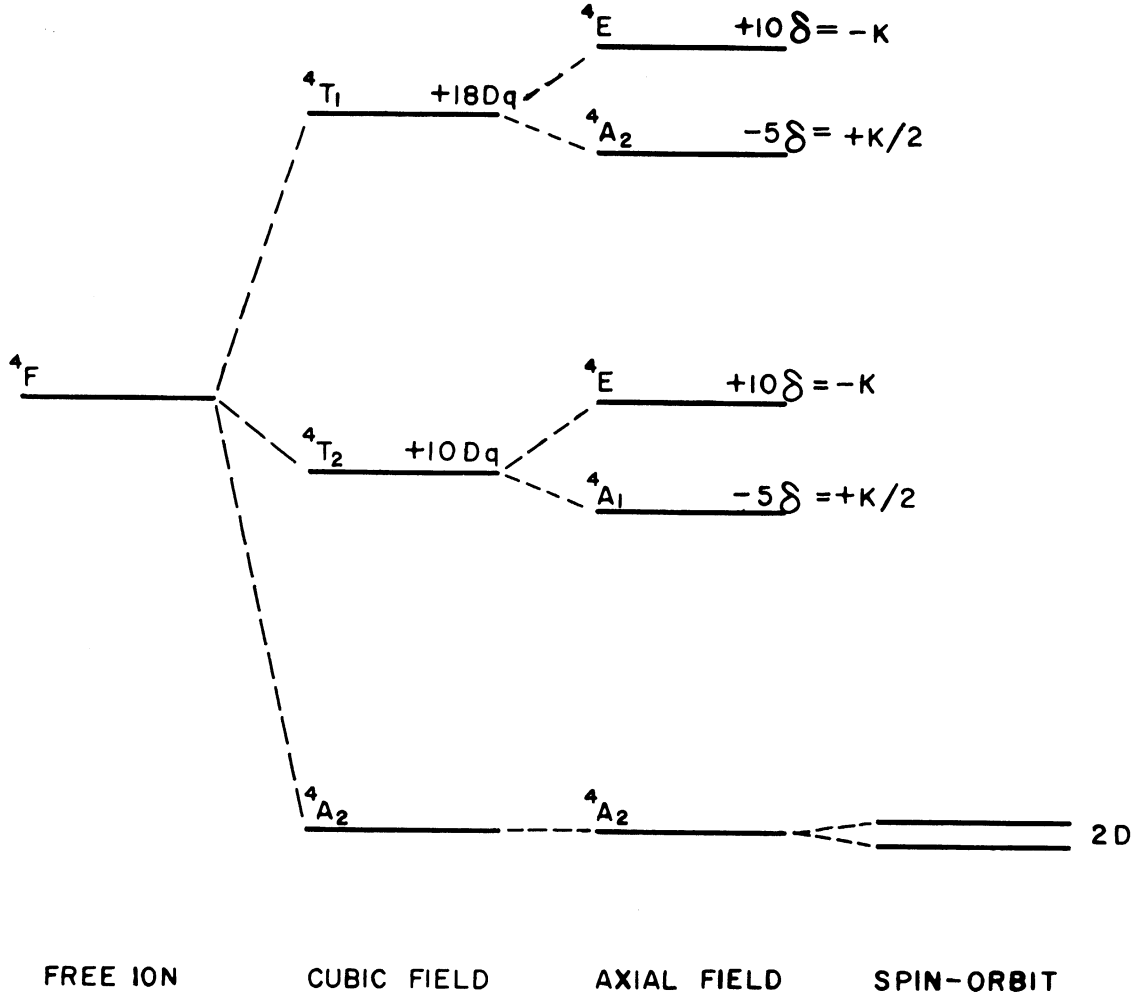

Figure 9. Crystalline field splitting of ^4F ground state for a $3d^3$ ion.

where the sum is over the axial split excited states and o refers to the unsplit $^4A_2$ ground state. Since L transforms as the irreducible representation T_1 of O_h and the product resulting from the $^4T_1$ excited state matrix elements, $T_1 \times T_1 \times A_2$ (see product table Appendix F), does not contain the identity representation, its matrix elements are zero and only those of the $^4T_2$ state are considered. These matrix elements are calculated in Appendix G and the result is

$$\Delta E = -\lambda^2\left[\frac{4S_z^2}{10Dq+10\delta} + \frac{4(S_x^2+S_y^2)}{10Dq-5\delta}\right] \tag{44}$$

where the excited states due to the excited doublet $^2T_2$ with its larger energy denominators have been neglected. The other excited doublet states do not couple directly with the ground state as in the case of the $^4T_1$ state.

Since δ is much smaller than Dq, equation 44 can be approximated as

$$\Delta E \cong \frac{-4\lambda^2}{10Dq}\left[S_z^2\left(1-\frac{\delta}{Dq}\right)+\left(S_x^2+S_y^2\right)\left(1+\frac{\delta}{2Dq}\right)\right] \tag{45}$$

or

$$\Delta E \cong \frac{-4\lambda^2}{10Dq}\left[S_x^2+S_y^2+S_z^2+\frac{\delta}{2Dq}\left(S_x^2+S_y^2-2S_z^2\right)\right] \tag{46}$$

or since $S_x^2 + S_y^2 + S_z^2 = S(S+1)$

$$\Delta E \cong \frac{-4\lambda^2}{10Dq}\left[S(S+1) - \frac{\delta}{2Dq}\left\{3S_z^2 - S(S+1)\right\}\right] . \tag{47}$$

The first term is simply the isotropic part and adds a constant to all levels. The coefficient of the term $3S_z^2 - S(S+1)$, or D, is

$$D = \frac{\delta\lambda^2}{5(Dq)^2} \tag{48}$$

where δ contains the a_{20} of the previous section. Thus, for small changes, the relative change in D is

$$\frac{\Delta D}{D} \cong \frac{\Delta\delta}{\delta} + \frac{2\Delta\lambda}{\lambda} - \frac{2\Delta Dq}{Dq} . \tag{49}$$

Similarly, the spin orbit coupling will shift the g value from the free ion value, g_o, and an equation analogous to equation 48 is (see Appendix G)

$$(g - g_o)_z = \frac{-8\lambda}{10Dq + 10\delta} . \tag{50}$$

For small changes then

$$\frac{\Delta(g-g_o)_z}{(g-g_o)_z} \cong \frac{\Delta\lambda}{\lambda} - \frac{\Delta Dq}{Dq} . \tag{51}$$

These equations (49 and 51) can then be used to predict the shifts in the spin Hamiltonian parameters D and $(g-g_o)$ if pressure data is available for the changes in Dq and λ. Only the change in Dq with uniaxial pressure is known from Drickamer's work.[36] Further analysis from the available data and the data from this experiment will be performed in Chapter V.

Chapter III

EXPERIMENT

For this experiment an electron paramagnetic resonance spectrometer for studying crystals under high hydrostatic pressure has been constructed[65] having many distinct advantages over earlier such instruments.[66,67,35] The advantages are the ease of cavity coupling adjustment under pressure, the use of a two sample comparison, and the resulting simplicity of data analysis. Also, the pressure is hydrostatic and a precise pressure measurement is possible.

In Section A the crystals and crystal orientation are discussed, in Section B the principles of operation and the construction of the apparatus are described, in Section C the advantages of the two sample system and the solution of the "cross talk" problem are discussed, and in Section D the method of taking data is included.

A. CRYSTALS AND CRYSTAL ORIENTATION

The crystals used in this experiment were identical pairs of washer-shaped single crystals of Al_2O_3+0.1% Cr_2O_3 and Al_2O_3+0.1%V_2O_3 obtained from Linde Optical Company. The crystalline c axis was in the plane of the washer $\pm$ 2.0°. Their dimensions were

I.D.	.090"	.005"
O.D.	.240"	.005"
Thickness	.060"	.005"

The naturally occurring chromium has a 9.5% abundance of the Cr^{53} isotope whose nuclear spin is 3/2, but all other isotopes in natural chromium have a nuclear spin of zero. The chromium substitutes for the aluminum in a plus three valence state. The $Al_2O_3:Cr^{3+}$ crystals were used as obtained from Linde and gave clear strong signals.

Naturally occurring vanadium is primarily the V^{51} isotope whose nuclear spin is 7/2. The vanadium also substitutes for the aluminum in the plus three state with a very small amount occurring in the plus four state. The plus three state is not discernible with microwave spectroscopy at room temperature and the plus four state does not interfere with the observed plus two spectra.[38] To obtain the doubly ionized vanadium, the crystals were subjected to 50 kev. X-rays for a period of three hours.[38] Because the conversion efficiency to V^{2+} is small and the signal strength is spread over eight lines (I = 7/2) instead of one as in ruby, the signal strengths were considerably weaker.

The crystals were oriented spectroscopically. As will be seen in the next sections, the cylindrical axis of the washer shaped crystals is coincident with the axis of rotation of the magnet. The plane of the washers is thus

perpendicular to this axis and held in the plane of rotation by the sample holders to much better than the $\pm 2^{\circ}$ quoted by the crystal manufacturer. No further attempt was made to orient the c axis in this plane.

Using Figure 4, which is a plot of the resonant magnetic field values as a function of angle, two points were used to orient the crystalline c axis of the ruby crystals with respect to the magnetic field. At $\vartheta = 54.74^{\circ}$ two levels cross and can be observed by the recordings to $\pm 0.5^{\circ}$. This was used as a check. Principally, the crystals were oriented by using the maximum for the high field line at $\vartheta = 0^{\circ}$. Observing the maximum of the resonances on the oscilloscope while rotating the magnet allowed orientation to the readability of the magnet scale or $\pm 0.2^{\circ}$. The vanadium crystals were oriented by observing the disappearance of the forbidden transitions which occur between the eight high field hyperfine lines when the c axis and the magnetic field are not exactly coincident.[43] This allowed orientation by observing the spectra to about $\pm 0.5^{\circ}$ and there was no indication that the alignment in the plane of the washer was significantly worse than this.

B. THE EXPERIMENTAL APPARATUS

The principles of operation are as follows: The two samples are placed in the atmospheric and high pressure sections of the microwave resonant cavity (Figure 11), which is located in a DC magnetic field. The magnetic field about each sample is modulated at a different frequency. The microwave power absorbed by the cavity is then fed as signal to two phase sensitive detection systems, each of which is sensitive to one of the two modulation frequencies. The signals from both samples are thus separated and plotted out on a pair of identically driven recorders. Thus the percentage change can be directly determined, and with a calibrated field sweep the relative shift can be directly measured in gauss. This not only reduces the error (formerly the difference between two large numbers) but greatly simplifies the analysis and procedure by reducing the need for considering second order corrections, hysteresis effects, and ambient changes.

The high pressure is generated by a hand pump, magnified with a piston intensifier (Figure 12), and fed to a beryllium-copper bomb through thick walled stainless steel tubing.

Spectrometer. The spectrometer is of the homodyne type[68] and utilizes X band (8-12 kMc/sec.) frequencies and phase sensitive detectors. Reflected power from the cavity

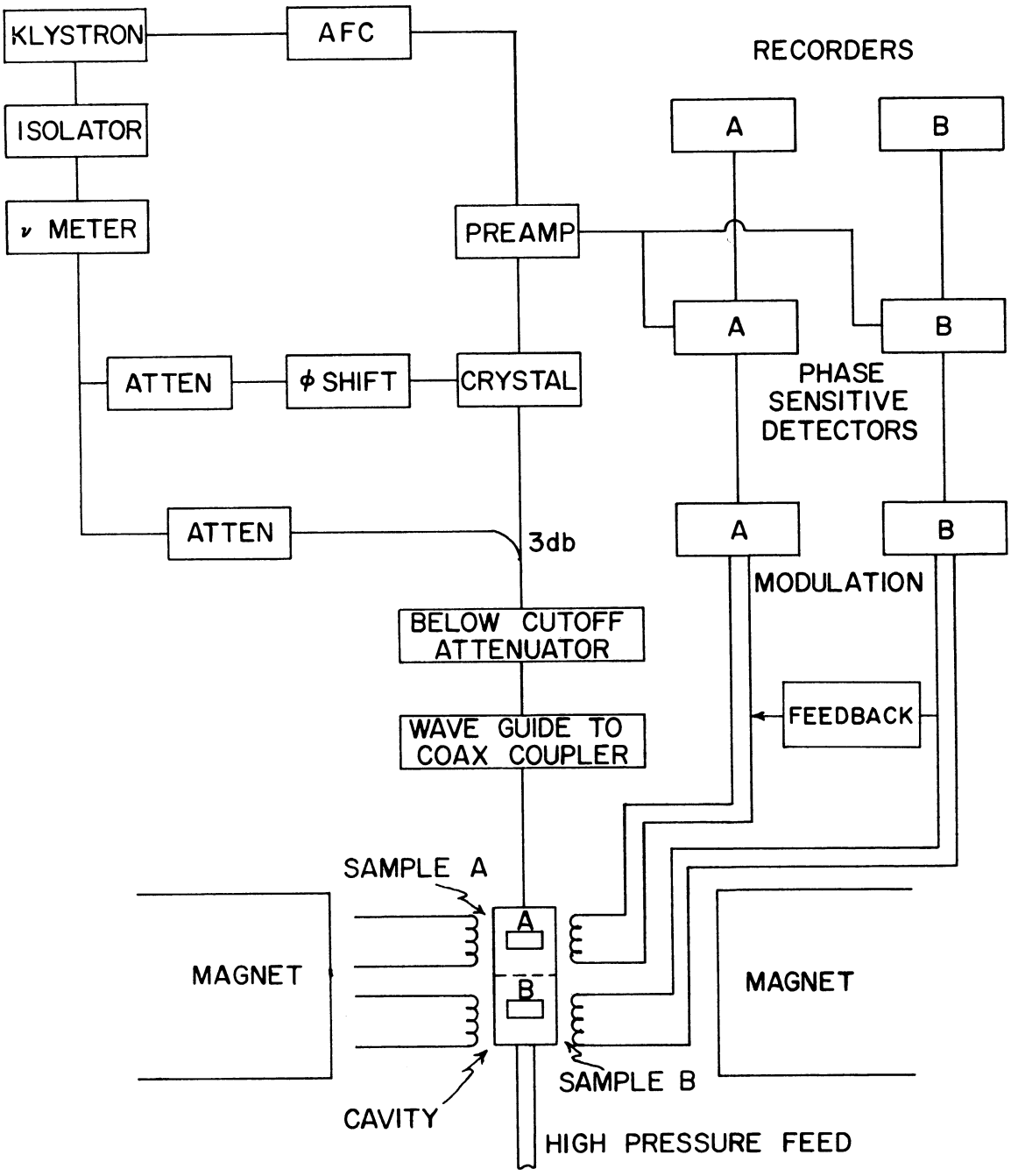

Figure 10. Spectrometer schematic.

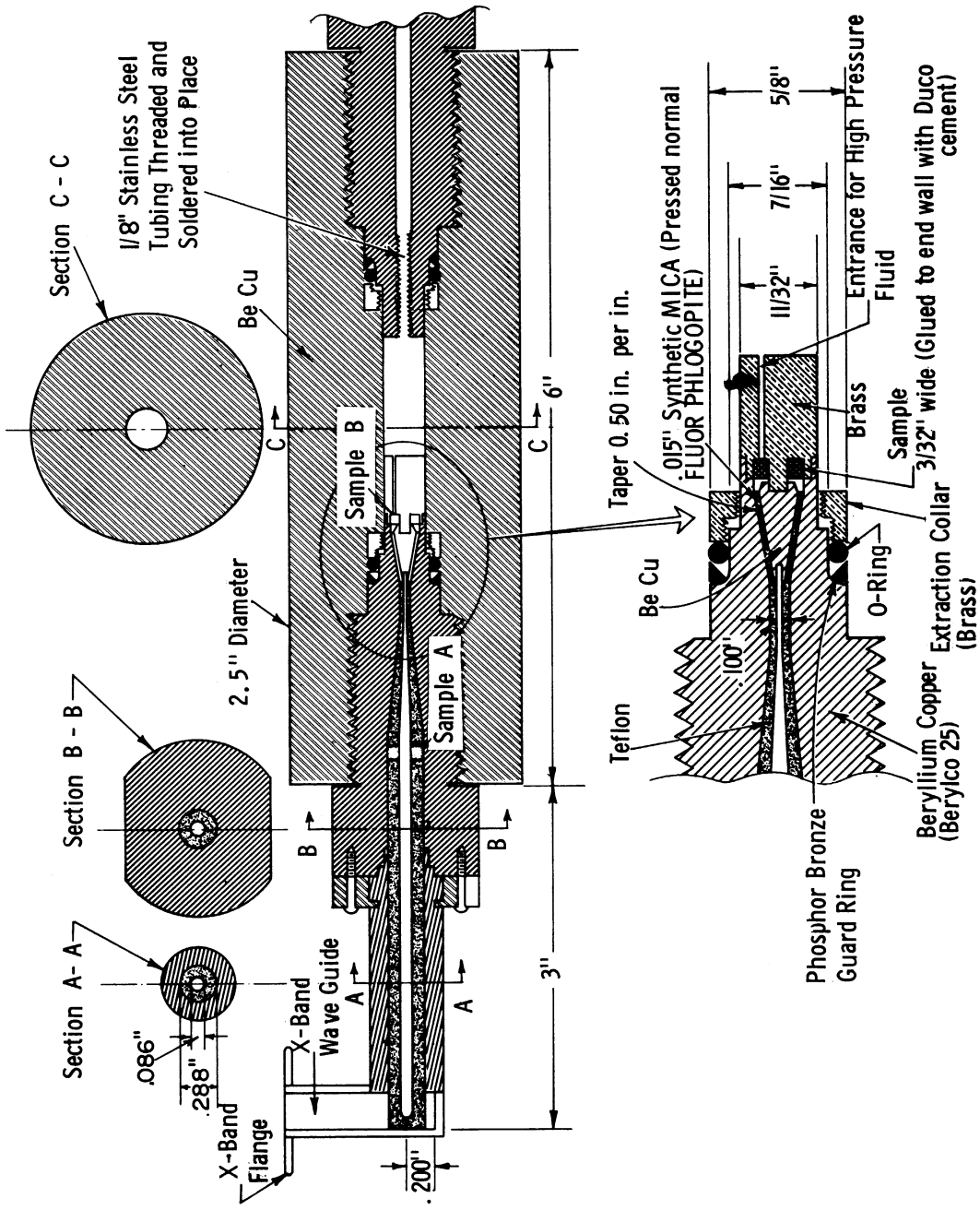

Figure 11. Pressure bomb and microwave cavity.

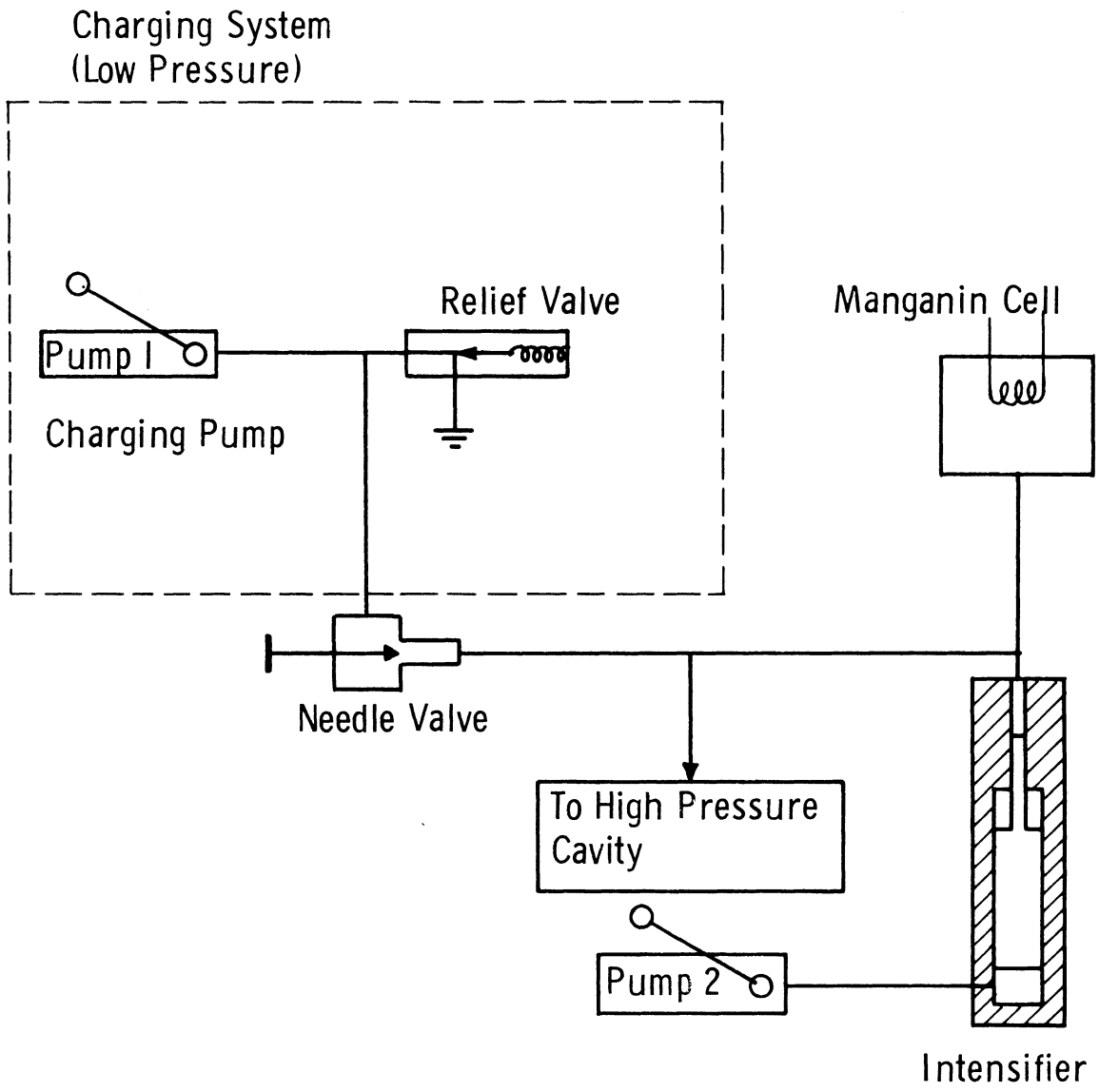

Figure 12. High pressure system schematic.

is used for detection[68] at present, however, and the bypass arm in the microwave system has been built in for future use. Referring to Figure 10, the microwaves are generated by the klystron and coupled through the electric field into the co-axial (Figure 11) cavity with the coupling adjusted by a below cutoff attenuator. The reflected power is then detected by a crystal detector. The microwave frequency is locked to the cavity by an automatic frequency control which uses a 10 kc frequency modulation and signal feedback.

The cavity is coaxial and built into one of the plugs of the high pressure bomb as shown in Figure 11. The cavity entrance is at the wave guide to coaxial converter and about 8 wavelengths from the high pressure sample. Just the last portion of the cavity, shown in detail in Figure 11, is at high pressure; this not only allows the coupling to be changed readily with pressure but keeps the volume and consequently the stored energy and the cavity's resonant frequency change with pressure at a minimum. This portion is sealed from the atmospheric portion by a beryllium-copper cone which is seated on an insulating cone of synthetic mica (pressed normal fluor phlogopite). The sealing cone is part of the center conductor of the coaxial cavity.

The high pressure sample is located at the end of the cavity. It is usually in the shape of an annulus about the center conductor and surrounded by pentane, the high pressure fluid. The identically oriented low pressure sample is placed part way up the cavity, and the rest of the cavity is filled with teflon.

The location of the second sample was determined by three requirements. First, it had to be beyond the cone and yet in a comparable magnetic field. The fields do not have to be exactly identical since it is the change in one absorption line with respect to the other that is measured. The magnetic field homogeneity was increased tenfold with the addition of simple ring shims which yielded a 3" diameter region in which the field was constant to within 0.1 gauss. (A 9" diameter Varian rotable magnet with a 3.25" gap is used). Second, the modulation of the magnetic field at one sample due to the modulation of the other had to be at a minimum. This was accomplished by placing each sample in the null of the modulating field of the other modulation coil. Third, the sample had to lie near a maximum of the microwave field. These requirements fixed the separation at 1.87". The frequency dependence of the cavity with pressure is small (ca. 2.5 Mc/sec. per 1000 atm). If one uses a thicker and shorter mica cone than indicated in Figure 11,

filling the rest of the space with Teflon, the cavity "Q" is about 500. The Teflon is primarily used to hold the long center conductor motionless to prevent modulation pick-up. Teflon, however, has a broad resonance about g = 2 and for sensitivity in this region a system of washers can be used.

The absorption signal is fed into a preamplifier and then to two phase sensitive detectors whose first stages are twin-tee filter amplifiers adjusted to the two modulation frequencies, 228 cps and 800 cps. (The modulation frequencies have to be low in order to penetrate the bomb.) These are followed by the lock-in amplifiers. The outputs are then plotted by two identical recorders with synchronized charts driven by the same chart drive shaft.

High Pressure System. The components of the high pressure system are shown schematically in Figure 12. Most of the components were manufactured by Harwood Engineering. The system has a low pressure charging section and high pressure generating equipment. Hand pumps are used with a 20:1.5 piston intensifier used to obtain the high pressure. The pressure is determined with a manganin cell and bridge circuit using a precision four decade resistance box and galvanometer. The sensitivity of the measurement circuit has been determined to be less than 1 atmos-

phere. The accuracy is thus limited by the pressure dependence of the resistance of the magnanin wire, which is linear with pressure to within 0.5%. The measuring system was calibrated by observing the 3% volume change as mercury freezes at 7420 atmospheres and 0°C. This was done using a specially constructed Invaro oil hardening steel bomb with a much larger volume than the experimental bomb.

The high pressure is transferred to the bomb through thick walled, cold worked stainless steel tubing with a 0.0075" inside diameter and 0.125" outside diameter. The bomb, shown in Figure 11, is 2.5" O.D. and 11/32" I.D. and open on both ends. The bomb, the two end plugs, and the sealing cone are made of Beryl co 25, a nonmagnetic, high strength beryllium copper alloy which is machined in the annealed state and heat treated afterwards. The plugs are sealed with rubber, teflon, and phosphor bronze ring seals of the unsupported type[69] and the unit is designed to hold a pressure of 10,000 atmospheres. Because of the seals a practical limit is about 8,000 atmospheres. Normal pentane is used as the transfer fluid and at these high pressures it becomes viscous. As much as 15 minutes is necessary for the pressure to be transmitted through the tubing.

The bomb is clamped into the magnet by means of brass clamps attached to circular brass caps which are

clamped over the magnet's pole pieces. These brass caps also hold the ring shims and the modulation coils. The clamps permit motion only in the vertical direction along the two-sample axis, which is also the axis of magnet rotation. This allows precise centering and accurate repositioning.

C. THE TWO SAMPLE METHOD

Perhaps the most practical advantage of comparing the spectra of a sample under high pressure to one at atmospheric pressure is that during the course of the experiment one can see at a glance that a pressure shift in the spectra is indeed there, estimate its order of magnitude, and determine its direction without any calculations or analysis whatsoever. The fact that the two channels are similar reduces the need to consider electronic distortion of the line shape. It also eliminates any consideration of ambient changes since the difference is always what is measured. Hysteresis effects in the magnet, except for homogeneity, can also be ignored unless a set of lines is being considered.

Placing both samples in the same cavity so that the transitions in each occur at the same microwave frequency provides many advantages. Second order frequency corrections in unshifted parameters are completely eliminated.

Also if the pressure perturbations are small, and they usually are, most second order perturbations can be neglected since these would be second order corrections to a pressure shift which is already second order. The fact that both samples are at the same frequency allows some very helpful simplifications in the analysis. For example, consider the spin $-\frac{1}{2}$ to $\frac{1}{2}$ transition for Cr^{3+} in Al_2O_3 with the magnetic field along the c axis of the crystal, from equation 14 with I = 0,

$$h\nu = g_z \beta H = g_z' \beta H' \tag{52}$$

where the primes indicate under pressure. Solving for $\Delta g_z = g_z' - g_z$ is simplified by the equality above to

$$\Delta g_z = g_z \frac{H - H'}{H'} = -g_z \frac{\Delta H}{H'} \tag{53}$$

Thus, a precise measurement of a g shift involves only an ordinary field measurement and no frequency measurement. In a similar manner the $\frac{1}{2}$ to 3/2 transition

$$h\nu = g_z \beta H + 2D = g_z' \beta (H + \Delta H) + 2(D + \Delta D) \tag{54}$$

simplifies to (since g shifts are very small)

$$2\Delta D = -g_z \beta \Delta H \tag{55}$$

Also, if there is a close set of lines that falls within the sweep range so that the unshifted spectra can be used to calibrate the shifted spectra (See Section D), no field measurements whatsoever are needed. In this case, however, linearity of the field sweep to first order is necessary.

The only disadvantage of the two sample method and the major problem of any two signal system is the channel separation or "cross talk". In our case, this is electronically quite simple and narrow band amplifiers and phase sensitive detectors assure that signals carried on each of the two modulation frequencies are definitely separated. To be certain that the signal carried on one of the modulation frequencies is purely due to one sample is not as simple.

If one defines a measure of cross talk, K_A, as the ratio of the signal from sample A that is carried through on channel A to the signal from sample B that is carried through on channel A, then K_A and K_B can be measured experimentally by using two different samples. A lower limit must then be set for K. The center of the absorption line, which is what is measured in this experiment, will be shifted most by a second signal when the second signal is $\frac{1}{2}$ line width away, as shown in Figure 13, so that its maximum slope occurs at the true center. The observed center of the sum (or difference, depending on polarity) of the two signals will then be shifted by 1/4K times the line width.

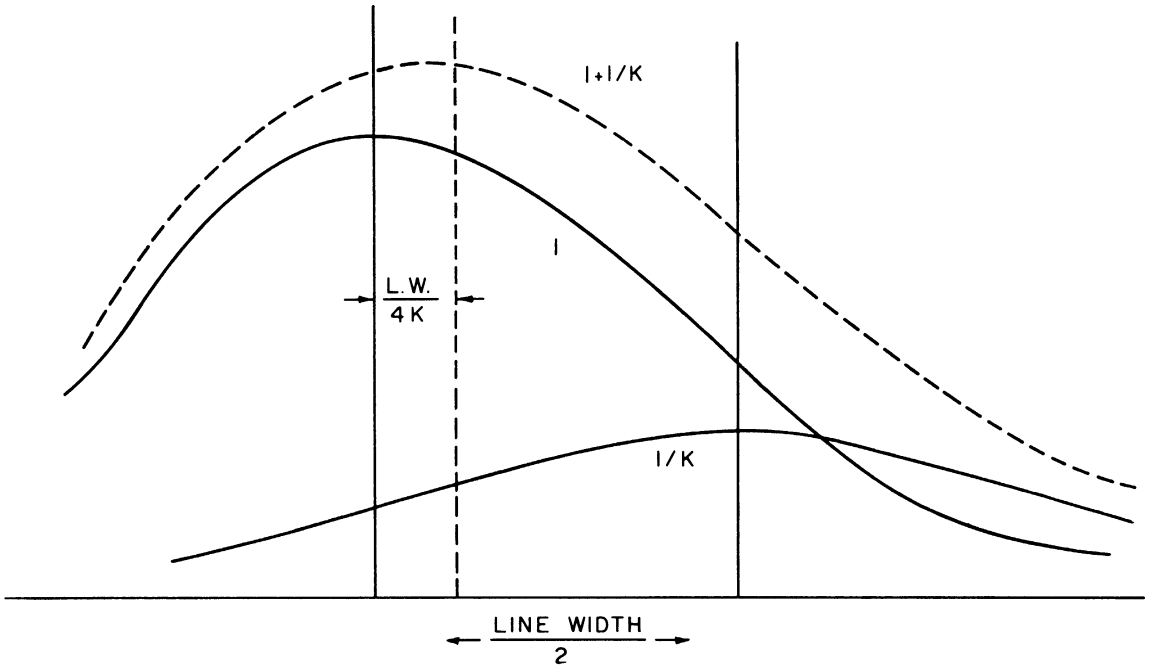

Figure 13. Line center shift due to overlapping lines.

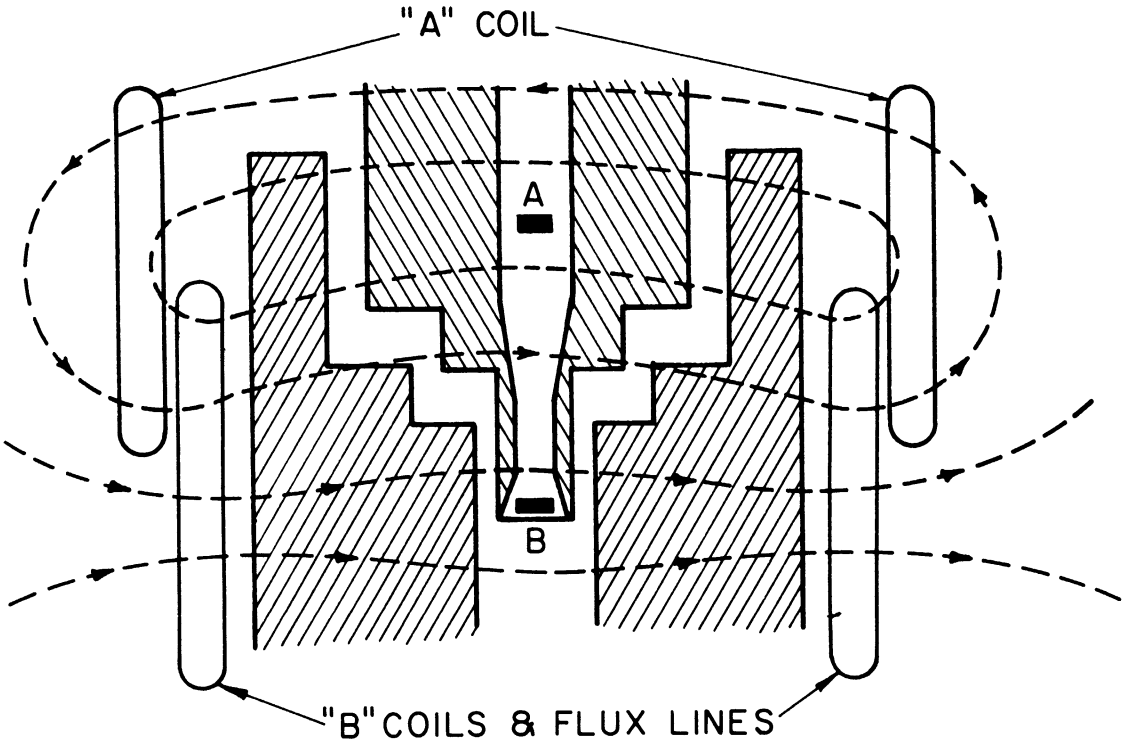

Figure 14. Bomb, coils, and flux lines schematic.

The choice of minimum permissible K is thus determined by the line width and the expected pressure shifts and in our case was about 10.

The primary criterion in determining the location of the second sample was that it be at a maximum in the microwave fields in the coaxial cavity, yet be as close as possible to the high pressure sample so that they both remain in the homogeneous portion of the DC magnetic field. This separation then determined the size of the modulation coils so that a pair of coils centered on one sample had a null at the other as shown in Figure 14. Without the pressure bomb and with proper orientation of the coils, $K_A = 10$ and $K_B = 10^3$ were obtained. However, with the bomb, $K_A = 10^4$ and $K_B = 1$. Consideration of these values and the bomb shape (schematically shown in Figure 14) and the fact that the skin depth at these frequencies is considerably smaller than the bomb thickness, lead to the conclusion that the modulation was being caused by induced currents. Therefore another method had to be used to eliminate the cross talk in channel B. Since this was due to the field modulation about sample B being carried up to and around sample A, but not vice versa, a portion of the B modulation signal can be inverted and fed into the A modulation to exactly cancel the cross talk. Thus K_B can be set by a phase and amplitude adjust-

ment of this feedback to be as large as desired or even infinity. In this manner, cross talk was reduced to less than one part in 10^4.

D. EXPERIMENTAL PROCEDURE

When there is more than one line falling within the sweep range of the DC magnetic field, the data taking is extremely simple. The known line separations on the atmospheric pressure chart provide a calibration for the high pressure chart. Using identical chart paper on recorders driven by the same shaft assures equality of recordings. (It was found, however, that the chart paper grid spacings and drive hole spacings are not always reliable.) Figure 15 shows a sketched pair of recordings for the first three fine structure lines for Mn^{++} in MgO. In actual practice the signals are driven a long way off scale in order to more accurately determine where the center of the absorption line falls (derivatives are what are plotted and constant line shape is assumed, which is supported by the work of Wait.[22]) In this method magnet hysteresis can be a problem unless a field sweep (as opposed to current sweep) is used or the sweep is calibrated.

If no close set of lines is available, the procedure is to stop the sweep exactly when the recorder shows the

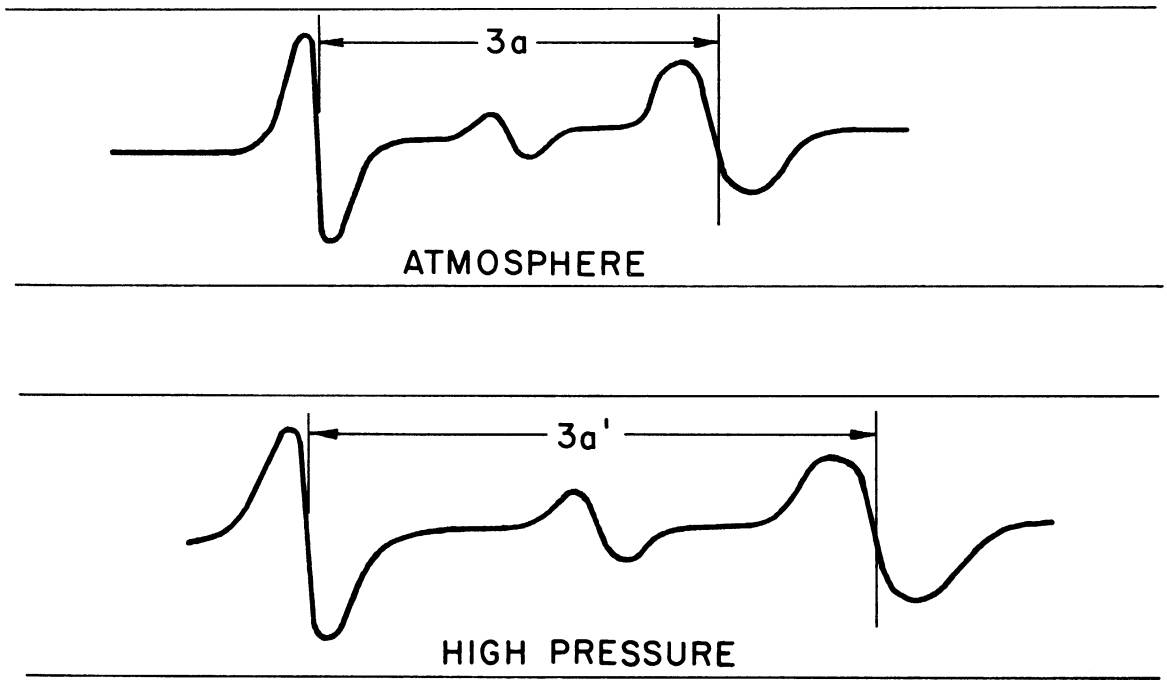

Figure 15. Sketch of pressure effect on Mn^{2+} in MgO lines.

derivative to be zero and measure the field with a nuclear magnetic resonance probe. Similarly, the field is measured for the shifted line. The difference between the field at the probe and that at the sample is of no concern as long as it is constant since the difference between resonance conditions is what is measured. The nuclear magnetic resonance probe used the proton resonance of a 0.2 molar solution of $CuCl_2$ in water for the low field lines and the deuteron resonance of a 1.0 molar solution of $CuCl_2$ in 99.9% pure heavy water for the high field lines.

The only other necessary measurement is that of the microwave frequency. The frequency does not appear in equations 40 and 42 but it is necessary to correct for any residual field difference between the two samples at atmospheric pressure. This difference must be subtracted from the pressure shifts and since the frequency changes a little with pressure, this zero pressure difference must be corrected with frequency as is explained in the data reduction in Appendix D. Since accuracy to better than one part in 10^4 was not necessary a previously calibrated absorption type wavemeter was used. This allowed frequency measurements to 0.001 Gc/sec out of about 9.4 Gc/sec. Table IV shows the calibration of the frequency meter when a transfer oscillator was used to measure the microwave frequency to better than one part in a million.

TABLE IV

Calibration of Absorption Frequency Meter HP X532A #15030 with a Transfer Oscillator Measurement.

Actual Frequency Gc/sec.	Frequency Meter Reading Gc/sec.
9.0468	9.0470
9.1792	9.1790
9.2157	9.2160
9.2234	9.2230
9.2345	9.2350
9.2614	9.2620
9.2951	9.2950
9.3433	9.3430
9.4003	9.4000
9.5073	9.5070

A list of all the electronic equipment used is given in Appendix E.

Chapter IV

RESULTS

A. Cr^{3+} IN SAPPHIRE

Data for the resonant field conditions as a function of hydrostatic pressure were taken for the single resonance line of the I = 0 Cr^{3+} ion at five positions of angle and field. These were the low field and midfield lines with the magnetic field parallel to the crystalline axis, the higher two lines at 54.7°, and one midfield line at 30°. The last three "off-axis" resonances were used primarily for a check. For the principle chromium isotope no hyperfine interaction exists and the resonance condition for the magnetic field parallel to the c axis shown as equation 14 in Chapter II becomes

$$h\nu = g_z \beta H + D[2M + 1] \qquad (56)$$

The most significant pressure dependence was observed for D,[70] the crystalline field parameter in the spin Hamiltonian. It will be discussed first followed by the results for g_z and A. All shifts were determined relative to the parameters obtained by Schulz-DuBois[37] and Laurence and Lambe,[39]

$$\begin{aligned} g_z &= 1.9840 \pm .0006 \\ 2D &= -11{,}493 \pm 6\text{Mc/sec.} \\ A &= B = 48.5\ \text{Mc/sec.} \end{aligned} \qquad (57)$$

which agreed with those obtained here, $g_z = 1.9850 \pm .001$ and $2D = -11,492 \pm 10$ Mc/sec.

D Shift. The pressure dependence of the zero field splitting, D, was determined with the low field line with the magnetic field parallel to the crystal axis and checked at three non-parallel positions. The low field line is due to the M = +3/2 to +1/2 transition for which equation 56 becomes

$$h\nu = g_z \beta H + 2D \quad . \tag{58}$$

Because the change in g_z was expected to be very small compared to that in D from previous pressure experiments and, indeed, showed to be small (5×10^{-5}/katm as opposed to 2×10^{-3}/katm.) from this study, it was neglected in obtaining the pressure shifts in D. Since both samples were subject to the same microwave frequency, the above resonant condition held for both the high pressure and reference samples so that

$$g_z \beta H' + 2D' = g_z \beta H + 2D \tag{59}$$

where the primes indicate the high pressure condition. Solving for the change in 2D gives

$$\Delta 2D = - g_z \beta \Delta H \quad . \tag{60}$$

The analysis of the experimental data is explained in Appendix D. The results are shown in Figure 16. Note that since D is negative, the results were plotted with increasing magnitude downward so that the negative slope implies a relative increase in magnitude. The $\Delta 2D$ obtained from this experiment was added to the value of 2D obtained from Schulz-DuBois.[37] A least squares fit to the straight line $y_i = a + bx_i$ gives a slope

$$b = -21.15 \text{ Mc/sec. katm.} \tag{61}$$

The error in the plotted values can be due to the field measurement, the pressure measurement, and the location of the zero condition of the absorption derivative. The field was measured to $\pm$ 0.15 kcP ("Proton" kilocycles/sec. for proton NMR probe, see Appendix D), or $\pm$ 0.1 Mc/sec. The pressure measurement was to $\pm$1 atmosphere in several thousand and is therefore neglected. The accuracy of the absorption line zero determination can be estimated from the line width, about 10 gauss, and the signal to noise ration, which was about 400:1. (The signals were driven off the recorders in order to enhance this accuracy in the zero determination.) Assuming constant line shape and linearity of the second derivative between the two points of maximum derivative yields an accuracy of $\pm$ 0.025 gauss, better than the accuracy of the field measurement. This was experimentally confirmed. Thus the error in $\Delta 2D$ becomes

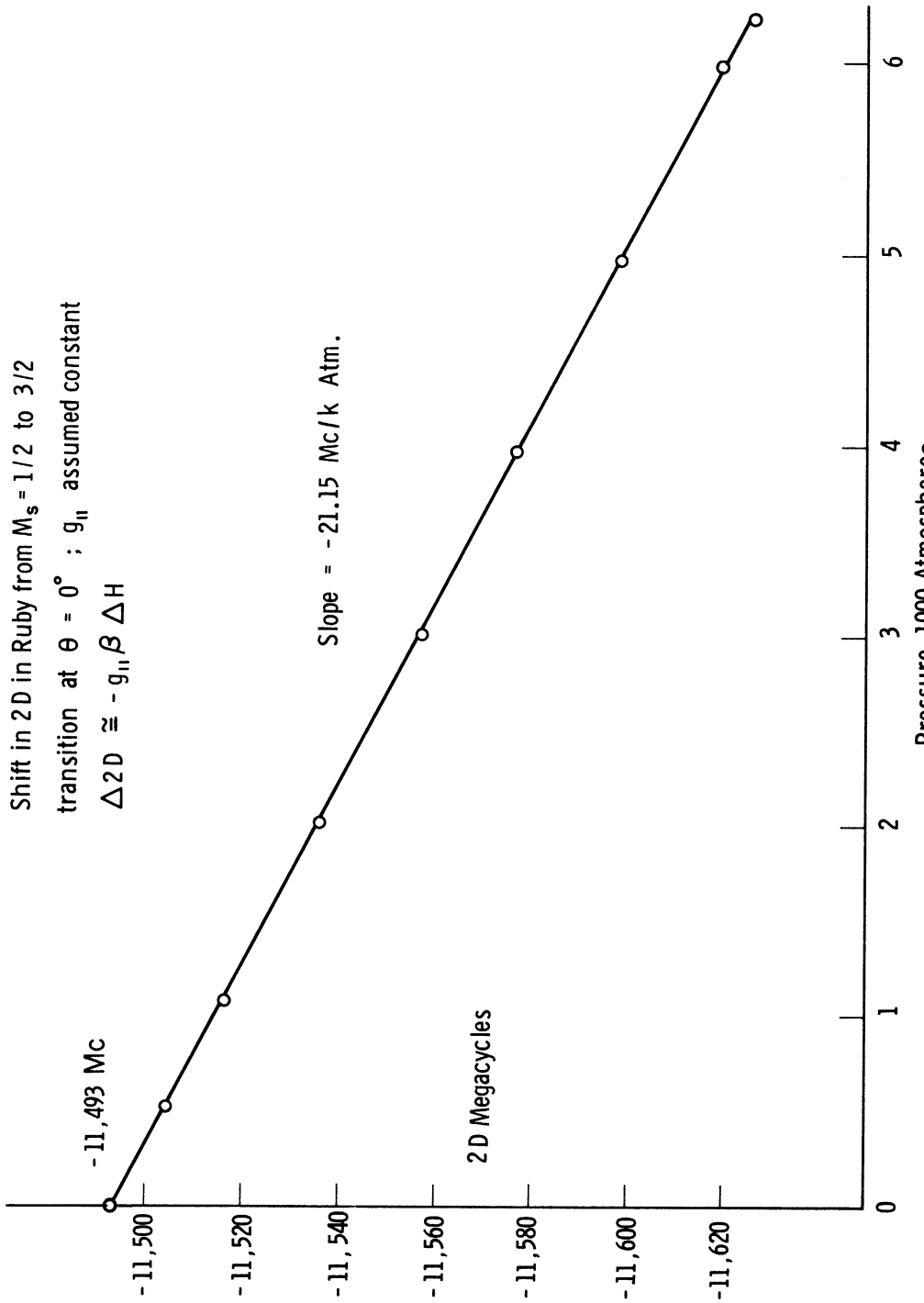

Figure 16. Zero field splitting versus pressure for Cr^{3+} in Al_2O_3.

$$E_{\Delta 2D} = \pm 0.1 \text{ Mc/sec.} \pm 0.1 \text{ Mc/sec.} = \pm 0.2 \text{ Mc/sec.} \quad (62)$$

This yields a relative change in 2D of

$$\frac{\Delta 2D}{2D} = (1.84 \pm 0.02) \times 10^{-3} / \text{k atm.} \quad (63)$$

The method used to check this value for other resonant conditions was to use the pressure dependence determined above and check for agreement in the transition energies, such as equations 17 and 18 in Chapter II, with the experimental data. This was done because of the extreme complexity in solving for D from these equations. In all cases the agreement to the second significant figure in the pressure shift was excellent.

g Shift. The pressure dependence of g_z, the impurity ion's gyromagnetic ratio, can be obtained directly from the midfield line with the magnetic field parallel to the c axis. The midfield line is the $M = -\frac{1}{2}$ to $M = \frac{1}{2}$ transition and equation 56 simplifies to

$$h\nu = g_z \beta H \quad (64)$$

Again, since both samples were in the same cavity and subject to the same microwave frequency, the resonant condition for both samples was the same and

$$g_z \beta H = g_z' \beta H' \qquad (65)$$

where the primes indicate pressure. This leads immediately to the result

$$\Delta g_z = g_z' - g_z = g_z \frac{H - H'}{H'} = -g_z \frac{\Delta H}{H'} \quad . \qquad (66)$$

Analyzing the results of the experiment as detailed in Appendix D led to the plot shown in Figure 17. In this plot the Δg_z determined experimentally was added to the g_z value from Shulz-DuBois.[37]

As can be seen from Figure 17 there is an initial first step of about 1×10^{-4} and the remaining points fall on an approximate line that has no slope outside of the experimental error but has a slight general upward trend. In the following discussion it will be shown that neither of these is significant.

The initial step between one and a few hundred atmospheres was reproducible and occurs in the region of the largest physical changes in the microwave cavity as indicated by the changes in the cavity frequency. For example, the total change in a 9.5 Gc/sec. frequency between 1 and 7000 atmospheres is about 120 Mc/sec. Of this, about 60 Mc/sec. occur in the first 100 atmospheres and 100 Mc/sec. in the first few hundred atmospheres. Because

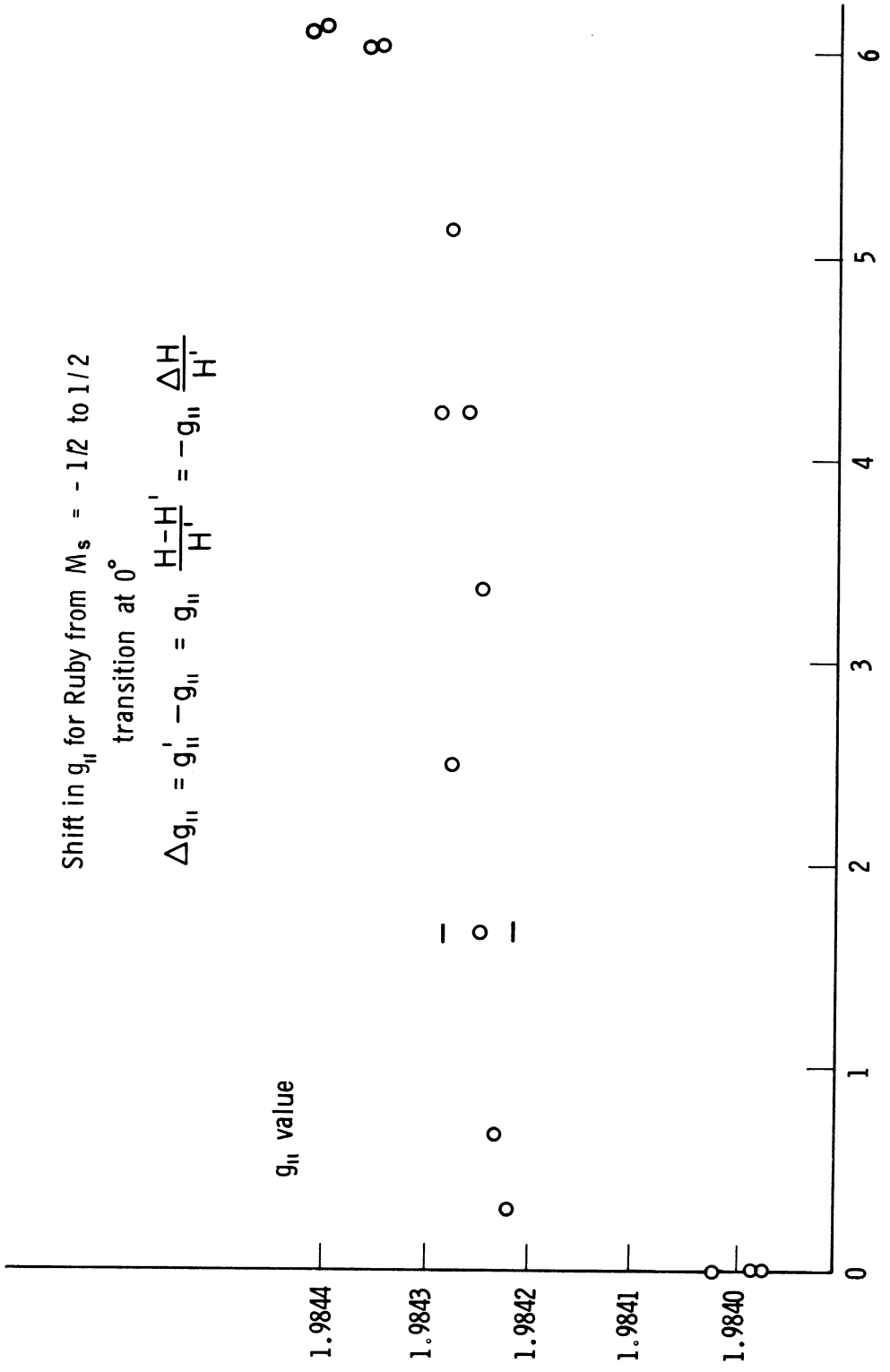

Figure 17. g value versus pressure for Cr^{3+} in Al_2O_3.

of this and the fact that the step maintained the relative sign and proportional magnitude of the remaining field difference when both samples were at atmospheric pressure, it is felt that this step was due to either rotational or vertical motion of the high pressure sample with respect to the reference sample. The rotational motion could arise from a circular motion of the pentane as it enters the sample holder in the initial compression but is not likely to be reproducible. The vertical motion arises from compression of the high pressure sealing cone shown in Figure 11 to which the sample holder is attached. This would be readily reproducible.

An order of magnitude of the effect can be estimated as follows. The sealing cone of mica has a thickness of 0.030" and a very small conical angle, ϕ . A compression of Δx in thickness will result in a vertical motion of $\Delta x/\sin \phi$. Since the angle is small, a vertical motion of about 0.030" can be taken as a reasonable upper limit. The samples are 1-3/4" apart so this is a 3% change. The zero pressure field difference due to slight misalighment or inequivalent fields at the two samples was 30 kcP. Assuming that this difference is linear a 3% change would allow a 1 kcP change which is equivalent to 2×10^{-4} in Δg_z, larger than the observed step.

Rotational motion would make the magnetic field no longer parallel to the crystalline axis and would allow mixing of the very large D term. This would add a correction term of the order of $D^2 \sin^2\vartheta / g_z \beta H$ where ϑ is now the small rotation. From the magnitude of the step, about one part in 2×10^4, an estimate of the necessary rotation can be found. Both $g_z \beta H$ and D are on the order of 10^4 Mc/sec. Thus, one part in 2×10^4 of $g_z \beta H$ is 0.5 Mc/sec., or

$$\frac{1}{2} Mc \sim \frac{D^2}{g_z \beta H} \sin^2\vartheta \sim \frac{D^2}{g_z \beta H} \vartheta^2$$

$$\frac{1}{2} Mc \sim \frac{(10^4)^2}{10^4} \vartheta^2 \, Mc \qquad (67)$$

$$\vartheta^2 \sim 1 / 2 \times 10^4$$

$$\vartheta \sim 1/140 \sim 1/3^\circ .$$

Thus a rotation of a few tenths degree could introduce such a step.

A check for rotation of the sample with cycling of the pressure was performed. The change of crystal orientation was observed by the motion of resonance lines as explained in Chapter III, Part A. This could be done to $\pm 0.2^\circ$ and no motion was observed. This does not preclude, however, that this effect does not contribute, but is an indication that it is less likely.

The slight slope shown in Figure 17 is well inside the experimental error. In spite of this an effort was made to see if it could be significant. As shown in Appendix D the zero pressure field difference correction was normalized to the zero pressure condition. This correction is not the same when normalized to a different pressure. Re-normalization to the next lowest pressure decreased the slope somewhat. This, coupled with the fact that in re-checks of the g shift the slope disappeared and in one case was slightly negative corresponding to a larger negative initial step, led to the conclusion that the two effects are interconnected and the slope is not significant.

In any case, an upper limit can be put on the change in the g_z value or change in the difference in g_z from the free ion value of $g_o = 2.0023$. By far the largest error occurs in ΔH since g_z is fixed and H' is measured to one part in 10^5. From Appendix D

$$\Delta H = H_{bx}' - \left\{ H_{ax} + \frac{\nu_x}{\nu_o}(H_{bo} - H_{ao}) \right\} \qquad (68)$$

where all the fields are measured to ± 0.15 kcP in 1.5×10^4 kcP and ν to five parts in 10^5. It is assumed that the field inhomogeneity does not change. The facts that the step was reproducible within other experimental errors and the field was always cycled repeatedly before measurements support this assumption.

Therefore an error estimate for ΔH would be

$$E_{\Delta H} = \pm 10^{-5} \pm 10^{-5} \pm \left[(5\times10^{-5})^2 + (5\times10^{-5})^2 + (10^{-5}+10^{-5})^2\right]^{1/2}$$

$$E_{\Delta H} = \pm 2\times10^{-5} \pm 7\times10^{-5} \cong 10^{-4} \qquad (69)$$

Thus

$$\frac{\Delta g_z}{g_z} \lesssim \frac{1\times10^{-4}}{2.0} = 5\times10^{-5} \qquad (70)$$

or since $g_o - g_z$ is about 2×10^{-2}

$$\left|\frac{\Delta(g-g_o)_z}{(g-g_o)_z}\right| \lesssim \frac{5\times10^{-5}}{2\times10^{-2}} = 2.5\times10^{-3} \qquad (71)$$

over a range of several thousand atmospheres. Therefore it can be said that the change in the difference between g_z and the free ion value of g_o is certainly less than 2.5×10^{-3} and probably on the order of 1×10^{-3}/katm. or less.

A Shift. An attempt was made to observe a shift in the hyperfine splitting due to the Cr^{53} isotope which is 9.5% abundant and has an I = 3/2. Only the two outermost hyperfine lines, m = $\pm$ 3/2, were observable and only at the midfield line with the magnetic field parallel to the crystalline axis. They were observed as two "pips" or "wings" on the sides of the very broad I = 0 resonance.

Because there was no clear cut zero to the derivative of these absorption lines, a determination of the **A** value could be made to only two parts in one thousand. **A** slight decrease in **A**, on the order of 0.5×10^{-3}/katm., was noticed. This shift was the same order of magnitude as observed elsewhere (0.6, 0.44, and 0.035×10^{-3}/katm.[20,22]) but since **A** could only be determined to 2×10^{-3}, it was inconclusive.

B. V^{2+} IN SAPPHIRE

The spectra for the V^{2+} ion in sapphire is more complex than that for ruby. This is primarily due to the addition of the hyperfine interaction with the vanadium nucleus which has a nuclear spin of 7/2. With small (2^{o}) misalignments, forbidden hyperfine transitions are allowed so that only when the magnetic field is parallel to the crystalline axis is the eight line "signature" of vanadium undistorted. Further complications arise because at X band frequencies the midfield transition occurs very near the energy level crossing indicated as a dotted enclosure in Figure 3. Both here and at the low field transitions the mixing of states has been observed[39] resulting in a very complicated spectrum. Since the ruby data indicated that g shifts could not be observed, g was assumed constant as before, and the necessary data was

taken from the high field lines, the only usable spectrum at X band frequencies, for which M = + 1/2 to +3/2. For the above case equation 14 in Chapter II becomes

$$h\nu = g_z \beta H + 2D + Am + f \tag{72}$$

where f is the second order hyperfine correction terms and is a function of A, G, g_z, H, D, and m.

The concentration of the V^{3+} ions in the vanadium impurity samples was the same as that for the Cr^{3+} ions in the ruby samples. Because the conversion of the V^{3+} ions to V^{2+} ions by X irradiation is not very high and the same signal strength is now spread over eight lines instead of one, the signal to noise ratio was considerably reduced. The cross talk bucking circuit described in Chapter III, which eliminated the sample cross talk between channels, is obviously dependent on the modulation amplitude. Because the modulation negative feedback is dependent on both modulation amplitudes, maximizing the high pressure sample signal while still eliminating the cross talk resulted in insufficient signal to noise for the reference sample signals. No reasonable balance which maintained the required accuracy was possible so a straightforward determination of the parameters A and D as a function of pressure was done using only the high pressure sample. In order to overdetermine the values, the resonant

conditions were observed for the first three (most clear) hyperfine lines at each pressure, for which m takes the values -7/2, -5/2, and -3/2.

The data was analyzed as detailed in Appendix D by an iterative process. Since the value of A was expected to change very little compared to the change in D, it was assumed constant with pressure. The zero pressure parameters were taken from the work of Laurence and Lambe[39] and are:

$$\begin{aligned} g_z &= 1.991 \\ 2D &= -9,607.2 \pm 2.0 \text{Mc/sec.} \\ A &= -220.615 \pm 0.025 \text{ Mc/sec} \\ B &= -222.890 \pm 0.100 \text{ Mc/sec.} \end{aligned} \tag{73}$$

Once D as a function of pressure was determined, its dependence was used to determine the dependence of A. From these the second order correction was corrected for pressure and the process repeated.

D Shift. The results of this analysis for the pressure dependence of the zero field splitting are shown in Figure 18. Again, the D value increases in magnitude and is plotted downward as an increase in a negative number. The slope by a least squares fit to the straight line $y_i = a + bx_i$ is

$$b = -17.0 \text{ Mc/sec. katm.} \tag{74}$$

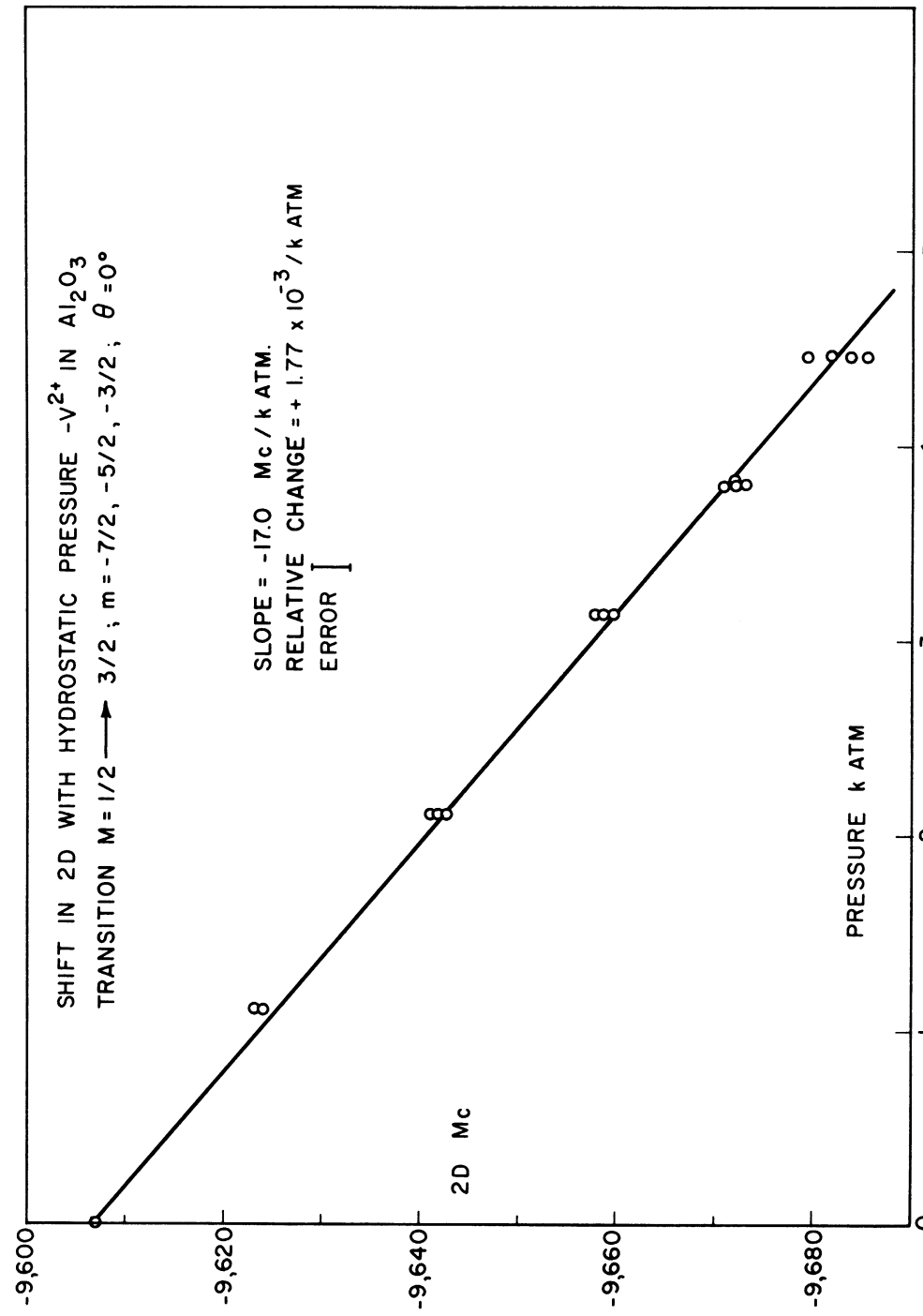

Figure 18. Zero field splitting versus pressure for V^{2+} in Al_2O_3.

The error is now larger because there are additional differences in the calculation and the signal to noise ratio was reduced. Also, the resonance probe for field measurements used a deuteron resonance so the ±0.15 kcD becomes about ±0.7 Mc/sec. The uncertainty in this value due to the reduced signal to noise ratio (50:1) raises this to ±1.0 Mc/sec. Since Δ2D is now

$$\Delta 2D = h\nu' - h\nu + g_z \beta H - g_z \beta H' \tag{75}$$

the error in Δ2D becomes

$$E_{\Delta 2D} = \pm 0.5 \pm 0.5 \pm 1.0 \pm 1.0 = \pm 3.0 \ Mc/sec. \tag{76}$$

This yields a relative change in 2D of

$$\frac{\Delta 2D}{2D} = (1.77 \pm 0.1) \times 10^{-3} / k \ atm. \tag{77}$$

A Shift. The larger errors here were expected to mask any pressure shifts in A unless they were unusually large. Expected shifts from other experiments would be on the order of 10^{-3}/katm. With the value A = -220 Mc/sec., this would be shifts of about 0.2 Mc/sec. katm. which is well inside the experimental error. No large shifts were observed. However, the data showed again a slight decrease, as in the case for ruby, of the expected order of magnitude. But this also was termed inconclusive.

C. SUMMARY

Listed below are the changes in the spin Hamiltonian parameters with hydrostatic pressure determined in this experiment on Cr^{3+} and V^{2+} ions in α-Al_2O_3.

Cr^{3+}

$$\frac{\Delta 2D}{2D} = (1.84 \pm 0.02) \times 10^{-3} / \text{k atm.}$$

$$\left| \frac{\Delta (g - g_0)_{\parallel}}{(g - g_0)_{\parallel}} \right| \lesssim 2.5 \times 10^{-3} / \text{k atm.}$$

V^{2+}

$$\frac{\Delta 2D}{2D} = (1.77 \pm 0.1) \times 10^{-3} / \text{k atm.}$$

Chapter V

CONCLUSIONS

A. DIRECT CONCLUSIONS

Hydrostatic compression of the sapphire lattice containing isoelectronic V^{2+} and Cr^{3+} impurities has shown that the crystalline field parameter, D, in the spin Hamiltonian varies linearly with pressure to about 7000 atmospheres for both ions. In addition, the relative changes, $\Delta D/D$, for both ions are very close in value and indicate an increase in magnitude. Similar results have been obtained for the cubic field splitting of other isoelectronic ions. Mn^{2+} and Fe^{3+} in MgO[20] and Gd^{3+} and Eu^{2+} in $SrTiO_3$[23] show this same identity in behavior with pressure. With no other considerations it can be concluded that both the V^{2+} and Cr^{3+} ions occupy the same or very closely the same lattice position, though not necessarily the aluminum site, and that the compressibility about each ion is nearly identical.

The implication that the ions occupy similar sites in the same lattice is supported by the identical pressure dependence of Dq found by Drickamer for five different ions (Ti^{3+}, V^{3+}, Ni^{2+}, Cr^{3+}, and Ni^{3+}) in sapphire.[34,36] It is in opposition to the substitutions proposed by Weakliem and McClure,[41] who postulated a varying displacement along

the c axis to explain the differences in the trigonal field parameter calculated from optical spectra for various triply ionized ions (Ti^{3+}, V^{3+}, Cr^{3+}, Mn^{3+}, Co^{3+}, and Ni^{3+}) in sapphire.

However, equal trigonal field parameters were found by Geschwind and Remeika[71] who carried out precise measurements of the anisotropy of the g shifts from EPR spectra. The anisotropy in $g-g_o$ arises because different excited states are coupled to the ground state for $(g-g_o)_z$ and $(g-g_o)_\perp$,(see Appendix G). Since the excited states are split by V_{ax}, this anisotropy can be used to determine the splitting. They observed the 3d ions Co^{2+}, V^{3+}, Cu^{3+}, and Ni^{2+} and the 4d ion Ru^{3+} in sapphire and determined nearly equal trigonal fields for all but Cu^{3+} and Ni^{2+}. Kamimura[63] has recently explained this behavior and by invoking distortion of the covalent bonds of the impurity has determined equal trigonal fields for all of the above ions implying similar positions.

Another experiment discussing ion position is by Laurence and Lambe[39] who observe widely different values of the electric field gradient at the impurity nucleus in ENDOR experiments for the isoelectronic ions V^{2+}, Cr^{3+}, and Mn^{4+} in sapphire. These values and other data are collected in Table V. They point out, however, that the variation in the electric field gradient (non-monotomic and opposing signs) shown in Table V cannot be quantitatively explained by simple point charge model displacement.

TABLE V

Comparison of crystal field parameters for V^{2+}, Cr^{3+}, and Mn^{4+} in sapphire.

	V^{2+}	Cr^{3+}	Mn^{4+}
$10Dq$ $(cm.^{-1})$	13,600 [43]	18,000 [13] 16,670 [63]	21,300 [79]
$\frac{\Delta Dq}{Dq}$ $(\times 10^{-3}/k\ atm.)$	—	0.60 ± 0.01 [36]	—
$-K$ $(cm.^{-1})$	160 [43]	475 [41] 350 [63] 330 [43]	700 [43]
$\frac{\Delta K}{K}$ $(\times 10^{-3}/k\ atm.)$	—	UNOBS. TO 60kbar 6.0 [36] ABOVE "	—
$-2D$ $(cm.^{-1})$	0.32 [39]	0.383 [37]	0.391 [79]
$\frac{\Delta 2D}{2D}$ $(\times 10^{-3}/k\ atm.)$	1.77 ± 0.1	1.84 ± 0.02 [26] 1.41 ± 0.7 [26] 1.58 ± 0.8 [28]	—
$g_{\parallel}$	1.991 [39]	1.9840 [37]	1.994 [79]
$g_{\perp}$		1.9867 [37]	
$\frac{\Delta(g-g_0)_{\parallel}}{(g-g_0)_{\parallel}}$ $(\times 10^{-3}/k\ atm)$	—	≤ 2.5	—
B_{RACAH} $(cm.^{-1})$	550 [43]	700 [63] 640 [13] 630 [36]	700 [79]
$\frac{B}{B_{FREE\ ION}}$	0.73 [43]	0.78 [36] 0.76 [43]	0.66 [43]
$\frac{\Delta B}{B}$ $(\times 10^{-3}/k\ atm.)$	—	-0.32 ± 0.01 [36]	—
λ $(cm.^{-1})$	12.35 [43]	70 [44] 63 [63]	$\simeq \lambda_{Cr^{3+}}$ [79]
$\frac{\lambda}{\lambda_{FREE\ ION}}$	0.65 [43]	0.78 [44] 0.73 [63] 0.62 [43]	$> \frac{\lambda}{\lambda_{F.I\ Cr^{3+}}}$ [79]

	V^{2+}	Cr^{3+}	Mn^{4+}	Al^{3+}
Q^{39} (b)	0.3	-0.03*	0.35	1.49
$(1-\gamma_\infty) eq^{39}$ (Mc/b)	-1.87	27.4*	5.26	16.1
$(1-\gamma_\infty)^{39}$	12.7	10.8	9.5	3.6 5.0
$\frac{A}{\gamma}^{39}$ (gauss)	-197,200	-201,600	-197,900	—
r_G (Goldschmitt rad. in a.u. = 0.53 Å)	1.36	1.23	0.98	0.96
$<r>^{**}$ (a.u.)	1.28	1.08	0.97	
$<r^2>^{**}$ $(a.u.)^2$	2.06 (2.4)	1.45 (2.7)	1.11 (3.2)	
$<r^4>^{**}$ $(a.u.)^4$	9.50 (12.8)	4.45 (15.7)	2.39 (19.8)	

* No independent determination of Q has been done. These values were arrived at by assuming the field gradient was the same as for Al^{3+}.

** Calculated by Watson from Hartree-Fock wave functions. Those in parantheses determined experimentally from $10Dq = 4q\langle r^4\rangle / 3R^5$ and linear scaling to $\langle r^2 \rangle^{.43}$

It should be pointed out that all of the above determinations except the field gradient have involved the spin-orbit coupling whose anisotropy[63] must also be accounted for as still another parameter. Examining the previous experiments as to the location of the ions, only two imply varying displacements. Laurence and Lambe calculate a displacement for the Cr^{3+} ion and propose other distortions to explain the other electric field gradients. Weakliem and McClure[41] originally proposed displacement from varying axial field parameters determined from optical spectra. The axial field parameters from EPR spectra[71] do not show this variation, even though both were determined from the many parameter crystal field theory.

In a molecular orbital calculation Lohr and Lipscomb show that the zero field splitting, 2D, is a more sensitive function of position than is the trigonal field splitting, 3/2 K, which is more sensitive to configuration mixing. From the similarity of the values of 2D from Table V and the above discussion, it seems reasonable to conclude in agreement with Drickamer[34,36] and Geschwind and Remeika[71] and Kamimura[63] that the Cr^{3+} and V^{2+} ions substitute in similar sites in the sapphire lattice though not necessarily the aluminum site. Further analysis at the end of the next section supports this conclusion.

The difference in charge of the two ions, V^{2+} and Cr^{3+}, suggests that the local compressibilities would be different. The local ionic binding energy would be expected to be significantly lower for V^{2+} leading to a higher local compressibility.[20] Also, the polarization of the O^{2-} ions[72] would be less, leading to a higher local compressibility. But the similar pressure dependence implies that these charge dependent effects are not noticeably different for the two ions. Though the V^{2+} ion is larger and higher covalency would be probable, the values of B/Bo and λ/λ_o from Table V indicated no significant difference, so one would expect no difference in compressibility due to a different degree of covalency. The fact that no anomalously large shifts in the difference of the g value from that of the free ion, $g-g_o$, or in the hyperfine splitting term, A, are observed implies that the local compressibility is the same or smaller than the bulk compressibility for sapphire. Thus it can be concluded, in agreement with Drickamer[34,36] that the compressibility about the different ions is the same and comparable to that of the bulk compressibility of sapphire. A further test of this discussion would, of course be the pressure dependence of Mn^{4+} in sapphire.

B. ANALYTICAL CONCLUSIONS

It is worthwhile to compare the results obtained in this experiment with those from a spin-phonon interaction experiment by Tucker[28] and a uniaxial stress EPR experiment on ruby performed by Terhune[26]. Tucker analyzed his experiment for longitudinal acoustic waves along the c axis with the interaction represented by a perturbation of the form

$$\mathcal{H}' = G e_{zz} S_z^2 \tag{78}$$

where G is defined as the magnetoelastic coupling constant and e_{zz} the elastic strain amplitude. The product Ge_{zz} is the change in the coefficient of S_z^2 with uniaxial displacement and should therefore yield the $\Delta 2D$ for a uniaxial pressure experiment. He obtains a value of $G^2 = 2.8 \times 10^{-30}$ $(ergs)^2$ for longitudinal acoustic waves along the c axis. (Note: The reference 28 reads 1.5×10^{-29} but this has been corrected by private communication[26] to the quoted value.) This yields a $\Delta 2D/2D = 4.5 \times 10^{-3}$/katm. From this and the data perpendicular to the c axis a hydrostatic pressure shift of $\Delta 2D/2D = 1.58 \times 10^{-3}$/katm. is predicted which has an error of about 50%. In the uniaxial stress experiment Terhune obtained a value of $\Delta 2D/2D = (5.2 \pm 0.3) \times 10^{-3}$/katm. for a stress parallel to the c axis. From this and the value obtained perpendicular to the c axis,

he predicted a hydrostatic pressure shift of $\Delta 2D/2D = 1.41 \times 10^{-3}$/katm. also with an error of 50%. Both of these predictions include the observed value for hydrostatic compression of $\Delta 2D/2D = 1.84 \times 10^{-3}$/katm.

The observed values of changes in D with hydrostatic and uniaxial compression can now be compared to those changes predicted for the a_{20} term in the crystalline field expansion shown in Table III. This can be done using equations 49 and 51 (Chapter II) which are

$$\frac{\Delta 2D}{2D} \cong \frac{\Delta \delta}{\delta} + \frac{2\Delta \lambda}{\lambda} - \frac{2\Delta D_q}{D_q} \qquad (49)$$

and

$$\frac{\Delta (g-g_0)_z}{(g-g_0)_z} \cong \frac{\Delta \lambda}{\lambda} - \frac{\Delta D_q}{D_q} \qquad (51)$$

The parameters on the right are proportional to the position variables as follows:

$$\delta \propto a_{20} \langle r^2 \rangle \qquad (79)$$

$$\lambda \propto \langle r^{-3} \rangle \qquad (80)$$

$$D_q \propto \langle r^4 \rangle R^{-5} \qquad (81)$$

where $< r^n >$ indicates the average value of r^n over the radial part of the 3d wave functions.

There is a reasonable amount of evidence that $g-g_o$ varies with pressure primarily as Dq^{-1}. Drickamer's experiment[36] showed that for ruby Dq behaves like R^{-5} to about 50,000 atm., implying that $< r^4 >$ changes very little in our pressure range. In Walsh's experiment[20] on Cr^{3+} and Ni^{2+} in MgO, he obtains values of $\frac{\partial \ln (g-g_o)}{\partial \ln V}$ 2.0 $\pm$ 0.2 and 1.9 $\pm$ 0.3 respectively. The corresponding values for $\frac{\partial \ln Dq}{\partial \ln V}$ from Minomura and Drickamer[34] are 1.84 and 2.0. This is an indication that both $< r^4 >$ and $< r^{-3} >$ also change very little. In the same experiment Minomura and Drickamer observe (as in ruby[36]) that the Racah B parameter changes very little, .026%/katm.

From the above discussion and the small change in B for ruby it seems reasonable to conclude that to a first approximation $< r^n >$ changes insignificantly, and the parameters in equations 79-81 become

$$\frac{\Delta \delta}{\delta} \cong \frac{\Delta a_{20}}{a_{20}} \tag{82}$$

$$\frac{\Delta \lambda}{\lambda} \cong 0 \tag{83}$$

$$\frac{\Delta Dq}{Dq} \cong -5 \frac{\Delta R}{R} \tag{84}$$

Substitution of a value for $\Delta Dq/Dq$ calculated from equation 84 and the elastic constants and of the point charge model values of $\Delta a_{20}/a_{20}$ from Table III for a substitutional position and +0.15 Å removed yields equation 85 and 85', respectively. These are (in units of 10^{-3}/katm.)

$$\frac{\Delta 2D}{2D} = 0.67 \pm 0.01 + 2(-0.68 \pm 0.01) = -.72 \pm 0.03 \tag{85}$$

$$\frac{\Delta 2D}{2D} = 0.48 \pm 0.01 + 2(-0.68 \pm 0.01) = -.88 \pm 0.03 \tag{85'}$$

which are compared to the experimental value of 1.84 ± 0.02. Similarly the uniaxial pressure values give

$$\frac{\Delta 2D}{2D} = 3.86 \pm 0.01 + 2(-0.6 \pm 0.01) = 2.66 \pm 0.03 \tag{86}$$

$$\frac{\Delta 2D}{2D} = 1.30 \pm 0.01 + 2(-0.6 \pm 0.01) = 0.10 \pm 0.03 \tag{86'}$$

which are compared to the experimental value of 5.0 ± 0.2, where 86' is for the removed position and $\Delta Dq/Dq$ is now Drickamer's experimental value. If relocation of the impurity ion is used to look for agreement, in both pressure cases the ion position would have to be far removed in the opposite direction from that proposed by McClure,[42] Laurence and Lambe,[39] and Lohr and Lipscombe.[44] There is also no position at which both equations would agree, so sub-

stitution of the impurity ion at a site other than the aluminum site cannot account for the results without relaxing the other basic assumptions.

The three other basic assumptions from Chapter II-E which were used to look for agreement can now be questioned. These were:

1. The change in the spin Hamiltonian parameters is due to changes in the crystalline field.
2. The local compressibility is the same as the bulk compressibility.
3. The point charge model can be used to describe the changes.

With regard to the first assumption, the optical experiment using uniaxial pressure on ruby by Drickamer[36] showed that equation 84 appears to be applicable. This and the small decrease in B were used (see Chapter II-E) to assure this assumption. The same experiment was also used to assure the second assumption. Since it is one of the objectives of this study to check on the last assumption and since the other assumptions are experimentally supported, it can be concluded that the point charge model is inadequate to describe the observed pressure effects.

Disregarding any other experiments and relaxing all the assumptions except that of the point charge model, a check

on the D shift, equation 49, can be done using the g shift, equation 51. Substitution of the latter into the former yields

$$\frac{\Delta 2D}{2D} \cong \frac{\Delta \delta}{\delta} + 2 \frac{\Delta (g - g_0)_z}{(g - g_0)_z} \tag{87}$$

or substituting the Table III values for $\Delta a_{20}/a_{20}$ as before and the experimental upper limit for $\Delta(g-g_0)/(g-g_0)$ yields

$$\frac{\Delta 2D}{2D} \leq 0.64 \pm 0.01 + \frac{\Delta \langle r^2 \rangle}{\langle r^2 \rangle} + 2(2.5) \tag{88}$$

$$\frac{\Delta 2D}{2D} \leq 0.48 \pm 0.01 + \frac{\Delta \langle r^2 \rangle}{\langle r^2 \rangle} + 2(2.5) \tag{88'}$$

which are compared to the experimental value 1.84 $\pm$ 0.02. Thus, this experiment alone does not eliminate possible agreement and an accurate value of the g shift is desired. However, arguments will now be given that any expected value of a $\Delta(g-g_0)/(g-g_0)$ would be negative and stronger than $\Delta\langle r^2 \rangle / \langle r^2 \rangle$, again leading to disagreement.

Stuart and Marshall[48] have argued that the decrease in the spin-orbit coupling parameter, λ, for a free ion upon substitution into a crystal is primarily due to expansion of the impurity ion wave functions. This arises from screening of the 3d electrons by overlap of the ligand charge clouds. They postulate that the

radial wave function expansion can be represented to a first approximation by a simple scaling factor with appropriate renormalization, i.e.

$$f(r)_{SOLID} = k^{3/2} f(kr)_{FREE} \quad ; \quad k < 1 \quad . \tag{89}$$

They have quantitatively supported this approximation with neutron scattering form factors for Mn^{2+} ions and super-hyperfine splittings in MnF_2 with $k \simeq 0.9$ going from the free ion to the solid. With this approximation the variables ζ , λ , and Dq will now have a k dependence from equations 79-81 with k decreasing further with compression. For example, consider the integral of r^2,

$$\langle r^2 \rangle_{SOLID} = \int f(r)_{SOLID} \, r^2 \, f(r)_{SOLID} \, r^2 dr \quad .$$

Substituting the scaled free ion wave function yields

$$\langle r^2 \rangle_{SOLID} = \int k^{3/2} f(kr)_{FREE} \, r^2 \, k^{3/2} f(kr)_{FREE} \, r^2 dr$$

or

$$\langle r^2 \rangle_{SOLID} = \frac{1}{k^2} \int f(kr)_{FREE} \, k^2 r^2 \, f(kr)_{FREE} \, k^2 r^2 dr \quad .$$

But since a change of variable doesn't affect the integral

$$\int f(kr)_{FREE} \, k^2 r^2 \, f(kr)_{FREE} \, k^2 r^2 dr = \int f(r)_{FREE} \, r^2 f(r)_{FREE} \, r^2 dr = \langle r^2 \rangle_{FREE}$$

and one obtains

$$\langle r^2 \rangle_{SOLID} = \frac{1}{k^2} \langle r^2 \rangle_{FREE} \quad .$$

Similarly the k dependence of all the parameters can be shown to be

$$\begin{aligned} \delta &\propto a_{20} k^{-2} \\ \lambda &\propto k^3 \\ Dq &\propto k^{-4} R^{-5} \\ g - g_0 &\propto \lambda / Dq \propto k^7 R^5 \end{aligned} \quad . \tag{90}$$

For small decreases in k ($\Delta k/k$ is a negative number) equation 87 becomes

$$\frac{\Delta 2D}{2D} \cong \frac{\Delta a_{20}}{a_{20}} - 2 \frac{\Delta k}{k} + 14 \frac{\Delta k}{k} + 10 \frac{\Delta R}{R} \tag{91}$$

or

$$\frac{\Delta 2D}{2D} \cong \frac{\Delta a_{20}}{a_{20}} + 12 \frac{\Delta k}{k} + 10 \frac{\Delta R}{R} \tag{92}$$

or substituting values as before

$$\frac{\Delta 2D}{2D} \cong 0.64 \pm 0.01 + 12 \frac{\Delta k}{k} + 10 \frac{\Delta R}{R} \tag{93}$$

$$\frac{\Delta 2D}{2D} \cong 0.48 \pm 0.01 + 12 \frac{\Delta k}{k} + 10 \frac{\Delta R}{R} \quad . \tag{93'}$$

Since $\Delta k/k$ and $\Delta R/R$ are both negative numbers for compression, agreement still is not possible with the point charge model.

Now it is possible to look analytically at the equality of $\Delta D/D$ for V^{2+} and Cr^{3+}. Equation 49 with the variation of all the parameters becomes

$$\frac{\Delta 2D}{2D} \cong \frac{\Delta a_{20}}{a_{20}} + \frac{\Delta \langle r^2 \rangle}{\langle r^2 \rangle} + 2\frac{\Delta \langle r^{-3} \rangle}{\langle r^{-3} \rangle} - 2\frac{\Delta \langle r^4 \rangle}{\langle r^4 \rangle} + 10\frac{\Delta R}{R} \qquad (94)$$

or in terms of the expansion scaling factor, k,

$$\frac{\Delta 2D}{2D} \cong \frac{\Delta a_{20}}{a_{20}} + 12\frac{\Delta k}{k} + 10\frac{\Delta R}{R} \quad . \qquad (95)$$

The expansion factors, k, would not be expected to vary significantly between V^{2+} and Cr^{3+}. In fact, $\lambda/\lambda_{\text{free ion}}$ in this analysis equals k^3. From Table V the values of $\lambda/\lambda_{f.i.}$ are similar so the factors $k = \sqrt[3]{\lambda/\lambda_{f.i.}}$ are quite similar and $\Delta k/k$ in equation 95 for Cr^{3+} and V^{2+} should thus be nearly identical.

Disregarding the expansion one can argue similarly for equation 94 from the equality of the pressure dependence of the cubid field splitting, a, for isoelectronic S-state ions, which was indicated earlier[20,23]. The cubic field splitting for S-state ions depends in some manner on λ and Dq and therefore on $\langle r^{-3} \rangle$, $\langle r^4 \rangle$, and R. The fact that the pressure dependencies are equal in the same lattice implies that either $\Delta\langle r^{-3} \rangle/\langle r^{-3} \rangle$ and $\Delta\langle r^4 \rangle/\langle r^4 \rangle$ are

the same for isoelectronic ions or small compared to $\Delta R/R$. In either case one could expect the same to hold true for $\Delta \langle r^2 \rangle / \langle r^2 \rangle$.

Assuming, therefore, that the $\frac{\Delta \langle r^n \rangle}{\langle r^n \rangle}$ (or the $\frac{-n \Delta k}{k}$) are the same for both ions and knowing the experimental equivalence of $\Delta 2D/2D$ one can write

$$\left(\frac{\Delta 2D}{2D}\right)_{Cr^{3+}} \cong \left(\frac{\Delta 2D}{2D}\right)_{V^{2+}} \tag{96}$$

or

$$\left(\frac{\Delta a_{20}}{a_{20}}\right)_{Cr^{3+}} + \left(10\frac{\Delta R}{R}\right)_{Cr^{3+}} \cong \left(\frac{\Delta a_{20}}{a_{20}}\right)_{V^{2+}} + \left(10\frac{\Delta R}{R}\right)_{V^{2+}} .$$

Since a_{20} and R are parameters that depend only upon the lattice and not the ions, it can be concluded that the ions occupy similar lattice sites and are subject to similar compressibilities.

C. SUMMARY

In summary, it can be concluded that:

1. The V^{2+} and Cr^{3+} ions occupy similar lattice sites, though possibly including the displacements proposed in the literature.
2. The local compressibilities about the ions are similar.
3. The local compressibility is approximately the same as the bulk compressibility.
4. The point charge model is inadequate to predict the pressure changes.

D. FURTHER STUDIES

The most immediately useful experiment which would complement the work reported here would be a determination of the changes in Dq and λ with hydrostatic pressure for ruby. The former can be done optically but a direct determination of the latter is currently unknown. Since the pressure dependence of the g shift involves λ and Dq in the same manner as in the pressure dependence of D, a complete quantitative analysis according to equations 49 and 51 for ruby could also be done with a better determination of the change in the g shift and a more realistic prediction of the change in ζ. The latter could be done by a molecular orbital calculation, such as done by Lohr and Lipscomb,[44] as a function of displacement of the surrounding ions, and the former is discussed in detail below. A measurement of the change in $(g-g_o)_z$ and a more precise determination of the D shift for uniaxial pressure would similarly provide all the data necessary.

It would also be interesting to see if the D shift for a third isoelectronic ion, Mn^{4+}, would agree with those of the Cr^{3+} and V^{2+}. An optical pressure experiment on V^{2+} in sapphire could also confirm this agreement. Other EPR experiments which would mutually complement this experiment and that by Walsh[20] would be the two S state

ions, Fe^{3+} and Mn^{2+}, in sapphire and V^{2+} in the cubic MgO. It also comes to mind that resonance shifts with pressure, more practically optical resonances, could be used as a pressure measurement with a potential in accuracy on the order of a per cent or less to pressures of several hundred thousand atmospheres.

Further measurement of the g shift. From the preceding study and previous high pressure EPR experiments[20,22], an expected value of $\Delta(g-g_o)_z/(g-g_o)_z$ would be 1×10^{-3}/katm. Since $(g-g_o)_z$ for ruby is about 0.02, this is a shift in g of 2×10^{-5}/katm. For 10% accuracy a g shift experiment should thus be able to see a Δg of 2×10^{-6}/katm. Since this can be observed over several thousand atmospheres, a reasonable g shift experiment should at least be accurate to one part in 10^5 in the measurements of the g value.

The necessary restrictions for such accuracy can now be determined from the g shift analysis in Chapter IV. The frequency and the field must be measured to about 5×10^{-6}, which requires a factor of two better field measurement. A constant inhomogeneity in the field of 0.1 gauss per inch would be sufficient to permit the suspected motion of 0.030". This is readily obtainable without the bomb, but inhomogeneities inside the bomb would have to be determined. Rotation would have to be held to less than $1/6^o$. The mixing of the change in D with

pressure becomes too large with a misalignment of $\pm$ 3°. Assuming constant line shape, the determination of the center of the 12 gauss wide absorption line requires a signal to noise ratio of about 1000:1. If all of the above requirements can be met, a $\Delta(g-g_o)_z/(g-g_o)_z$ = 1×10^{-3}/katm. could be observed.

APPENDIX A

CRYSTALLINE FIELD FOR SAPPHIRE

The crystalline electric field at the impurity ion site can be calculated by approximating the surrounding ligands by point charges and assuming that there is no overlap of the impurity ion charge and these point charges. (The validity of these assumptions are discussed in the text (Chapter II Part D) and will not be repeated here.) Then the crystalline electric field in this region has a potential which obeys Laplace's equation

$$\nabla^2 V(\underline{r}) = 0 \tag{A1}$$

Therefore, the crystalline field potential can be expanded about the impurity ion site and Laplace's equation has solutions of the form

$$V(\underline{r}) = \sum_{lm} a_{lm} r^l Y_{lm}(\theta, \varphi) \tag{A2}$$

where r, θ, and φ are the spherical coordinates of $\underline{r}$ centered at the impurity ion site and $Y_{lm}(\theta, \varphi)$ are the spherical harmonics. The z axis will be taken as the axis of highest symmetry, the C_3 or three-fold axis in the crystal.

In order to evaluate the coefficient a_{lm}, the potential in equation A2 is equated to the potential at the position $\underline{r}$

$$V(\underline{r}) = \frac{1}{4\pi\epsilon} \sum_i \frac{q_i}{|\underline{r} - \underline{r}_i|} \tag{A3}$$

due to charges, q_i, at the surrounding ion sites, $\underline{r}_i$, whose coordinates are r_i, ϑ_i, and φ_i. From the law of cosines this potential becomes

$$V(\underline{r}) = \frac{1}{4\pi\epsilon} \sum_i q_i / \left[r^2 + r_i^2 - 2\,\underline{r} \cdot \underline{r}_i \right]^{1/2} \tag{A4}$$

which in terms of the Legendre polynomials becomes

$$V(\underline{r}) = \frac{1}{4\pi\epsilon} \sum_i \frac{q_i}{r_i} \sum_{\ell=0}^{\infty} \left(\frac{r}{r_i} \right)^{\ell} P_\ell (\cos \alpha) \tag{A5}$$

where α is the angle between $\underline{r}$ and $\underline{r}_i$. The Legendre polynomials are related to the spherical harmonics by

$$Y_{\ell 0}(\alpha, \beta) = \left(\frac{2\ell+1}{4\pi} \right)^{1/2} P_\ell (\cos \alpha) \tag{A6}$$

so that equation A5 is now

$$V(\underline{r}) = \frac{1}{4\pi\epsilon} \left(\frac{4\pi}{2\ell+1} \right)^{1/2} \sum_i \frac{q_i}{r_i} \sum_{\ell=0}^{\infty} \left(\frac{r}{r_i} \right)^{\ell} Y_{\ell 0}(\alpha, \beta) \tag{A7}$$

The use of the spherical harmonic addition theorem

$$Y_{\ell m}(\alpha, \beta) = \left(\frac{4\pi}{2\ell+1} \right)^{1/2} \sum_m Y^*_{\ell m}(\vartheta_i, \varphi_i)\, Y_{\ell m}(\vartheta, \varphi) \tag{A8}$$

gives for equation A7

$$V(\underline{r}) = \frac{1}{\epsilon} \sum_i \frac{q_i}{r_i} \sum_\ell \frac{1}{(2\ell+1)} \frac{r^\ell}{r_i^\ell} \sum_m Y^*_{\ell m}(\vartheta_i, \varphi_i)\, Y_{\ell m}(\vartheta, \varphi) \tag{A9}$$

Comparison of equations A9 and A2 show that the coefficients $a_{\ell m}$ are

$$a_{\ell m} = \frac{1}{\epsilon(2\ell+1)} \sum_i \frac{q_i}{r_i^{\ell+1}} Y^*_{\ell m}(\theta_i, \varphi_i) \qquad \text{(A10)}$$

where

$$Y^*_{\ell m} = (-1)^m Y_{\ell -m} \qquad \text{(A11)}$$

The expansion in equation A2 with the coefficients in equation A10 can be restricted now due to the symmetry of the impurity ion site and many of the $a_{\ell m}$ vanish. The symmetry of the sapphire lattice at the impurity site is 3 (C_3). This means that the potential is invariant under any of the symmetry operations of the C_3 point group. These are E, C_3, and $2C_3$. Application of the C_3 operation demands that

$$V(r, \theta, \varphi + \tfrac{2\pi}{3}) = V(r, \theta, \varphi) \qquad \text{(A12)}$$

The spherical harmonics, however, obey the relation

$$Y_{\ell m}(\theta, \varphi + \mu) = e^{im\mu} Y_{\ell m}(\theta, \varphi) \qquad \text{(A13)}$$

So that $e^{im\mu}$ is unity, the product $m\mu$ is restricted to integral miltiples of 2π or, since in this case $\mu = 2\pi/3$, values of m to

$$m = 3n \quad ; \quad n = 0, 1, 2, 3, \ldots\ldots \qquad \text{(A14)}$$

The basis functions (equation 3) used to evaluate any matrix elements for the crystalline field potential will consist of 3d wave functions for which 1 = 2. This will lead to integrals of the form

$$\int Y_{2m}^{*} \left(Y_{lm}^{*}\right)_{CF} Y_{2m}\, dV \qquad \text{(A15)}$$

In order for this integral not to vanish 1 is limited to values of 4 or less by the triangle theorem of the spherical harmonics. Also, the parity of the two basis functions are even, their product is even, and therefore the parity of the crystalline field term must be even. This limits 1 to the values 0, 2, and 4.

Thus through symmetry restrictions and the evaluation of matrix elements which do not vanish when the 3d wave functions are used, the crystalline field expansion, equation A2, becomes

$$V(\underline{r}) = a_{00} Y_{00} + a_{20} r^2 Y_{20} + a_{40} r^4 Y_{40} + a_{43} r^4 \left(Y_{43} + Y_{4-3}\right) \qquad \text{(A16)}$$

The a_{00} term will just add a constant to all energy levels and can be eliminated from consideration. The symmetry restrictions of equation A16 are for the orbital angular momentum operators since they enter through position coordinates. The spin operators in the crystalline field term of the spin Hamiltonian, however, must obey the same symmetry restrictions because they enter only through the

spin orbit coupling. It can also be shown that any polynomial in an arbitrary angular momentum operator, J_i, of degree 2J + 1 can be reduced to a polynomial of degree 2J-1, or

$$J_i^{2J+1} \Longrightarrow J_i^{2J-1} + J_i^{2J-2} + \text{----} \quad \text{(A17)}$$

Both Cr^{3+} and V^{2+} have an S = 3/2 so the polynomials of the spin angular momentum operators of the form S_i^4 (or S_i^{2S+1}) allowed by the symmetry restrictions in equation A16 can be expressed as polynomials in S_i^2 (or S_i^{2S-1}). This removes the spin terms which transform like Y_{40} and Y_{43} from consideration.

Thus for a $3d^3$ ion whose S = 3/2 only the term with the coefficient

$$a_{20} = \frac{1}{5\epsilon} \sum_i \frac{q_i}{r_i^3} Y_{20}^*(\theta_i, \varphi_i) \quad \text{(A18)}$$

need be considered. The spherical harmonics in terms of Legendre polynomials are

$$Y_{\ell m}(\theta, \varphi) = (-1)^m \left\{ \frac{2\ell+1}{4\pi} \frac{(\ell-m)!}{(\ell+m)!} \right\}^{1/2} P_\ell^m(\cos\theta)\, e^{im\varphi} \quad \text{(A19)}$$

Substituting this in a_{20} yields the a_{20} given as equation 35 in Chapter II or

$$a_{20} = \frac{1}{\epsilon\sqrt{20\pi}} \sum_i \frac{q_i}{r_i^3} P_{20}(\cos\theta_i) \quad \text{(A20)}$$

where

$$P_{20} = \frac{1}{2}\left(3\cos^2\vartheta_i - 1\right) \tag{A21}$$

It can now be shown that the point charge model can be used to describe the changes in the electrostatic field for an arbitrary ligand charge distribution if the compression is conformal or angle preserving. For an arbitrary ligand charge distribution the coefficients $a_{\ell m}$ in equation A10 becomes

$$a_{\ell m} = \frac{1}{\epsilon(2\ell+1)} \sum_i \int \frac{Y^*_{\ell m}(\Theta, \Phi)}{R^{\ell+1}} \rho_i(R, \Theta, \Phi)\, d\underline{R} \tag{A22}$$

for a distributed ligand charge density ρ_i. (This can be seen by replacing the point charge distribution, qi at (r_i ϑ_i, φ_i), in equation A3 by an arbitrary $\rho_i(\underline{R}) = \rho_i(R,\Theta,\Phi)$ $= q_i \psi^*_{L_i}\psi_{L_i}$ where the ion-ligand and ligand-ligand overlap is zero. The potential becomes $V(\underline{r}) = \frac{1}{4\pi\epsilon}\sum_i \int \frac{\rho_i(\underline{R})}{|\underline{r}-\underline{R}|}\, d\underline{R}$ and results in the coefficients in equation A22 in a completely analogous manner.) For the special angle preserving compression

$$\rho_i'(R', \Theta', \Phi') = \rho_i(R+\Delta R, \Theta, \Phi) \tag{A23}$$

the new coefficients $a_{\ell m}'$ can be expressed in terms of the old by equation A22 as

$$a'_{\ell m} = a_{\ell m} - (\ell+1)\frac{\Delta R}{R} a_{\ell m} \qquad (A24)$$

and

$$\frac{\Delta a_{\ell m}}{a_{\ell m}} = -(\ell+1)\frac{\Delta R}{R} \qquad (A25)$$

Since $\Delta R/R$ is a constant independent of R, this model should accurately preduct any changes due to a conformal compression as in a cubic structure.

APPENDIX B

CHANGE IN CRYSTALLINE FIELD WITH PRESSURE

The change in the crystalline field potential with the application of pressure can be determined from the elastic constants, the lattice constants, and the compressional model derived in Chapter II. The model leads to the following equation (equation 38)

$$\frac{\Delta a_{20}}{a_{20}} = \frac{1}{a_{20}} \sum_i \left(\frac{\partial a_{20}}{\partial x} \Delta x_i + \frac{\partial a_{20}}{\partial z} \Delta z_i \right) \tag{B1}$$

where

$$a_{20} = \frac{1}{e\sqrt{20\pi}} \sum_i \frac{q_i}{r_i^3} P_{20}(\cos \theta_i) \tag{B2}$$

and for $x_k = x, z$

$$\frac{\partial a_{20}}{\partial x_k} = Q \sum_i q_i \left[\frac{-3}{r_i^4} \frac{\partial r_i}{\partial x_k} P_{20}(\cos \theta_i) + \frac{1}{r_i^3} \frac{\partial P_{20}(\cos \theta_i)}{\partial x_k} \right] \tag{B3}$$

and Q is just a combination of constants. The Δx_i and Δz_i for hydrostatic pressure are obtained from equations 25

$$u_1 = \epsilon_{xx} = \frac{\Delta x}{x} = -(s_{11} + s_{12} + s_{13}) p \tag{B4}$$

$$u_3 = \epsilon_{zz} = \frac{\Delta z}{z} = -(2 s_{13} + s_{33}) p$$

by multiplying by the appropriate ion coordinate as follows

$$\Delta x_i = \frac{\Delta x}{x} x_i = u_1 x_i$$
$$\Delta z_i = \frac{\Delta z}{z} z_i = u_3 z_i \quad . \tag{B5}$$

From Table II the values of U_1 and U_3 are

$$u_1 = -0.129 \times 10^{-3} / k \text{ atm.}$$
$$u_3 = -0.146 \times 10^{-3} / k \text{ atm.} \tag{B6}$$

where 1 atmosphere = 1.01325 bars (10^6 dyne/cm.^{2}) = 1.0332 kg/cm.^{2}

The calculations were also performed as a function of uniaxial compression. In all cases considered here the compression was taken along the z axis. For uniaxial compression (see Appendix C) the stresses of equation 24 become

$$p_3 = -p \; ; \; p_1 = p_2 = p_4 = p_5 = p_6 = 0 \quad . \tag{B7}$$

From the matrix multiplication shown as equation 23 the values U_1 and U_3 in terms of the elastic compliance coefficients become

$$u_1 = -s_{13} p$$
$$u_3 = -s_{33} p \quad . \tag{B8}$$

Substituting the compliance coefficients from Table II yield the values

$$\left.\begin{aligned} U_1 &= 0.0395 \times 10^{-3}/\text{katm.} \\ U_3 &= -0.225 \times 10^{-3}/\text{katm.} \end{aligned}\right\} \text{ Uniaxial}$$

The sums in equations B1 and B2 run over the six oxygen and the fourteen nearest aluminum ions. Since many of these ions have the same effect, the sum can be reduced to eight terms with the coordinates for the eight sites listed in Table II. Each term must then be multiplited by a weighting factor, N_i, which is just the number of ions which have those particular coordinates. Also, since the constant Q appears in both the numerator and denominator, it can be dropped. With these simplifications, the substitution of equations B2, B3, and B5 into B1 yields

$$\frac{\Delta a_{20}}{a_{20}} = \sum_{i=1}^{8} N_i q_i \left[u_1 x_i \left(\frac{-3}{r_i^4} \sin\vartheta_i P_{20} + \frac{1}{r_i^3} \frac{\partial P_{20}}{\partial x} \right) + u_3 z_i \left(\frac{-3}{r_i^4} \cos\vartheta_i P_{20} + \frac{1}{r_i^3} \frac{\partial P_{20}}{\partial z} \right) \right] \Bigg/ \sum_{i=1}^{8} \frac{N_i q_i}{r_i^3} P_{20} \qquad \text{(B9)}$$

For calculational purposes the numerator can be simplified using the following relations:

$$x_i = r_i \sin\vartheta_i \qquad z_i = r_i \cos\vartheta_i$$

$$\frac{\partial P_{20}}{\partial x} = \frac{-3\cos^2\vartheta_i \sin\vartheta_i}{r_i} \qquad \text{(B10)}$$

$$\frac{\partial P_{20}}{\partial z} = \frac{3\cos\vartheta_i \sin^2\vartheta_i}{r_i}$$

as shown in the following steps:

$$N_i q_i \left[u_1 x_i \left(\frac{-3}{r_i^4} \sin\theta_i P_{20} + \frac{1}{r_i^3} \frac{\partial P_{20}}{\partial x} \right) + u_3 z_i \left(\frac{-3}{r_i^4} \cos\theta_i P_{20} + \frac{1}{r_i^3} \frac{\partial P_{20}}{\partial z} \right) \right] ;$$

$$\frac{N_i q_i}{r_i^3} \left[u_1 x_i \left(\frac{-3}{r_i} \sin\theta_i P_{20} + \frac{-3\cos^2\theta_i \sin\theta_i}{r_i} \right) + u_3 z_i \left(\frac{-3}{r_i} \cos\theta_i P_{20} + \frac{3\cos\theta_i \sin^2\theta_i}{r_i} \right) \right] ;$$

$$\frac{-3N_i q_i}{r_i^3} \left[u_1 \left(\sin^2\theta_i P_{20} + \cos^2\theta_i \sin^2\theta_i \right) + u_3 \left(\cos^2\theta_i P_{20} - \cos^2\theta_i \sin^2\theta_i \right) \right] ;$$

$$\frac{-3N_i q_i}{r_i^3} \left[u_1 \sin^2\theta_i \left(P_{20} + \cos^2\theta_i \right) + u_3 \cos^2\theta_i \left(P_{20} - \sin^2\theta_i \right) \right] .$$

Equation B10 is now

$$\frac{\Delta a_{20}}{a_{20}} = \frac{\sum_{i=1}^{8} \frac{-3N_i q_i}{r_i^3} \left[u_1 \sin^2\theta_i \left(P_{20} + \cos^2\theta_i \right) + u_3 \cos^2\theta_i \left(P_{20} - \sin^2\theta_i \right) \right]}{\sum_{i=1}^{8} \frac{N_i q_i}{r_i^3} P_{20}} \qquad \text{(B11)}$$

where $P_{20} = \frac{1}{2}(3\cos^2 - 1)$. This is the equation that was used to numerically calculate the values in Table III.

The change in the crystalline field potential with both hydrostatic and uniaxial pressure was also done as a function of position along the z axis. To do this the values of z_i were obtained from the constants r_i and $\cos\theta_i$ in Table I. For example, z_i for the oxygen site 01 is

$z_1 = r_1 \cos\phi_1 = (1.95\,\text{Å})(0.436) = 0.806\,\text{Å}$

If the impurity ion substitutes 0.1 Å toward the empty octahedral site along the z axis, this value will be lower by 0.1 Å or .706 Å since the motion is toward the plane of these ions (i.e., up in Figure 6). With the new values z_i the constants of Table II were redetermined assuming no change in x_i. The calculations for hydrostatic and uniaxial pressure were then performed again. As indicated in Table III, this was done for the non-substitutional positions of -0.1Å, 0.1Å, 0.12Å, and 0.15Å where the positive number indicates a position closer to the empty octahedral site.

It was seen early in the calculational process that the contribution of the fourteen aluminums was usually quite small. Therefore, their contribution was neglected in some of the calculations as shown in Table III. In the remaining values the aluminum contribution and the oxygen contribution were calculated separately. The table then shows the values for only the oxygens and for the combined effect of the oxygens and the aluminums.

All the numerical calculations were checked by Miss P. Van Alstine by an independent determination.

APPENDIX C

ELASTIC CONSTANTS

In order to be able to use the elastic constants properly, it is necessary to understand their origin and meaning. Since the elastic constants are relations between stress and strain, these will first be discussed in sections A and B. After the elastic constants and their special notation are discussed in section C, the special form that they take for isotropic or "Engineering" materials is indicated in section D. Techniques of measurement are briefly reviewed in section E.

A. THE STRESS TENSOR

Two assumptions are first necessary to describe the "stress" or combination of forces applied to a deformable body. First, all parts of the body are in equilibrium. Since the interaction forces in a body are molecular and therefore very short range, the second assumption is that the forces acting on any part of the body by surrounding parts act only on its surface. (This does not hold when macroscopic fields are produced such as in the piezoelectric effect.)

Consider the forces acting in or upon the small differential cube in Figure C1. By the second assumption these forces can be resolved into the forces, σ_{ij} , acting on the faces of the cube. σ_{ij} can be interpreted as the force in the i direction acting on the surface, S_j whose normal is in the j direction. If $i = j$, it is a "normal" force, and if $i \neq j$, it is a "shear" force. By convention a positive σ_{ii} is a tensile force and negative a compressive force. It can be shown[73] that the σ_{ij} are symmetric. This can be easily seen from Figure C1 and the first assumption. Since the portion of the body represented by the cube must be in equilibrium, its moments about any axis must be zero. For example, the moments about the x_1 axis are $-\sigma_{23}$ and σ_{32} whose sum must equal zero. Therefore $\sigma_{23} = \sigma_{32}$ and similarly $\sigma_{ij} = \sigma_{ji}$.

From the second assumption, the sum of the forces on the surface of the cube, $\oint \sigma_{ij}\, dS_j$, is equivalent to the sum of the forces within the cube, $\int F_i\, dV$, where F_i is the vector force per unit volume on the arbitrarily small volume element dV . From vector analysis the two can only be equal if F_i is the divergence of σ_{ij} or

$$F_i = \frac{\partial \sigma_{ij}}{\partial x_j} \qquad \text{(C1)}$$

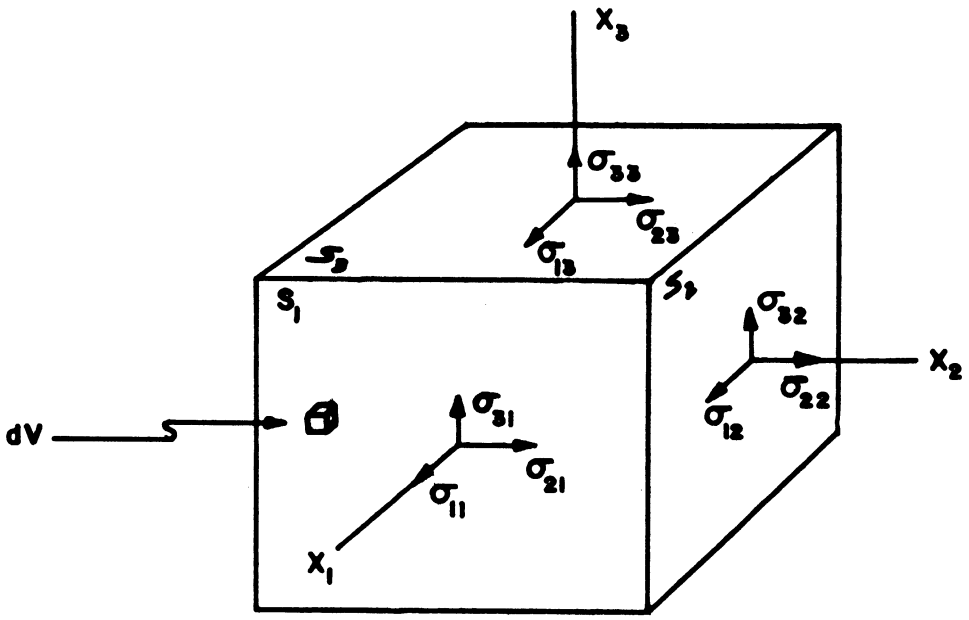

Figure C1. Stress components.

Since F_i is a vector, then σ_{ij} must be a tensor of rank two. Also, the equation of equilibrium for a deformable body is then

$$\frac{\partial \sigma_{ij}}{\partial x_j} = 0 \quad . \tag{C2}$$

Because it is a tensor, it can be transformed to its principle axes so that only diagonal elements exist. Some examples for uniaxial, hydrostatic, and pure shear stresses are shown below.

$$\begin{pmatrix} \sigma & 0 & 0 \\ 0 & 0 & 0 \\ 0 & 0 & 0 \end{pmatrix} \qquad \begin{pmatrix} -p & 0 & 0 \\ 0 & -p & 0 \\ 0 & 0 & -p \end{pmatrix}$$

Uniaxial Tension Hydrostatic Pressure

$$\begin{pmatrix} -\sigma & 0 & 0 \\ 0 & \sigma & 0 \\ 0 & 0 & 0 \end{pmatrix} = \begin{pmatrix} 0 & \sigma & 0 \\ \sigma & 0 & 0 \\ 0 & 0 & 0 \end{pmatrix}$$

Pure Shear

It must be emphasized that the stress tensor is not a "matter" or crystal property tensor such as permittivity or magnetic susceptibility. It is "field" tensor and can have any arbitrary direction for its principle axes and can exist for isotropic and amorphous bodies such as glass.

B. THE STRAIN TENSOR

Since it is not as simple to picture strain geometrically it is easiest to understand by starting with one dimension and generalize to two and later three dimensions. A stretchable one dimensional string is pictured in Figure C2a. Consider point P a distance x from the origin and a nearby point Q at $x+\Delta x$. After stretching, P is at P' a distance $x+u$ from the origin, and Q is at Q' a distance $\Delta x+\Delta u$ from P'. Since strain is an indication only in change of length, the transition from the origin is of no concern, and strain can be defined as the increase in length over the original length. Therefore

$$\text{strain} \equiv \frac{\text{increase in length}}{\text{original length}} = \frac{P'Q' - PQ}{PQ} = \frac{\Delta u}{\Delta x} \quad \text{(C3)}$$

More precisely, the strain at the point P is

$$e = \lim_{\Delta x \to 0} \frac{\Delta u}{\Delta x} = \frac{du}{dx} \quad . \quad \text{(C4)}$$

If $\frac{du}{dx}$ is a constant for all x, then it is said to be "homogeneous" strain. Only homogeneous strain will be considered from here on. (For inhomogeneous strain see, for example, Reference 74.)

In two dimensions the string becomes the stretchable sheet pictured in Figure C2b. There are now four e's where

a.)

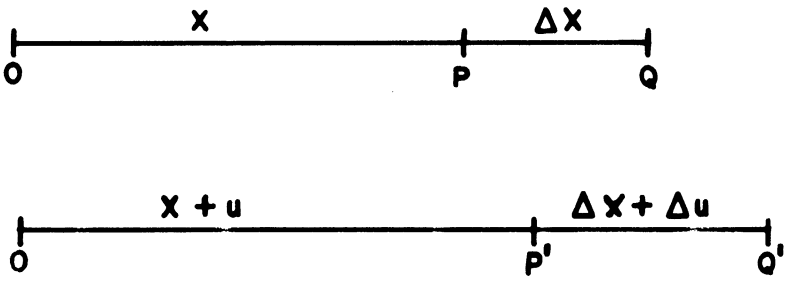

ONE DIMENSIONAL STRAIN

b.)

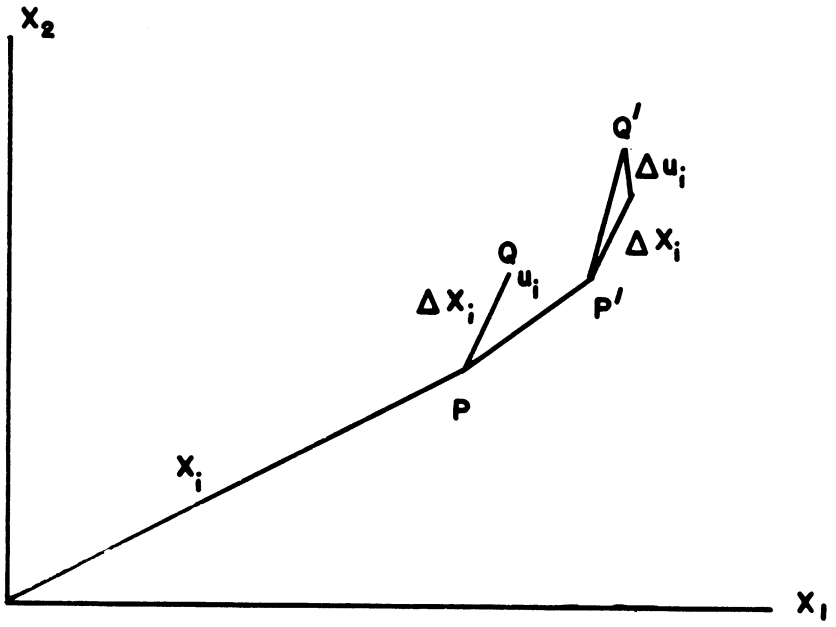

TWO DIMENSIONAL STRAIN

Figure C2. One and two dimensional strain.

$$e_{ij} = \frac{\partial u_i}{\partial x_j} \quad ; \quad (i,j = 1,2) \qquad \text{(C5)}$$

Geometrically the change Δu_i would be

$$\Delta u_i = \frac{\partial u_i}{\partial x_j} \Delta x_j = e_{ij} \Delta x_j \qquad \text{(C6)}$$

Since Δu_i and Δx_j are vectors, e_{ij} is a tensor of rank 2.

The special case of Δx_i parallel to an axis, say x_1, is helpful to understand the meaning of e_{ij}, and is shown in Figure C3a. The point Q_1' will now not only have a component of linear extension, Δu_1, along the axis as in the one dimensional case but shift off the axis by Δu_2 as well. Thus

$$\frac{\Delta u_1}{\Delta x_1} = \frac{\partial u_1}{\partial x_1} = e_{11} \qquad \text{(C7)}$$

and e_{11} is the linear or extension component. Also from Figure C3a and from the fact that only small changes are considered

$$\text{TAN}\,\vartheta = \frac{\Delta u_2}{\Delta x_1 + \Delta u_1} \cong \frac{\Delta u_2}{\Delta x_1} \cong \vartheta \cong \frac{\partial u_2}{\partial x_1} = e_{21} \qquad \text{(C8)}$$

and e_{21} is the rotational component.

Now if e_{ij} is purely a strain tensor, then a transformation which allows no deformation should have all $e_{ij} = 0$. But a pure rotation of an angle φ shown in Figure C3b has no deformation but

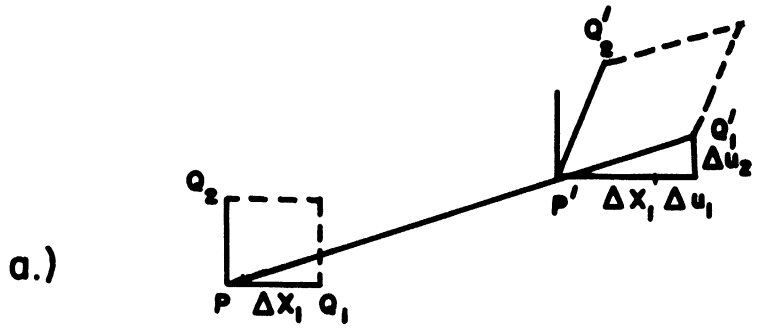

PURE SHEAR

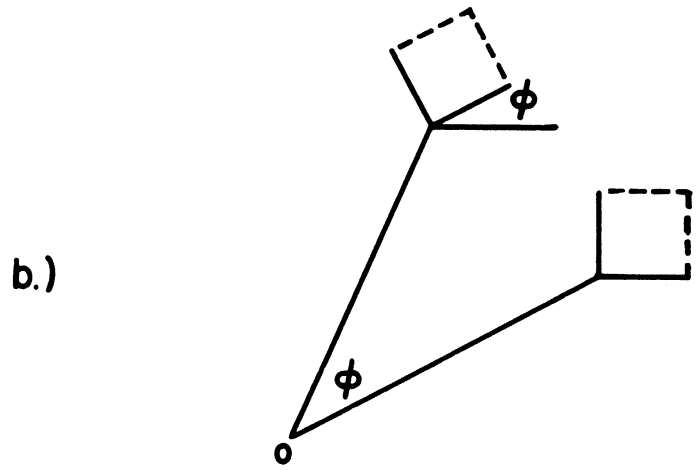

ROTATION

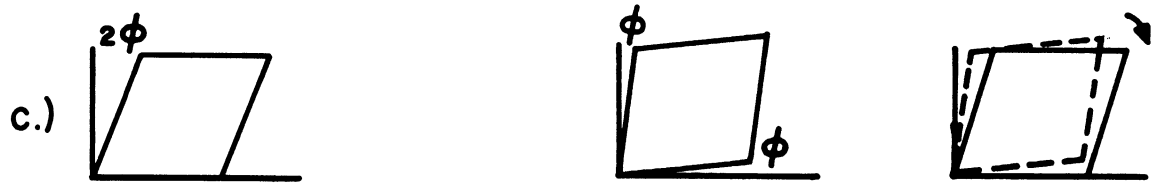

SIMPLE SHEAR = PURE SHEAR + ROTATION

Figure C3. Examples of specialized strains.

$$e_{ij} = \begin{pmatrix} 0 & -\varphi \\ \varphi & 0 \end{pmatrix} \quad . \tag{C9}$$

This rotation is antisymmetric and it can be proven in general that a pure rotation is always antisymmetric as follows:

Choose the origin as the axis of rotation and the Δu_i will always be perpendicular to Δx_i and

$$\Delta u_i \, \Delta x_i = 0 \quad . \tag{C10}$$

Substitution from equation C6 gives

$$e_{ij} \, \Delta x_j \, \Delta x_i = 0 \tag{C11}$$

or

$$\begin{aligned} e_{ij} &= 0 \qquad i = j \\ e_{ij} &= -e_{ji} \qquad i \neq j \end{aligned} \quad . \tag{C12}$$

The conditions (C12) are exactly those of an antisymmetric tensor. Since any tensor can be defined as the sum of a symmetric tensor and an antisymmetric tensor, e_{ij} can be defined as

$$e_{ij} = \epsilon_{ij} + \omega_{ij} = \tfrac{1}{2}\left(e_{ij} + e_{ji}\right) + \tfrac{1}{2}\left(e_{ij} - e_{ji}\right) \quad . \tag{C13}$$

ϵ_{ij} is the symmetric part of the strain tensor and is commonly called just the strain tensor. ϵ_{ii} is the same as e_{ii} but ϵ_{12} is now $\frac{1}{2}(e_{12} + e_{21})$ and equivalent to $\frac{1}{2}$ the change in angle between two axes. A simple example of this separation is shown in Figure C3c where a "simple" shear is equivalent to the sum of a "pure" shear and a rotation.

Extension to three dimensions is completely general and easily done by simply letting i and j run over 1, 2, 3. Again it must be emphasized that the strain tensor will only conform to matter or crystal properties when the causing stress does.

C. ELASTIC CONSTANTS AND MATRIX NOTATION

Experimentally it has been known for a long time that a stress will produce a strain and that below the elastic limit, where irreversible changes start to occur, the two are proportional. This is Hooke's Law and is written

$$\epsilon = s\sigma \tag{C14}$$

where s is a constant. The higher the value of s, the larger the strain produced for a given stress or the more compliant the material. The s is thus called "elastic compliance" or just compliance. Equation C14 is also written

$$\sigma = C\,\epsilon \tag{C15}$$

where now the higher the value of C, the less the strain or the stiffer the material. The C is therefore called "elastic stiffness" or just stiffness. These equations are generalized in tensor notation to

$$\epsilon_{ij} = s_{ijkl}\,\sigma_{kl} \tag{C16}$$

and similarly

$$\sigma_{ij} = c_{ijkl}\,\epsilon_{kl} \tag{C17}$$

where the indices range over 1, 2, 3 and the s and c now have 81 components. It can be proven that s_{ijkl} and c_{ijkl} are tensors of fourth rank.[60] Because σ_{ij} and ϵ_{ij} are symmetric, not all of the 81 components are independent. For example, if we apply shear stress σ_{21}, there must also be σ_{12} and

$$\epsilon_{ij} = s_{ij12}\,\sigma_{12} + s_{ij21}\,\sigma_{21} = \left(s_{ij12} + s_{ij21}\right)\sigma_{12} \quad . \tag{C18}$$

It is impossible to devise an experiment to separate s_{ij12} from s_{ij21}, therefore, an arbitrary constant can be used to relate them; the easiest being equality, or

$$s_{ijkl} = s_{ijlk} \tag{C19}$$

In a similar argument, a uniaxial stress along say the x_3 axis will produce the strains

$$\epsilon_{ij} = s_{ij33}\,\sigma_{33} \quad \text{AND} \quad \epsilon_{ji} = s_{ji33}\,\sigma_{33} \tag{C20}$$

But since $\epsilon_{ij} = \epsilon_{ji}$ we can write

$$s_{ijkl} = s_{jikl} \tag{C21}$$

Thus the independent number of components is reduced to 36.

Now a change in notation is necessary before the elastic constants given in the literature are obtained. Since there are six independent components in each of the stress and strain tensors, the double indices are reduced to a single index ranging from 1 to 6, as follows:

Matrix Notation	1	2	3	4	5	6	(C22)
Tensor notation	11	22	33	(23,32)	(31,13)	(12,21)	

or in the tensor arrays:

$$\begin{pmatrix} \sigma_{11} & \sigma_{12} & \sigma_{13} \\ & \sigma_{22} & \sigma_{23} \\ \text{SYM.} & & \sigma_{33} \end{pmatrix} \longrightarrow \begin{pmatrix} \sigma_1 & \sigma_6 & \sigma_5 \\ & \sigma_2 & \sigma_4 \\ \text{SYM.} & & \sigma_3 \end{pmatrix} \longrightarrow \begin{pmatrix} p_1 \\ p_2 \\ p_3 \\ p_4 \\ p_5 \\ p_6 \end{pmatrix}$$

and similarly the ϵ_{ij} becomes u_i . Thus we now have the equations used in actual practice

$$u_i = s_{ij} p_j \tag{C23}$$

and

$$p_i = c_{ij} u_j \tag{C24}$$

For example; hydrostatic pressure would be $p_1 = p_2 = p_3 = -p$ and $p_4 = p_5 = p_6 = 0$; uniaxial tension is $p_1 = p$ and $p_{2,6} = 0$; pure shear is $p_1 = -p_2$ and $p_{3,6} = 0$ or $p_{1,5} = 0$ and $p_6 = p$. Since the arrays s_{ij} and c_{ij} are selected components of their respective fourth rank tensors, they are not tensors of rank two and do not transform like one. If it is desired to transform to a new set of axes, it is necessary to return to the four index notation. However, the arrays are still symmetric and only 21 independent components exist for an anisotropic material with no symmetry.

Crystal symmetry will reduce the number of constants still further. For example, in the $\bar{4}$ class with the $\bar{4}$ (S_4) axis parallel to x_3 the axes transform as follows:

$$1 \rightarrow 2 \; ; \quad 2 \rightarrow -1 \; ; \quad 3 \rightarrow -3$$

Therefore, in the tensor notation

$11 \rightarrow 22\ ;\ 22 \rightarrow 11\ ;\ 33 \rightarrow 33\ ;\ 23 \rightarrow 13\ ;\ 31 \rightarrow -32\ ;\ 12 \rightarrow -21$

or in matrix notation

$1 \rightarrow 2\ ;\ 2 \rightarrow 1\ ;\ 3 \rightarrow 3\ ;\ 4 \rightarrow 5\ ;\ 5 \rightarrow -4\ ;\ 6 \rightarrow -6\ .$

The array of indices becomes in the matrix notation

$$\begin{pmatrix} 22 & 21 & 23 & 25 & -24 & -26 \\ & 11 & 13 & 15 & -14 & -16 \\ & & 33 & 35 & -34 & -36 \\ & & & 55 & -54 & -56 \\ & \text{SYMMETRIC} & & & 44 & 46 \\ & & & & & 66 \end{pmatrix}$$

and when equated with the original, results in the following relations between constants for this particular class:

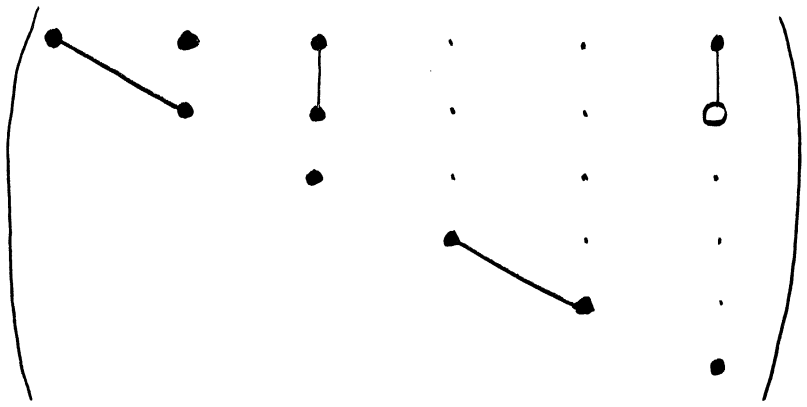

This is a common means of displaying these relations (Reference 60, p. 140) and a heavy dot implies a non-zero value, a line adjoining two dots is equivalence, and a circle is negative equivalence. Further examples would be triclinic, which is simply 21 dots and cubic, which is

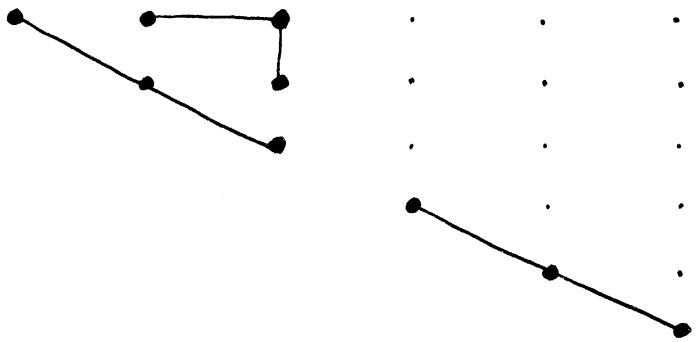

D. ISOTROPIC STRESS STRAIN RELATIONS

For isotropic materials the constants are reduced to two. Its relations are like cubic above except $S_{44} = 2(S_{11} - S_{12})$. The constant relating pure tensile stress and pure extensive strain is called "Young's Modulus", E, where

$$E = \frac{1}{S_{11}} \tag{C25}$$

and can be thought of as a coefficient of extension. The ratio of transverse compression to longitudinal extension is

$$\nu = -\frac{S_{12}}{S_{11}} \tag{C26}$$

and is called "Poisson's Ratio", ν . Substitution into equation C23 gives, for example,

$$u_1 = \frac{1}{E}\left\{P_1 - \nu(P_2 + P_3)\right\} \quad . \tag{C27}$$

The "Rigidity Modulus", G , comes from the shear components of equation C23, or

$$u_4 = 2(S_{11} - S_{12})P_4 = \frac{1}{G}P_4 \tag{C28}$$

or

$$G = \frac{1}{2(S_{11} - S_{12})} \tag{C29}$$

and can be thought of as a resistance to shear.

The volume change or "dilation", Δ, is

$$(1+u_1)(1+u_2)(1+u_3) - 1 = \Delta \tag{C30}$$

which for small strains becomes

$$\Delta = u_1 + u_2 + u_3 \quad . \tag{C31}$$

For hydrostatic pressure where $P_1 = P_2 = P_3 = -P$ and $P_{4,6} = 0$, $-\Delta / P$ just becomes the sum of the nine components in the upper left-hand corner of the S_{ij} matrix and for cubic and isotropic is

$$-\frac{\Delta}{P} = 3(S_{11} + 2S_{12}) = \frac{1}{K} \qquad \text{(C32)}$$

where K is the "Bulk modulus".

E. MEASUREMENTS

If the medium is now subjected to an elastic wave, equation C2 has an additional term so that the balance of forces is still maintained and the equation of equilibrium becomes

$$\rho \frac{\partial^2 \epsilon_{ij}}{\partial t^2} = \frac{\partial \sigma_{ij}}{\partial x_j} \qquad \text{(C33)}$$

where ρ is the density and the left-hand side is a mass times acceleration. Since the σ_{ij}'s can be related to the ϵ_{ij}'s (Reference 73, p. 98), equation C33 can be reduced to a set of equations of the form

$$\frac{\partial^2 u_i}{\partial x_j^2} - \frac{1}{c_j^2} \frac{\partial^2 u_i}{\partial t^2} = 0 \qquad \text{(C34)}$$

which is now in matrix notation and c_j contains only combinations of the elastic constants and is the "velocity of sound" in the material in the j direction.

Most measurements of the elastic constants use some form of equation C34 and a determination of the elastic wave velocities in various directions.[47,75-77] There are two principle methods of this type of measurements, pulse echo

and resonance, both of which measure the adiabatic constants. The pulse echo method utilizes a determination of the time delay for a single pulse to echo a given number of times in a crystal of known length. The resonance technique involves a variation of input frequency to a crystal and observation of resonances for a known length in the crystal.

Static methods are simpler in theory but more difficult in practice and measure the isothermal constants.[78] This method just measures a known strain for a known stress. The isothermal constants, however, can be obtained from the adiabatic ones by the relation

$$[s_{ij}]_S - [s_{ij}]_T = - \frac{\alpha_i \alpha_j T}{\rho C_\rho} \qquad \text{(C35)}$$

Where α_i is the change in strain, u_i, with temperature and C_ρ the heat capacity at constant stress. These differences are usually quite small.

APPENDIX D

DATA REDUCTION

A. CHROMIUM IMPURITY

For the Cr^{3+} ion the data obtained from the experimental procedure were the pressure, the microwave frequency, and the magnetic field measurements at the two resonant conditions for the two samples. The frequency measurement is direct in gigacycles from a calibrated absorption type frequency meter (See Chapter III). The field measurements were in "proton" kilocycles (kcP) for a proton nuclear resonance condition and were converted directly into pressure shifts as will be shown later.

The pressure readings were in 0.01 ohms resistance to balance the bridge circuit including the manganin wire whose resistance changes with pressure. By judicious choice of bridge components this reading was almost equivalent to atmospheres pressure. Calibration of the pressure system by observing the freezing point of mercury showed a correction to the resistance reading as

$$P(\text{atm.}) = 0.904\, R(0.01\ \text{OHMS}) - 60. \tag{D1}$$

For the determination of any shifts in the g_z value the equation

$$\Delta g_z = - g_z \frac{\Delta H}{H'} \qquad \text{(D2)}$$

is used. The value of g_z is obtained from Schulz-DuBois[37] and is

$$g_z = 1.9840 \pm .0006 \qquad \text{(D3)}$$

The ratio $\Delta H/H'$ needs no conversion of units and "proton" kilocycles/sec. can be used directly.

In the g shift determinations there often remained a field difference when both samples were at atmospheric pressure. This zero pressure difference which is subtracted from high pressure differences must be corrected for the frequency changes in the cavity. Consider the following diagrams:

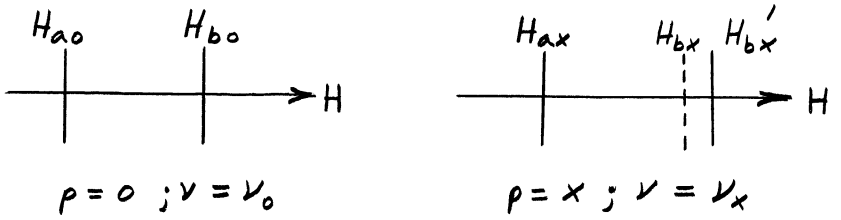

$\rho = 0 \; ; \nu = \nu_0$ $\qquad$ $\rho = x \; ; \nu = \nu_x$ $\qquad$ (D3)

When no pressure is applied the resonance field condition for the high pressure sample, H_{bo}, is different from that for the reference sample, H_{ao}. Applying pressure to the system changes the frequency so that these two new resonant conditions are

$$H_{bx} = \frac{\nu_x}{\nu_o} H_{bo}$$

$$H_{ax} = \frac{\nu_x}{\nu_o} H_{ao} \qquad \text{(D4)}$$

because

$$h\nu = g_z \beta H \qquad \text{(D5)}$$

In addition, the high pressure samples resonant field value is shifted because of a change in the spin Hamiltonian parameter to the value H^0_{bx}. The value that is desired

$$\Delta H = H_{bx}' - H_{bx} \qquad \text{(D6)}$$

thus becomes in terms of the measured parameters

$$\Delta H = H_{bx}' - H_{bx} = H_{bx}' - (H_{ax} + H_{bx} - H_{ax})$$

$$\Delta H = H_{bx}' - \left\{H_{ax} + \frac{\nu_x}{\nu_o}(H_{bo} - H_{ao})\right\} \qquad \text{(D7)}$$

This equation and equation D2 were used to evaluate shifts in g_z with pressure.

The shift in the spin Hamiltonian parameter, 2D, was evaluated from experimental data by the equation

$$\Delta 2D = -g_z \beta \Delta H \qquad \text{(D8)}$$

The value g_z is the unshifted value of equation D3 and β is the Bohr magneton

$$\beta = 9.2732 \times 10^{-21} \text{ erg/gauss} . \tag{D9}$$

Converting the ergs to megacycles and the gauss to "proton" kilocycles/sec. with $\gamma_p/2\pi$ =4.25770 kcP/gauss yields

$$\beta = 0.32872 \text{ Mc/sec. kcP} \tag{D10}$$

and equation D8 is

$$\Delta 2D = -0.65234 (\text{Mc/sec. kcP}) \Delta H (\text{kcP}). \tag{D11}$$

Since for these data runs there was n egligible or no zero pressure field difference, this was the equation used to evaluate the data.

The values obtained were fit by the least squares method to the equation

$$y_i = a + b x_i \tag{D12}$$

where y_i is the parameter $\Delta 2D$; x_i, which has essentially no error ($\pm$ 1 atm. in thousands), is the pressure; and a and b are

$$b = \frac{\bar{x}\,\bar{y} - \overline{xy}}{(\bar{x}^2) - \overline{x^2}}$$

$$a = \bar{y} - b\bar{x} \tag{D13}$$

The standard error of the fit is the root-mean-square of the y derivations

$$s_y = \left(\sum_{i=1}^{n} d_i^2 / n \right)^{1/2} \qquad \text{(D14)}$$

For the check of the pressure shift in 2D when the magnetic field was not parallel to the crystalline field axis, equations 17 and 18 (Chapter II) were used. These equations involve the values x and y where

$$x = g_z \beta H / (-D)$$

$$y_M - y_{M-1} = \frac{E_M}{-D} - \frac{E_{M-1}}{-D} = \frac{h\nu_{M \to M-1}}{-D} \qquad \text{(D15)}$$

The values of g_z and β from equations D2 and D10 were used with the measured frequency and magnetic field values and the D(P) obtained from the zero angle determination. A check for equality to three significant figures in the pressure shift was then determined.

B. VANADIUM IMPURITY

The same data was obtained for the V^{2+} ion as for the Cr^{3+} ion except that it was only for the high pressure sample. Also, the resonant magnetic field conditions for the first (in increasing field) three hyperfine lines were obtained for each pressure. This allowed two separate

determinations of the two spin Hamiltonian parameters involved, D and A (See Chapter IV). Because there was no two sample comparison in this case, equation 14 was used directly and is shown below where the second order hyperfine correction is simplified to $f(B,A,g_z, D,H,m)$ and the transition M = $+\frac{1}{2}$ to +3/2 is used;

$$h\nu = g_z \beta H + 2D + Am + f \quad . \tag{D16}$$

The frequency, the pressure, and the magnetic field were measured as before; however, the field probe contained heavy water and the deuteron resonance was used. Therefore, "deuteron" kilocycles/sec. were measured and with $\gamma_D / 2\pi$ = 0.65356 kcD/gauss the value for β becomes

$$\beta = 2.1415 \text{ Mc/sec. kcD} \quad . \tag{D17}$$

Since for V^{2+} in Al_2O_3 the values $g_z \beta H$ and 2D are of the same order of magnitude, the second order correction, f, is quite significant as can be seen from equation 14. An iterative process was used to determine the pressure dependence of this correction. From the first part of this experiment and previous high pressure EPR experiments, the shift in D with pressure was expected to be much larger than that in A and g_z. (The change in B was assumed to be the same as A.) Thus to first order in

pressure shifts g_z, A, and f were assumed constant and the change in D with pressure was calculated from equation D16 as

$$\Delta 2D = h\nu' - h\nu + g_z \beta H - g_z \beta H' \tag{D18}$$

where the primes indicate pressure. This was done for each of the three hyperfine lines at a given pressure. From the pressure dependence of $D = D(P)$ the pressure dependence of the second order correction, $f^0(\ldots,D^0,\ldots)$ was calculated. This was at most a 2% change in a term which was at most a 0.4% correction. However, this was used to attempt to detect shifts in A.

For a given pressure the resonant field conditions for two hyperfine lines are

$$h\nu_m' = g_z \beta H_m' + 2D' + mA' + f'(m) \tag{D19}$$

and

$$h\nu_{m+1}' = g_z \beta H_{m+1}' + 2D' + (m+1)A' + f'(m+1)$$

Subtracting the former from the latter yields

$$A' = h(\nu_{m+1}' - \nu_m') + g_z \beta (H_m' - H_{m+1}') + f'(m) - f'(m+1) . \tag{D20}$$

(Note: In this iterative process it is impossible to calculate a $\Delta A = A^0 - A$ analogous to equation D18. Since it would take form

$$A' - A = \frac{1}{m}\left\{\left(h\nu' - g_z\beta H' - f' - 2D'\right) - \left(h\nu - g_z\beta H - 2D - f\right)\right\} \quad \text{(D21)}$$

where the D^0 and f^0 were calculated from the same data (ν^0, H^0, ν, and H) assuming a constant **A**, it will just return a constant **A**.)

Evaluation of equation D20 between two independent pairs of hyperfine lines for each pressure indicated no shift in **A** outside of the experimental error. Thus, **A** was assumed constant, and the calculation of equation D18 was redone using a pressure corrected second order hyperfine correction, f^0, or

$$\Delta 2D = \left(h\nu' - g_z\beta H' - f'\right) - \left(h\nu - g_z\beta H - f\right) \quad \text{(D22)}$$

This then yielded the results for the pressure dependence of the crystalline field term in the spin Hamiltonian.

APPENDIX E

EQUIPMENT

The following is a list of the commercial electronic equipment used in the experiment and shown in the schematic in Figure 9. The high pressure generating equipment was manufactured by Harwood Engineering. The pressure bomb and cavity were fabricated under the direction of Mr. Herman Roemer in the University of Michigan Physics Department's Instrument Shop. All other components except standard waveguide were constructed in the laboratory.

A. SPECTROMETER
- Klystron - Varian V153C
- Wavemeter - Hewlett Packard X532A
- Isolator - Kearfott 177-2c-1
- 20 db Attenuator - Hewlett Packard X375A
- Phase Shifter - Hewlett Packard X885A
- 50 db Attenuator - FXR - X164A
- Detector - Microwave Associates IN23E
- Power Supply, Preamp, and AFC - Varian V4500-10
- Signal Generator - Heathkit AG8
- Modulation Amplifier - Heathkit AA121
- Recorders - Varian G10

B. MAGNET
- Varian 3400 9"D. - $3\frac{1}{4}$" gap rotable magnet with Varian V2503 - 7 kva power supply

C. PRESSURE MEASUREMENT
- Galvanometer - Leeds and Northrup 2430D
- Decade Resistance - General Radio 1432U

APPENDIX F

RACAH PARAMETERS AND SYMMETRY TABLES

The Racah parameters arise from the two electron matrix elements of the interelectron Coulomb repulsion integral, i.e., matrix elements of the last term in $\mathcal{H}_0$, and are all of the form

$$\langle \phi_i^* \phi_j^* \left| \frac{e^2}{r_{12}} \right| \phi_m \phi_t \rangle \qquad \text{(F1)}$$

(With i = m and j = t this is just a Coulomb integral, J, or with i = t and j = m an exchange integral, K.)
The potential is expanded as

$$\frac{e^2}{r_{12}} = \frac{e^2}{(r_1^2 + r_2^2 - 2 r_1 r_2 \cos\omega)^{1/2}} = \frac{e^2}{r_>}\left(1 + \frac{r_<^2}{r_>^2} - 2\frac{r_<}{r_>}\cos\omega\right)^{-1/2}$$

$$= \frac{e^2}{r_>} \sum_{k=0}^{\infty} \frac{r_<^k}{r_>^k} P_k(\cos\omega) \qquad \text{(F2)}$$

where $r_<$ and $r_>$ are the lesser and greater of the two electron coordinates r_1 and r_2. The integral can now be done over the angular part of the wave functions leaving

$$\langle \phi_i^* \phi_j^* \left| \frac{e^2}{r_{12}} \right| \phi_m \phi_t \rangle = \sum_{k=0}^{\infty} \langle R_{n\ell}^i R_{n\ell}^j \left| \frac{e^2 r_<^k}{r_>^{k+1}} \right| R_{n\ell}^m R_{n\ell}^t \rangle \, a_k \qquad \text{(F3)}$$

where the angular integration is lumped in the constant, a_k.

One defines now Slater Condon parameters

$$F^k(i_{n\ell}, j_{n\ell}) = \langle R^i_{n\ell} R^j_{n\ell} \left| \frac{e^2 r_<^k}{r_>^{k+1}} \right| R^i_{n\ell} R^j_{n\ell} \rangle \qquad \text{(F4)}$$

$$G^k(i_{n\ell}, j_{n\ell}) = \langle R^j_{n\ell} R^i_{n\ell} \left| \frac{e^2 r_<^k}{r_>^{k+1}} \right| R^i_{n\ell} R^j_{n\ell} \rangle \qquad \text{(F5)}$$

(It is easy to see that $J = \sum_{k=0}^{\infty} a_k F^k$ and $K = \sum_{k=0}^{\infty} a_k G^k$.)
A common denominator $1/d_k^2$ exists in the a_k and is usually lumped with F^k for a new $F_k = \frac{1}{d_k^2} F^k$. The sum is cut off at $k = 2\ell$ because of the angular part and for d electrons Racah introduced the three linear combinations of F_k as basic parameters:

$$\begin{aligned} A &= F_0 - 49 F_4 \\ B &= F_2 - 5 F_4 \\ C &= 35 F_4 \end{aligned} \qquad \text{(F6)}$$

The first order electrostatic energies are linear combinations of these parameters. In particular for $3d^3$ free ions they are

$$\begin{aligned} {}^4F &= 3A - 15B \\ {}^4P &= 3A \\ {}^2H &= {}^2P = 3A - 6B + 3C \end{aligned} \qquad \text{(F7)}$$

$$^2G = 3A - 11B + 3C$$

$$^2F = 3A + 9B + 3C$$

$$^2D = 3A + 5B + 5C \pm (193B^2 + 8BC + 4C^2)^{1/2}.$$

Note that A enters the same in all levels and is usually just dropped. B and C for a given ion are thus not independent but connected by a ratio C/B.

In a crystalline field these levels will be split and related by a function of the field and these parameters. Thus by observing transitions between levels of the same electronic origin, one determines the field splitting. Combining this with transitions between levels of different electronic origin, one determines the Racah parameters. It is in this manner that Drickamer[34] determined the change in B with pressure.
For example, for Cr^{3+} in sapphire[55]

$$h\nu_{T_2} = E\left[^4A_2(F) \rightarrow {}^4T_2(F)\right] = -2Dq - 15B - (-12Dq - 15B) = 10Dq$$

$$h\nu_{T_1} = E\left[^4A_2(F) \rightarrow {}^4T_1(F)\right] = 3Dq - \tfrac{15}{2}B \pm \left[(15B - 10Dq)^2 + 120BDq\right]^{1/2} \quad \text{(F8)}$$

From the frequency dependence of the $^4T_2$ - $^4A_2$ transition he determined the pressure dependence of Dq. From this and the pressure dependence of the $^4T_1$ - $^4A_2$ transition he calculated the pressure dependence of B.

That B decreases with increasing covalency as indicated in Chapter II-E can be seen as follows. B is made of integrals of the following form[55]

$$\int R_i^*(r) R_j^*(r) \frac{r_<^l}{r_>^{l+1}} R_i(r) R_j(r) \, dr \qquad \text{(F9)}$$

where R is a radial wave function, $r_<$ and $r_>$ are the lesser and greater coordinates of the two repelling electrons and l is an integer. With covalency R becomes $R(r) = \alpha \phi(r) + \beta \psi(r)$ where ϕ and ψ are the impurity and ligand orbitals and $\beta < \alpha < 1$. Thus the integrals above are primarily proportional to α^4 which decreases with covalency. That B decreases with radial expansion can be seen from the wave function expansion discussion in Chapter V (equation 89) and the observation that the dominant r dependence in the operator is a negative power. Therefore B will be proportional to some positive power of k, the radial expansion scaling factor, which decreases with increasing pressure.

The irreducible representations of the O_h and C_3 point groups are given below along with the product table for the O_h group.

O

	E	$8C_3$	$3C_2$	$6C_2'$	$6C_4$	
A_1	1	1	1	1	1	$x^2+y^2+z^2 = r^2$.
A_2	1	1	1	-1	-1	
E	2	-1	2	0	0	x^2-y^2, $3z^2-r^2$.
T_1	3	0	-1	-1	0	x, y, z; I_x, I_y, I_z.
T_2	3	0	-1	1	-1	xy, yz, zx.

$O_h = O \times \text{Inversion}$

C_3

	E	C_3	C_3^2	
A	1	1	1	z; x^2+y^2; z^2; I_z.
E	1	ω	ω^2	x, y; x^2-y^2, xy;
	1	ω^2	ω	xz, yz; I_x, I_y.

$\omega = \exp(2\pi i/3)$

Products of the Irreducible Representations of O_h

	A_1	A_2	E	T_1	T_2
A_1	A_1	A_2	E	T_1	T_2
A_2	A_2	A_1	E	T_2	T_1
E	E	E	A_1+A_2+E	T_1+T_2	T_1+T_2
T_1	T_1	T_2	T_1+T_2	$A_1+E+T_1+T_2$	$A_2+E+T_1+T_2$
T_2	T_2	T_1	T_1+T_2	$A_2+E+T_1+T_2$	$A_1+E+T_1+T_2$

APPENDIX G

MATRIX ELEMENTS FOR AXIAL AND ZERO FIELD SPLITTINGS AND g SHIFTS

Before the orbital matrix elements of the spin orbit coupling between the $^4A_2$ ground state and the $^4T_2$ excited state can be calculated, the splitting of the excited state due to the axial field must be determined. First the orbital wave functions will be determined. The cubic symmetry operations on the spherical harmonics

$$
\begin{aligned}
Y_3^{-3} &= \sqrt{\frac{7}{4\pi}}\sqrt{\frac{5}{16}}\,(x-iy)^3\,r^{-3} \\
Y_3^{-2} &= \sqrt{\frac{7}{4\pi}}\sqrt{\frac{15}{8}}\,z\,(x-iy)^2\,r^{-3} \\
Y_3^{-1} &= \sqrt{\frac{7}{4\pi}}\sqrt{\frac{3}{16}}\,(x-iy)(5z^2-r^2)\,r^{-3} \\
Y_3^{0} &= \sqrt{\frac{7}{4\pi}}\sqrt{\frac{1}{4}}\,z\,(5z^2-r^2)\,r^{-3} \\
Y_3^{1} &= \sqrt{\frac{7}{4\pi}}\sqrt{\frac{3}{16}}\,(x+iy)(5z^2-r^2)\,r^{-3} \\
Y_3^{2} &= \sqrt{\frac{7}{4\pi}}\sqrt{\frac{15}{8}}\,z\,(x+iy)^2\,r^{-3} \\
Y_3^{3} &= \sqrt{\frac{7}{4\pi}}\sqrt{\frac{5}{16}}\,(x+iy)^3\,r^{-3}
\end{aligned}
\qquad \text{(G1)}
$$

yield the following linear combinations for an F-state ion in O_h symmetry with the four fold axis as the z axis[53]

$$
{}^4T_1: \quad \sqrt{\frac{3}{8}}\,Y_3^{1} + \sqrt{\frac{5}{8}}\,Y_3^{-3}, \quad \sqrt{\frac{3}{8}}\,Y_3^{-1} + \sqrt{\frac{5}{8}}\,Y_3^{3}, \quad Y_3^{0} \qquad \text{(G2)}
$$

$$
\begin{aligned}
{}^4T_2: \quad & \sqrt{\tfrac{5}{8}}\; Y_3^{\,1} - \sqrt{\tfrac{3}{8}}\; Y_3^{\,-3} \\
& \sqrt{\tfrac{5}{8}}\; Y_3^{\,-1} - \sqrt{\tfrac{3}{8}}\; Y_3^{\,3} \\
& \sqrt{\tfrac{1}{2}}\left(Y_3^{\,2} + Y_3^{\,-2}\right)
\end{aligned}
$$

$$
{}^4A_2: \quad \sqrt{\tfrac{1}{2}}\left(Y_3^{\,2} - Y_3^{\,-2}\right)
$$

where they have been classified according to their transformation properties. These must be transformed to the [111] trigonal axis by the Eulerian rotation[80] $R(\alpha\,\beta\,\gamma)$ where $\alpha = 45^\circ$ is the rotation about the z axis, $\beta = \arccos 1/\sqrt{3}$ is the following rotation about the new y axis, and $\gamma = 0^\circ$ is the following rotation about the newest z axis. This transformation yields

$$
\begin{aligned}
{}^4T_{10} \quad & \tfrac{1}{3}\left\{2\; Y_3^{\,0} - \sqrt{\tfrac{5}{2}}\left(Y_3^{\,3} - Y_3^{\,-3}\right)\right\} \\
{}^4T_{1+1} \quad & \sqrt{\tfrac{1}{6}}\left\{\sqrt{5}\; Y_3^{\,2} + Y_3^{\,-1}\right\} \\
{}^4T_{1-1} \quad & \sqrt{\tfrac{1}{6}}\left\{\sqrt{5}\; Y_3^{\,-2} - Y_3^{\,1}\right\} \\
{}^4T_{20} \quad & \sqrt{\tfrac{1}{2}}\left\{Y_3^{\,3} + Y_3^{\,-3}\right\} \\
{}^4T_{2+1} \quad & \sqrt{\tfrac{1}{6}}\left\{Y_3^{\,2} - \sqrt{5}\; Y_3^{\,-1}\right\} \\
{}^4T_{2-1} \quad & \sqrt{\tfrac{1}{6}}\left\{Y_3^{\,-2} + \sqrt{5}\; Y_3^{\,1}\right\} \\
{}^4A_2 \quad & \tfrac{1}{3}\sqrt{2}\left\{\left(Y_3^{\,3} - Y_3^{\,-3}\right) - \sqrt{5}\; Y_3^{\,0}\right\}
\end{aligned}
\qquad \text{(G3)}
$$

Since the $^4T_1$ state does not couple directly to the ground state it will no longer be considered.

Equation 42 (Chapter II) becomes for L = 3

$$V_{AX} = 2\delta\left[L_z^2 - \tfrac{1}{3}L(L+1)\right] = 2\delta\left[L_z^2 - 4\right] \tag{42}$$

and the matrix elements for the $^4T_2$ state are

$$\begin{aligned} &\langle {}^4T_{20}|V_{AX}|{}^4T_{20}\rangle = 2\delta\tfrac{1}{2}\{(9-4)+(9-4)\} = 10\delta \\ &\langle {}^4T_{2+1}|V_{AX}|{}^4T_{2+1}\rangle = 2\delta\tfrac{1}{6}\{(4-4)+5(1-4)\} = -5\delta \\ &\langle {}^4T_{2-1}|V_{AX}|{}^4T_{2-1}\rangle = 2\delta\tfrac{1}{6}\{(4-4)+5(1-4)\} = -5\delta \end{aligned} \tag{G4}$$

To prove that the ground state doesn't split under V_{ax}

$$\langle {}^4A_2|V_{AX}|{}^4A_2\rangle = 2\delta\tfrac{1}{9}\{2[(9-4)+(9-4)]+5(0-4)\} = 0. \tag{G5}$$

Now equation 43 can be evaluated to obtain the ground state splitting

$$\Delta E = -\sum_{n={}^4T_{2\pm1}^{\circ}} \frac{\lambda^2\langle {}^4A_2|L_zS_z+\frac{1}{2}(L_+S_-+L_-S_+)|n\rangle\langle n|\text{----}|{}^4A_2\rangle}{E({}^4T_{2\pm1}^{\circ}) - E({}^4A_2)}. \tag{43}$$

To see which states are connected by which operators the following operations are evaluated;

$$\begin{aligned} L_z|{}^4A_2\rangle &= \tfrac{1}{3}\{3\sqrt{2}\,(Y_3^3 + Y_3^{-3})\} \\ L_+|{}^4A_2\rangle &= \tfrac{1}{3}\{-\sqrt{12}\;Y_3^{-2} - \sqrt{12}\sqrt{5}\;Y_3^{1}\} \\ L_-|{}^4A_2\rangle &= \tfrac{1}{3}\{\sqrt{12}\;Y_3^{2} - \sqrt{12}\sqrt{5}\;Y_3^{-1}\} \end{aligned} \tag{G6}$$

Because the Y's are orthogonal only the following matrix elements need to be calculated;

$$\langle {}^4T_{2\theta} | L_z | {}^4A_2 \rangle = \frac{1}{\sqrt{2}} \frac{1}{3} \left\{ 3\sqrt{2} + 3\sqrt{2} \right\} = 2$$

$$\langle {}^4T_{2+1} | L_- | {}^4A_2 \rangle = \frac{1}{\sqrt{6}} \frac{1}{3} \left\{ \sqrt{12} + 5\sqrt{12} \right\} = 2\sqrt{2} \qquad \text{(G7)}$$

$$\langle {}^4T_{2-1} | L_+ | {}^4A_2 \rangle = \frac{1}{\sqrt{6}} \frac{1}{3} \left\{ -\sqrt{12} - 5\sqrt{12} \right\} = -2\sqrt{2}$$

Similarly

$$\langle {}^4A_2 | L_z | {}^4T_{2\theta} \rangle = 2$$

$$\langle {}^4A_2 | L_+ | {}^4T_{2+1} \rangle = 2\sqrt{2} \qquad \text{(G8)}$$

$$\langle {}^4A_2 | L_- | {}^4T_{2-1} \rangle = -2\sqrt{2}$$

Therefore for $L_z S_z$ one obtains

$$\Delta E_{L_z} = -\lambda^2 \frac{2S_z 2S_z}{10D_q + 10\delta} = -\lambda^2 \frac{4S_z^2}{10D_q + 10\delta} \qquad \text{(G9)}$$

and for $\frac{1}{2}(L_+ S_- + L_- S_+)$ one obtains

$$\Delta E_{L\pm} = -\lambda^2 \frac{\frac{1}{4}\left\{ 2\sqrt{2}\, S_- \, 2\sqrt{2}\, S_+ + (-2\sqrt{2}) S_+ (-2\sqrt{2}) S_- \right\}}{10Dq - 5\delta}$$

$$\Delta E_{L\mp} = -\lambda^2 \frac{2(S_- S_+ + S_+ S_-)}{10Dq - 5\delta} \qquad \text{(G10)}$$

but

$$S_- S_+ = S_+ S_- = S_x^2 + S_y^2 \qquad \text{(G11)}$$

so

$$\Delta E_{L_\pm} = -\lambda^2 \frac{4(S_x^2 + S_y^2)}{10Dq - 5\delta} \quad . \tag{G12}$$

Combining ΔE_{L_z} and $\Delta E_{L_\pm}$ yields

$$\Delta E = -\lambda^2 \left[\frac{4 S_z^2}{10Dq + 10\delta} + \frac{4(S_x^2 + S_y^2)}{10Dq - 5\delta} \right] \tag{44}$$

which is equation 44 (Chapter II).

The change in the g value from the free ion value, g_o, is for g_z from equations 8, G6 and G7

$$(g - g_o)_z = -2\lambda \frac{\langle {}^4A_2 | L_z | {}^4T_{20} \rangle \langle {}^4T_{20} | L_z | {}^4A_2 \rangle}{10Dq + 10\delta} \tag{G13}$$

or

$$(g - g_o)_z = \frac{-8\lambda}{10Dq + 10\delta} \tag{50}$$

which is equation 50 (Chapter II). For $g_\perp$ the $L_\pm$ connect to the ${}^4T_{2\pm1}$ states and from equations 8, G6 and G7

$$(g - g_o)_\perp = -2\lambda \frac{\langle {}^4A_2 | \tfrac{1}{2} L_+ | {}^4T_{2-1} \rangle \langle {}^4T_{2-1} | \tfrac{1}{2} L_- | {}^4A_2 \rangle + \langle {}^4A_2 | \tfrac{1}{2} L_- | {}^4T_{2+1} \rangle \langle {}^4T_{2+1} | \tfrac{1}{2} L_+ | {}^4A_2 \rangle}{10Dq - 5\delta} \tag{G14}$$

or

$$(g - g_o)_\perp = -2\lambda \frac{2+2}{10Dq - 5\delta} = \frac{-8\lambda}{10Dq - 5\delta} \quad . \tag{G15}$$

REFERENCES

1. W. Low, Solid State Physics, edited by F. Seitz and D. Turnbull, Academic Press, New York (1960), Supp. 2.

2. G.E. Pake, Paramagnetic Resonance, W. A. Benjamin, New York (1962), Frontiers in Physics Series.

3. J.D.E. Ingram, Spectroscopy at Radio and Microwave Frequencies, Academic Press, New York (1955).

4. J.D.E. Ingram, Free Radicals as Studied by Electron Spin Resonance, Academic Press, New York (1958).

5. C.P. Shlichter, Principles of Magnetic Resonance, Harper and Row, New York (1963).

6. B. Bleaney and K.W.H. Stevens, Repts. Prog. Phys. 16, 108 (1953).

7. K.D. Bowers and J. Owen, Rept. Prog. Phys. 18, 304 (1955).

8. H.S. Jarrett, Solid State Physics, Vol. 13, Academic Press, New York (1963).

9. R.S. Title, Phys. Rev. 131, 623 (1963).

10. T.P.P. Hall, W.Hayes, R.W.H. Stevenson, and J. Wilkens, J. of Chem. Phys. 38, 1977 (1963).

11. T.P.P. Hall, et. al., J. of Chem. Phys. 39, 35 (1963).

12. J. Ferguson, J. of Chem. Phys. 39, 116 (1963).

13. D.L. Wood, J. Ferguson, K. Knox, and J.F. Dillon, Jr., J. of Chem. Phys. 39, 890 (1963), Figure 4.

14. F K. Hurd, M. Sachs, and W.D. Hershberger, Phys. Rev. 93, 373 (1954).

15. J.H. Van Vleck, Phys. Rev. 41, 208 (1932).

16. J.H. Van Vleck and W.G. Penney, Phil. Mag. 17, 461 (1934).

17. M.H.L. Pryce, Phys. Rev. 80, 1107 (1950).

18. H. Watanabe, Progr. Theoret. Phys. Japan 18, 405 (1957).

19. H. Watanabe, Phys. Rev. Letters 4, 410 (1960).

20. W.M. Walsh, Jr., Phys. Rev. 122, 762 (1961).

21. M.J.D. Powell, J.R. Gabriel and D.F. Johnston, Phys. Rev. Letters 5, 145 (1960).

22. David F. Wait, Phys. Rev. 132, 601 (1963).

23. L. Rimai, T. Deutsch and B.D. Silverman, Phys. Rev 133, A1123 (1964).

24. H. Blum and G.B. Benedek, Bull. Amer. Phys. Soc. 8, 619 (1963).

25. W.J. Viegele and J D. Stettler, Bull. Amer. Phys. Soc. 8, 529 (1963).

26. R.W. Terhune, Ford Scientific Laboratories, Dearborn, Michigan, private communication.

27. P L. Donoho, Physics Dept., The William Marsh Rice University, Houston, Texas, private communication.

28. E.B. Tucker, Phys. Rev. Letters 6, 183 (1961).

29. T.D. Black and P.L. Donoho, Bull. Amer. Phys. Soc. 9, 37 (1964).

30. A.L. Schawlow, A.H. Piksis, and S. Sugano, Phys. Rev. 122, 1469 (1961).

31. M.D. Sturge, Phys. Rev. 131, 1456 (1963), and Phys. Rev. 130, 639 (1963).

32. D R. Stephens and H.G. Drickamer, J. of Chem. Phys. 35, 424 (1961).

33. J.C. Zahner and H.G. Drickamer, J of Chem. Phys. 35, 1483 (1961).

34. S. Minomura and H.G. Drickamer, J. of Chem. Phys. 35, 903 (1961).

35. J.H. Gardner, et. al., Rev. Sci. Inst. 34, 1043 (1963).

36. D.R. Stephens and H.G. Drickamer, J. Chem. Phys. 35, 427 (1961).

37. E.O. Schulz-DuBois, The Bell System Technical Journal 38, 271 (1959).

38. J. Lambe and C. Kikuchi, Phys. Rev. 118, 71 (1960).

39. N. Laurence and J. Lambe, Phys. Rev. 132, 1029 (1963).

40. S. Sugano and Y. Tanabe, J. Phys. Soc. Japan 13, 880 and 899 (1958).

41. H.A. Weakliem and D.S. McClure, J. Appl. Phys. S33, 347 (1962).

42. D.S. McClure, J. Chem. Phys. 36 2757 (1962).

43. M.D. Sturge, Phys. Rev. 130, 639 (1963).

44. L.L. Lohr, Jr., and W.N. Lipscomb, J. Chem. Phys. 38, 1607, (1963).

45. E.B. Royce and N. Bloembergen, Phys. Rev. 131, 1912 (1963).

46. R.W.G. Wyckoff, Crystal Structures Handbook, Interscience Pub., Inc., New York (1958).

47. B.T. Bernstein, J. Appl. Phys. 34, 169 (1963).

48. W. Marshall and R. Stuart, Phys. Rev. 123, 2048 (1961).

49. M.H.L. Pryce, Proc. Roy. Soc. 63A, 25 (1950).

50. A. Abragram and M.H. L. Pryce, Proc. Roy. Soc. 205A, 135 (1951).

51. H.A. Bethe and E.E. Salpeter, Quantum Mechanics of One- and Two-Electron Atoms, Academic Press, New York (1957).

52. M. Wolfsberg and L. Helmholz, J. Chem. Phys. 20, 837 (1952).

53. C.J. Ballhausen, Introduction to Ligand Field Theory, Ch.7, McGraw Hill Book Co., Inc., New York (1962).

54. J.C. Slater, Quantum Theory of Atomic Structure, New York, McGraw-Hill Book Co., Inc., (1960).

55. J.S. Griffith, The Theory of Transition Metal Ions, Cambridge (1961).

56. V. Heine, Group Theory in Quantum Mechanics, Pergamon Press, New York (1960).

57. K.W.H. Stevens, Proc. Phys. Soc. 65A, 209 (1952).

58. G. Racah, Phys. Rev. 62, 438 (1942).

59. N. Laurence, E.C. McIrvine, and J. Lambe, J. Phys. Chem. Solids 23, 515 (1962).

60. J.F. Nye, Physical Properties of Crystals, Oxford University Press, London (1957).

61. C. Kittel, Introduction to Solid State Physics, John Wiley and Sons, Inc., New York (1956).

62. S. Sugano, J. Appl. Phys. S33, 303 (1962).

63. H. Kamimura, Phys. Rev. 128, 1077 (1962).

64. Y. Tanabe and S. Sugano, J. Phys. Soc. Japan 9, 753 and 766 (1954).

65. A.F. Clark and D.F. Wait, Rev. of Sci. Inst., To be published.

66. W.M. Walsh, Jr. and N. Bloembergen, Phys. Rev. 107, 909 (1957).

67. A.W. Lawson and George E. Smith, Rev. of Sci. Inst. 30, 989 (1959).

68. G. Feher, Bell System Technical Journal 36, 449 (1957).

69. P.W. Bridgman, The Physics of High Pressure, Bell and Sons, Ltd., London (1931).

70. A.F. Clark, R.H. Sands, and C. Kikuchi, Bull. Amer. Phys. Soc. 9, 36 (1964).

71. S. Geschwind and J.P. Remeika, J. Appl. Phys. S33, 370 (1962).

72. D.S. McClure, J. Chem. Phys. 38, 2289 (1963).

73. L.D. Landau and E.M. Lifshitz, Theory of Elasticity, Addison-Wesley Publishing Co., Inc., Reading, Mass., (1959).

74. A.C. Eringen, Nonlinear Theory of Continuous Media, McGraw-Hill Book Company, Inc., New York, (1962).

75. J.B. Wachtman, Jr., et al. J. of Research N.B.S., 64A, 213, (1960).

76. D.I. Bolef and M. Menes, J. Appl. Phys. 31, 1010, (1960).

77. W.G. Mayer and E.A. Hiedemann, J. of Acoustical Society of Amer. 30, 756, (1958).

78. H.B. Huntington, Solid State Physics 7, 213, Academic Press Inc., New York, (1958).

79. S. Geschwind, et al., Phys. Rev. 126, 1684 (1962).

80. D.M. Brink and G.R. Satchler, Angular Momentum, Oxford (1962).